PNNL-11536 Rev. 1
UC-2030

Gas Retention and Release Behavior in Hanford Double-Shell Waste Tanks

P. A. Meyer
M. E. Brewster
S. A. Bryan
G. Chen
L. R. Pederson
C. W. Stewart
G. Terrones

May 1997

Prepared for the U.S. Department of Energy
under Contract DE-AC06-76RLO 1830

Pacific Northwest National Laboratory
Richland, Washington 99352

DISCLAIMER

Preface

This report was prepared to satisfy the Defense Nuclear Facilities Safety Board (DNFSB) Recommendation 93-5 Implementation Plan (DOE 1996), Milestone 5.4.3.5.1, "Letter reporting refinement of flammable gas generation/retention models using void meter and retained gas sampling data."

The data obtained from operating the void fraction instrument (VFI) (Stewart et al. 1996a), and retained gas sampler (RGS) (Shekarriz et al. 1997) have determined the amount and composition of gas retained in the wastes in the six double-shell tanks on the Flammable Gas Watch List (Johnson et al. 1997). The interpretation of those data and the models for gas retention and release developed or improved as a result represent significant progress toward an adequate understanding of the mechanisms of gas generation, retention, and release. This report summarizes the VFI and RGS data and presents the models these data have enabled us to develop.

Abstract

This report describes the current understanding of flammable gas retention and release in Hanford double-shell waste tanks AN-103, AN-104, AN-105, AW-101, SY-101, and SY-103. This knowledge is based on analyses, experimental results, and observations of tank behavior. The applicable data available from the void fraction instrument, retained gas sampler, ball rheometer, tank characterization, and field monitoring are summarized. Retained gas volumes and void fractions are updated with these new data. Using the retained gas compositions from the retained gas sampler, peak dome pressures during a gas burn are calculated as a function of the fraction of retained gas hypothetically released instantaneously into the tank head space. Models and criteria are given for gas generation, initiation of buoyant displacement, and resulting gas release; and predictions are compared with observed tank behavior.

Summary

The gas retention and release behaviors of Hanford double-shell tanks (DSTs) on the Flammable Gas Watch List (FGWL), AN-103, AN-104, AN-105, AW-101, SY-101, and SY-103, were characterized in detail using the ball rheometer and void fraction instrument (VFI) from December 1994 to May 1996. These are reported in Stewart et al. (1996a). Additional data on gas composition and void fraction have since become available on four of these tanks (AW-101, AN-103, AN-104, and AN-105) using the retained gas sampler (RGS) from March through September 1996 and are described in Shekarriz et al. (1997).

The main objective of the work presented in this report is improving the models for gas retention and release based on these data and updating the original gas retention and release calculations with the new RGS and core sample data. Because of this extensive characterization effort, we have a better knowledge and understanding of these DSTs than of any other Hanford tanks. We include models that help explain current gas retention and release behavior and examine the potential for other tanks to exhibit hazardous episodic gas releases. The models developed for gas generation based on waste sample testing are also summarized. While none of these models have been formally verified and validated for safety analysis, they are consistent with the extant body of data and observations. The updates to earlier calculations and improvements to gas generation, retention, and release models are summarized below.

Gas Generation Models and Results

The three most important mechanisms for gas generation are 1) radiation-induced chemical decomposition of water and some organic species; 2) thermally induced chemical decomposition, mainly involving organic complexants and solvents; and 3) chemical decomposition of the steel tank walls. The first two clearly dominate, and the yield from radiolysis of the organic compounds is especially important.

Recent studies on gas evolution from tank waste samples and prior mechanistic studies with simulants have advanced our understanding of gas generation processes significantly. Activation energies for overall gas generation as well as for hydrogen, nitrogen, and nitrous oxide are now well established for the waste from Tank SY-103 (Bryan et al. 1996). The relative magnitude of the thermal and radiolytic components of gas generation are known as a function of temperature for wastes from SY-101 and SY-103, and a predictive model for gas generation based on the behavior of SY-103 waste has been developed. The gas composition in SY-103 has been revised according to the experimental generation rates.

Though we know how to study gas generation effectively, and we understand the gas generation behavior of SY-101 and SY-103 waste reasonably well, we cannot yet extrapolate to other waste types with confidence and precision. We must be able to do this to predict the long-term gas generation behavior. To this end, gas generation tests are being performed on waste samples from Tanks S-102 (a single-shell tank), AW-101, and AN-105.

Gas Retention Models and Results

Updating the retained gas volume calculation with the additional data from the RGS produced only minor adjustments in the average void fraction, void distribution, and total stored volume. The crust gas volume calculation model was modified as a result of the new information. The original calculation derived for SY-101 conservatively assumed a crust void fraction of 0.25. The best information now available indicates that the crust consists of the same material as the

nonconvective layer and that its void fraction is approximately the neutral buoyancy value. Consistent with these observations, the new model assumes the crust void fraction is slightly above neutral buoyancy such that a large fraction of its thickness is submerged below the free liquid surface. This change reduces the estimated crust gas volume by as much as half in some tanks.

The barometric pressure effect (BPE) model, which estimates the retained gas volume from the response of waste level to barometric pressure fluctuations, is derived in detail and its results compared with the gas volumes calculated from VFI and RGS void fractions. The assumptions made during the derivation require that the BPE model be applied to tanks with relatively deep, wet waste in which the vertical gas distribution can be estimated. Currently, this includes the DSTs and a few of the single-shell tanks (SSTs). The difference between the BPE and VFI gas volume estimates is well within the standard deviation of the VFI results. Good results are also obtained where the vertical gas distribution has a high uncertainty.

Gas Release Models and Results

The large episodic gas release events (GREs) historically observed in the DSTs on the FGWL are believed to be caused by the *buoyant displacement* mechanism (Stewart 1996b). In a buoyant displacement, a portion, or "gob," of the nonconvective layer near the tank bottom accumulates gas until it becomes sufficiently buoyant to overcome the weight and strength of material restraining it. At that point it suddenly breaks away and rises through the supernatant liquid layer. The hydrostatic pressure decreases as the gob rises, causing the stored gas bubbles to expand. Where bubble expansion is sufficient to fail the surrounding material, gas is released from the gob and, if not trapped by existing crust, may escape into the head space.

Buoyancy tends to destabilize the nonconvective layer, while the material strength stabilizes it. A buoyant displacement can occur when local void fraction is high enough to produce a net upward force in the nonconvective layer (exceeds "neutral buoyancy"). However, the strength of the bulk solids will keep the gob from rising until the buoyant force causes the material yield stress to be exceeded. Therefore, the void fraction must be significantly greater than the neutral buoyancy value before a buoyant displacement can begin.

The effect of the material strength depends on the shape of the gob as well as its size. The shape effect depends on the ratio of the surface area to volume. For large gobs, the effect of material strength is minimal, and the critical void fraction is approximately equal to the neutral buoyancy value. However, small gobs have a higher surface-to-volume ratio and require a much higher void fraction. To first order, gobs with a diameter approximately equal to the nonconvective layer depth may be the most probable. Better estimates are obtained with a detailed stability analysis.

At the onset of a buoyant displacement, the yield stress of the nonconvective material is exceeded, and the material around the participating gob begins to flow. Assuming that at this point the entire nonconvective layer behaves as a viscous fluid, the length scale can be estimated from the Rayleigh-Taylor theory for superposed fluid layers of different densities and viscosities. This analysis allows both the size and critical void fraction of a gob to be determined and leads to a method to predict the gas release volume and frequency of buoyant displacements in the six FGWL DSTs. The estimates compare quite well with actual tank behavior as derived from the waste level history.

Basic energy conservation principles can be applied to the buoyant displacement process to determine the conditions required for it to release gas. A simple predictive model is derived that describes the energy requirements of buoyant displacement in terms of estimated or measurable parameters. The model establishes a criterion for gas release by a buoyant displacement. The total

amount of energy stored in a gob of gas-bearing solids must exceed the energy required to yield the gas-retaining matrix. The model is compared with data from scaled experiments and applied to the six DSTs on the FGWL. The conclusion is that a relatively deep layer of supernatant liquid is required for buoyant displacement to release gas. This condition currently exists only in the DSTs.

The calculation of the peak dome pressure resulting from a postulated deflagration has also been updated with actual gas compositions from RGS data for AW-101, AN-103, AN-104, and AN-105. SY-103 compositions were derived from recent gas generation experiments (Bryan et al. 1996). The SY-101 compositions are unchanged. The new data slightly reduced the predicted pressures in the AN tanks. The peak pressure in SY-103 increased because the new composition has about twice the hydrogen. Only SY-101 demonstrated a clear potential for a flammable gas burn that could fail the dome structure. None of the other tanks appear capable of producing peak pressures exceeding the 3.08-atm limit at 99% confidence for even a very large release of 50% of their stored gas, which is far larger than any observed to date. Tanks SY-103 and AW-101 remain incapable of exceeding the pressure limit even if they were to release 100% of their stored gas.

The models discussed above, and the data on which they are based, allow us to evaluate these tanks' gas release potential. To within reasonable uncertainty, we now know how much gas they contain, its composition, and where it is stored; we also understand how the gas is released, and we can estimate approximately how much gas will be released and how often. Though these models are not, and possibly cannot be formally validated, they represent our best understanding and are consistent with the available knowledge base.

References

Bryan S, CM King, LR Pederson, SV Forbes, and RL Sell. 1996. *Gas Generation from Tank 241-SY-103 Waste.* PNNL-10978, Pacific Northwest National Laboratory, Richland, Washington.

Johnson GD. 1997 *Flammable Gas Project Topical Report.* HNF-SP-1193 Rev. 2, Duke Engineering Services Hanford, Richland, Washington.

Shekarriz A, DR Rector, LA Mahoney, MA Chieda, JM Bates, RE Bauer, NS Cannon, BE Hey, CG Linschooten, FJ Reitz, and ER Siciliano. 1997. *Composition and Quantities of Retained Gas Measured in Hanford Waste Tanks 241-AW-101, A-101, AN-105, AN-104, and AN-103.* PNNL-11450 Rev. 1, Pacific Northwest National Laboratory, Richland, Washington.

Stewart CW, JM Alzheimer, ME Brewster, G Chen, RE Mendoza, HC Reid, CL Shepard, and G Terrones. 1996a. *In Situ Rheology and Gas Volume in Hanford Double-Shell Waste Tanks.* PNNL-11296, Pacific Northwest National Laboratory, Richland, Washington.

Stewart CW, ME Brewster, PA Gauglitz, LA Mahoney, PA Meyer, KP Recknagle, and HC Reid. 1996b. *Gas Retention and Release Behavior in Hanford Single-Shell Waste Tanks.* PNNL-11391, Pacific Northwest National Laboratory, Richland, Washington.

Acknowledgments

The authors gratefully thank Lenna Mahoney, Reza Shekarriz, and Dave Rector, who supplied the RGS data and help us understand it. Thanks also to Blaine Barton and Steve Barker (both of LMHC) for providing us helpful suggestions and encouragement on the gas release model.

Thanks to Jerry Johnson (DESH) and to John Gray and Craig Groendyke (DOE-RL) for assistance in seeing the document through the formal review process.

We appreciate the efforts of Sheila Bennett who edited this report several times through final publication. Thanks to Kathy Rightmire for preparing the core extrusion and waste surface photos.

Contents

Figures

Tables

1.0 Introduction

The primary purpose of this report is to present models developed or updated using the data from the retained gas sampler (RGS), void fraction instrument (VFI), and ball rheometer to predict gas retention and release behavior. Models have been developed for determining stored gas volume, predicting peak pressure resulting from burning a specified fraction of stored gas volume, and predicting the potential size and frequency of buoyant displacement and whether a displacement event will release gas. A second major objective is to update the gas retention and release calculations given in Stewart et al. (1996a) with the new RGS and core sample data in Shekarriz et al. (1997). The models developed for gas generation based on waste sample testing by Bryan et al. (1996) are also summarized.

The flammable gas hazard in Hanford waste tanks was first recognized in the behavior of double-shell tank (DST) 241-SY-101 (SY-101). The waste level in this tank began periodically rising and suddenly dropping shortly after it was filled in 1980. The large, "sawtooth" level drops were taken as an indication of episodic gas releases that might pose a safety hazard. A period of intense study of this tank's behavior in 1990–1992 revealed that these releases were, in fact, hazardous; the gas was indeed occasionally flammable, and the releases were quite large. Some of them had sufficient volume to exceed the lower flammability limit (LFL) in the entire head space and would probably have damaged the tank if the gas had been ignited.

The major concern in SY-101 was mitigated in late 1993 with the installation of a mixer pump that has prevented gas retention (Allemann et al. 1994; Stewart et al. 1994; Brewster et al. 1995). But the experience with SY-101 created anxiety that other tanks might have similar large gas releases or the potential to do so, associating a perception of imminent danger with all 177 waste tanks. We know now that this perception was not correct. The large episodic gas releases in SY-101 were truly unique in size and hazard.

The historic gas releases in SY-101 prior to mixing were buoyancy-induced displacement events, at one time called "rollovers" (Allemann et al. 1993). In a buoyant displacement, a portion, or "gob," of the nonconvective layer near the tank bottom accumulates gas until it becomes sufficiently buoyant to overcome the weight and strength of material restraining it. At that point it suddenly breaks away and rises through the supernatant liquid layer. The stored gas bubbles expand as the gob rises, failing the surrounding matrix so a portion of the gas can escape from the gob into the head space.

Theory, experiment, and experience indicate that only the waste configuration found in the DSTs has the potential for significant gas releases by buoyant displacements. Only SY-103, AW-101, AN-103, AN-104, and AN-105 now actually exhibit this kind of episodic gas release, but these releases are typically less than 30 cubic meters in volume, compared with over 100 cubic meters in SY-101.

These five tanks, plus SY-101, represent the six DSTs on the 25-tank Flammable Gas Watch List (FGWL). The FGWL tanks were identified in response to Public Law 101-510, Section 3133 (the Wyden Amendment), as having a "serious potential for release of high level waste due to uncontrolled increases in temperature or pressure" from a flammable gas burn. This status has provided a powerful impetus for experiments, characterization, monitoring, and analytical studies sufficient to fully understand the risk involved. Accordingly, the void fraction instrument (VFI), ball rheometer, and the RGS were developed and deployed in the FGWL DSTs starting in December 1994. Gas generation tests on SY-103 waste samples were also performed in 1996.

The gas retention and release behaviors of Hanford DSTs AN-103, AN-104, AN-105, AW-101, SY-101, and SY-103 have been characterized in detail by the ball rheometer and VFI during operations from December 1994 to May 1996. The results of this testing campaign, given in Stewart et al. (1996a), include the following:

- Waste configuration (thickness of the crust, convective, and nonconvective layers)
- Rheology of the convective and nonconvective layers (viscosity and yield stress as a function of shear rate, and density)
- Retained gas volume and distribution (void fraction profile, effective pressure, and gas volume of each waste layer)
- Gas release behavior (gas release history, distribution of release volume and release fraction, peak dome pressure during a hypothetical burn).

Additional data have since become available on four of these tanks (AW-101, AN-103, AN-104, and AN-105) from the RGS segments included in push-mode sampling from March through September 1996. Shekarriz et al. (1997) give a detailed description of RGS design and operation and present the gas compositions and void fractions obtained. The concentration of ammonia dissolved in the liquid and observations of X-ray imaging are also discussed. The sampling history of each tank is shown in Table 1.1.

Table 1.1. Tank Waste Sampling History

Tank	Riser	Core + RGS	VFI	Ball Rheo.
SY-101	22A	5/22-26/91 (win. C)	-	-
	11B	12/14-16/91 (win. E)	12/21/94	4/5/95
	4A	-	1/17/95	3/28/95
SY-103	unkn.	9/86	-	-
	14A	9/94	-	-
	17C	-	7/19/95	7/14/95
	22A	-	8/18/95	8/8/95
AW-101	13A	-	9/22/95	9/18/95
	1C	-	9/24/95	9/20/95
	24A	3/15-22/96 (RGS)	-	-
	24B	5-22-23/96 (RGS)	-	-
AN-105	1B	-	12/20/95	12/15/95
	16B	-	12/22/95	12/18/95
	12A	6/13-17/96 (RGS)	-	-
	7B	6/26-28/96 (RGS)	-	-
AN-104	16B	-	4/2/96	3/27/96
	1B	-	4/4/96	4/1/96
	12A	8/14/96 (RGS)	-	-
	10A	9/9-12/96 (RGS)	-	-
AN-103	7B	2/10-14/86	-	-
	16B	-	5/14/96	5/6/96
	1B	-	5/16/96	5/10/96
	12A	9/13-16/96 (RGS)	-	-
	21A	9/20/96 (RGS)	-	-

The balance of this report is organized into four categories consistent with the important aspects of the flammable gas safety issue: gas generation, retention, release, and the immediate consequences of gas release, should the gas be ignited. Each is discussed in a separate section as indicated below.

An understanding of gas generation is important to successful operation of the waste tanks for several reasons. First a knowledge of the gas generation rate is needed to verify that any given tank has sufficient ventilation to keep flammable gas concentration at a safe level in the dome space in the steady state (i.e., gas release equals generation rate). Understanding the generation mechanisms of the various gases is important for estimating the stored gas composition and in predicting long-term effects. The results of recent gas generation testing on SY-103 waste samples (Bryan et al. 1996) and the current model for flammable gas generation are discussed in Section 2.

The gas retention calculations given in Stewart et al. (1996a) are updated with the new RGS and core sample data in Shekarriz et al. (1997) in Section 3. Except for the crust layer, the update did not change the gas volumes significantly. Recent photos of AN-103 and AN-104 core extrusions and representative video frames of the waste surface in all six tanks complete the visual data set. Since the gas distribution is now known in these six tanks, the stored gas volume can be calculated at any time from the waste level or barometric pressure response. These models are also described in Section 3.

Models that predict how a buoyant displacement event is initiated have been developed using the waste rheology and configuration data as well as the observed gas release behavior. These models not only explain the gas releases in the six tanks tested but can also be used to predict whether other tanks (e.g., newly filled via transfers) will experience buoyant displacement. It has also been determined that only tanks with a waste configuration similar to these six DSTs have the potential for significant gas releases by buoyant displacement (Stewart et al. 1996b). These models are derived in Section 4.

Given the stored gas volume and its composition, the peak pressure during a hypothetical burn can be estimated as a function of release fraction. The peak pressure model and the results are described in Section 5. References cited can be found in Section 6.

The data acquired and the models developed to date are neither perfect nor complete. We have few data on the floating crust layer and on the particle shape and size distributions, for example. However, we believe the current understanding is sufficient to assess the potential flammable gas risk in the tanks studied in this report, under storage operations, for the foreseeable future. In any event, since no new waste-intrusive measurements are planned in these tanks, temperature profiles, waste level, and head-space gas monitoring represent the only new data available for a long time to come.

2.0 Gas Generation Models

The current knowledge of gas generation has been summarized by Pederson and Bryan (1996). While the VFI and RGS data do not directly support gas generation studies, the gas compositions from the RGS provide an independent, though indirect, measure of the relative gas generation rates of the various species. This section provides a brief overview of the models for the kinetics of gas generation and current laboratory results to measure and predict gas generation.

Gas generation in the waste results from radiation-induced chemical decomposition of water and some organic species and from thermally induced chemical decomposition, mainly involving organic complexants and solvents. The effects of radiation on the generation of gases (Meisel et al. 1993) and the thermal degradation of the organic species (Barefield et al. 1995, 1996) have been evaluated through studies of synthetic waste mixtures. More recently, the focus has been on testing actual tank waste samples (Bryan et al. 1996; Person 1996).

2.1 Studies Using Actual Waste

Gas generation was evaluated from samples of the convective layer of SY-103 (Bryan et al. 1996) and a core composite sample from SY-101 (Person 1996). The changes in the gas generation rates as a consequence of changes in temperature, radiation dose rate, presence or absence of oxygen, and dilution with concentrated sodium hydroxide solution were studied to gain perspective on the principal reaction parameters. Thermal and self-irradiation gas generation rates for the convective layer of Tank SY-103 were determined from 60 to 120°C (140 to 248°F). The results of the thermal reactions are shown in Figures 2.1 and 2.2 and Table 2.1. Nitrous oxide generation was favored at high reaction temperatures, and hydrogen generation was favored at temperatures similar to those at which wastes are stored.

Thermal and self-irradiation gas generation results reported by Bryan et al. (1996) were based on total gas generation from samples heated to 60–120°C. Radiolytic gas generation was assumed to be much less than thermal generation at and above 60°C. While this assumption is basically correct, the data were further analyzed to determine the small contribution to gas generation from the self-radiolysis of the radioactive samples (Pederson and Bryan 1996). The radiolytic contribution was subtracted from the total gas generation, yielding the "thermal-only" gas generation for these test samples. The self-irradiation dose rate in SY-103 convective layer samples was calculated at 119 R/h, mainly from ^{137}Cs beta decay, with most of the remainder due to ^{90}Sr (Bryan et al. 1996). In the actual waste tank, the self-irradiation dose rate was calculated to be 444 R/h, about three-fourths of which derived from ^{137}Cs gamma decay (Bryan et al. 1996).

Overall rates of gas generation were found to follow standard Arrhenius behavior over the temperature range of 60 to 120°C. These results are shown in Figure 2.2 along with additional data taken later at 33°C (the approximate temperature of SY-103 waste). The best fit of the ln (initial rate) versus the inverse of absolute temperature for the 60 to 120°C data was used to estimate the activation energy for gas generation (solid line in the figure). As discussed above, high-temperature gas generation (above 60°C) was dominated by thermal processes, and the effect of the radiolytic gas generation was small. However, the gas generation measured at 33°C showed a significant deviation from the value expected for thermal-only gas generation. The difference between the measured rate of gas generation at 33°C and the extrapolated value was attributed tothe enhanced gas generation due to self-radiolytic processes.

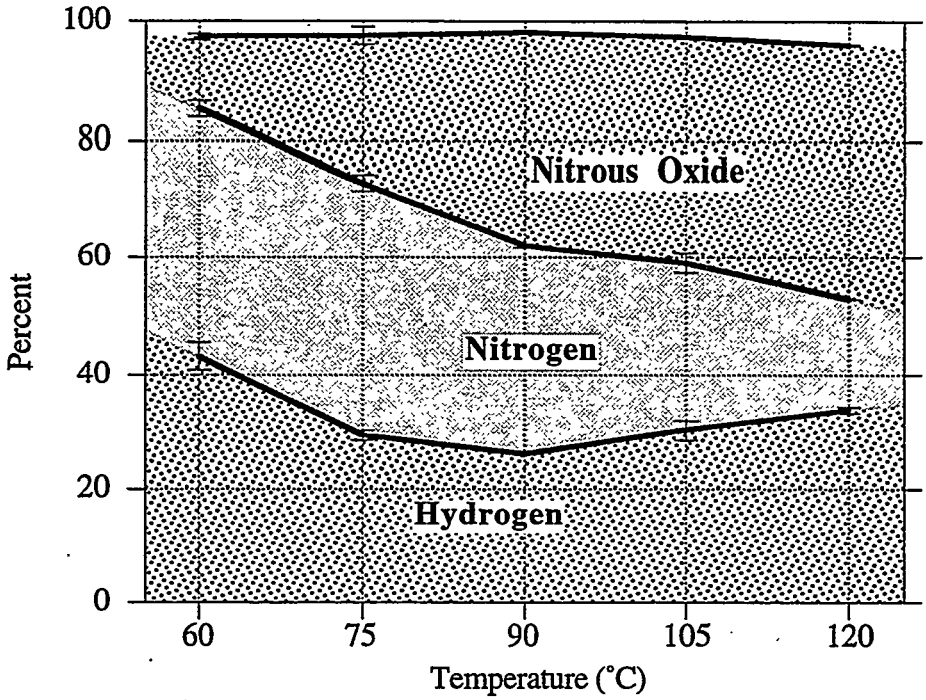

Figure 2.1. Generated Gas Composition Versus Temperature from SY-103

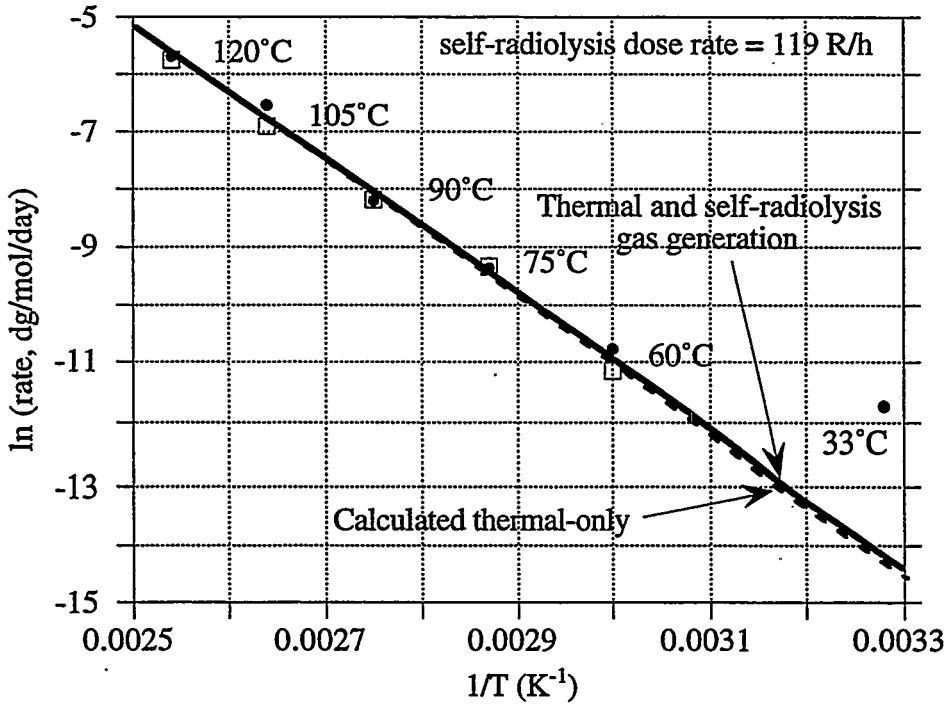

Figure 2.2. Arrhenius Plot of Thermal Gas Generation Rates for SY-103

Table 2.1. Pre-Exponential Factors and Activation Energies for Thermal Gas Generation

Pre-Exponential Factors (mol/kg-d) and Energies of Activation (kJ/mol) (rate = $Aexp[-E_a/RT]$)	
Gas	Thermal Activation Parameters
H_2	E_a = 91.3 ± 9.0[(a)] A = 1.4E+09
N_2	E_a = 83.7 ± 10.2 A = 1.1E+08
N_2O	E_a = 116.7 ± 9.4 A = 5.5E+12
Total gas	E_a = 96.3 ± 6.3 A = 1.2E+10
(a) Errors are expressed as 95% confidence intervals.	

The radiolytic contribution for gas generation was expected to be approximately constant over the limited temperature range of these samples (33 to 120°C). This allowed the radiolytic contribution measured at 33°C to be subtracted from the total gas generation measured for the high-temperature samples (60 to 120°C). The best fit of the gas generation data now corrected for the radiolytic contribution is shown as the dashed line in Figure 2.2. The difference in the slopes of the solid line (data from total gas generation) and the dashed line (data from thermal-only gas generation after correction for radiolytic component) is small. Even though the radiolytic contribution is small at high temperature (above 60°C), it should be pointed out that the self-radiolysis contribution to total gas generation is significant at tank temperatures (32°C) and indeed is approximately five times greater than the thermal process at that temperature. Radiolytic gas generation yields were determined for SY-103 convective layer samples using an external radiation source. The results are presented in Table 2.2. The average $G(H_2)$ value for 60 and 75°C is 0.14 ± 0.02 molecules/100 eV.

Although the comparisons are indirect, the gas generation rates from the experimental program and in-tank measurements are similar, as summarized in Table 2.3. The total calculated hydrogen gas generation from these waste samples is 2.0×10^{-6} mol(H_2)/kg/day. Hydrogen production of 2.3×10^{-6} mol/kg/day was reported in SY-103 based on gas composition from headspace grab samples and the ventilation rate (Wilkins 1995). The agreement between these two investigations is excellent and confirms that the amount of hydrogen generated thermally at tank temperature (31.7°C) is small; about 20% of the amount generated by the wastes in SY-103 as a consequence of thermal chemistry.

Table 2.2. G-Values in Radiolytic Reactions from SY-103 at 5300 R/h

Gas	G Value(molecules/100 eV)
Hydrogen	0.14 ± 0.02
Nitrogen	0.53 ± 0.03
Nitrous Oxide	0.033 ± 0.009

Table 2.3. Comparison of Gas Generation Rates

Contribution to Gas Generation	Gas Generation Rate (mol/kg-day)		
	Hydrogen	Nitrous Oxide	Nitrogen
Thermal at 31.7°C	3.1×10^{-7}	5.4×10^{-8}	4.9×10^{-7}
Radiolytic at 444 R/h	1.63×10^{-6}	3.84×10^{-7}	6.17×10^{-6}
Sum	1.9 " 0.1 x 10^{-6}	4.4 " 0.1 x 10^{-7}	6.7 " 0.1 x 10^{-6}
In-tank (Wilkins 1995)	2.3 " 0.2 x 10^{-6}	not determined	not determined

Independent experiments were carried out with a core composite sample from SY-101 (Person 1996). The tests were performed in the approximate temperature range of 65 to 100°C (149 to 212°F) with helium or 30% oxygen in helium as the cover gas. Additional tests were performed with the waste sample diluted by approximately 50 vol% with 2.5 M sodium hydroxide solution. The results in Figure 2.3 show that overall rates of gas generation from SY-101 waste samples were remarkably similar to those from SY-103 waste. The total gas generation rates for SY-101 for the first 10 days of tests at 100°C (212°F) (0.75 m-mol/kg/day), for example, are statistically indistinguishable from the kinetic data from SY-103 interpolated to that temperature.

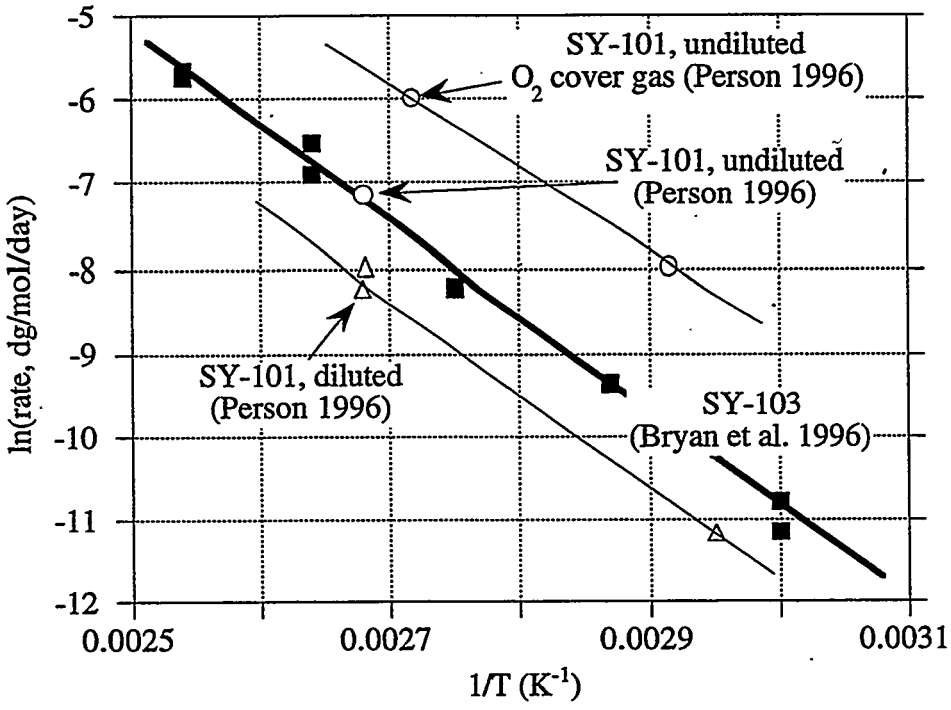

Figure 2.3. Comparison of Total Gas Generation from SY-101 and SY-103

2.2 Kinetics of Gas Generation

Although flammable gas generation rates in SY-101 and SY-103 have been well established through laboratory studies and in-tank observations, the rates for other tanks are not known with any certainty. Equations were developed to estimate the rate of hydrogen generation from tank wastes as a function of temperature, total organic carbon (TOC) content, and aluminum concentration (Hopkins 1994; Graves 1994) compared to that of SY-101. The newly measured kinetic gas generation parameters from SY-103 waste samples makes it a better choice as the benchmark from which to estimate generation rates in other tanks. The modified expression below (Pederson and Bryan 1996) estimates the thermal component of hydrogen generation in Tank X in mol/kg/day based on SY-103 behavior:

$$\dot{Q}_X^{TH} = \dot{Q}_{SY103}^{TH}\left(\frac{[TOC]_X}{[TOC]_{SY103}}\right)\left(\frac{[Al]_X}{[Al]_{SY103}}\right)\exp\left[\frac{E_{SY103}^{H_2}}{R}\left(\frac{1}{T_X}-\frac{1}{T_{SY103}}\right)\right] \qquad (2.1)$$

where $\dot{Q}_{SY103}^{TH}$ is the baseline thermal hydrogen generation rate for SY-103, 3.5×10^{-7} mol/kg/day at $T_{SY103} = 304.7$°K (89.1°F) with $[TOC]_{SY103} = 0.74$ wt% (convective layer) and $[Al]_{SY103} = 2.8$ wt%, E_{SY103}^{H2} is the activation energy of -91 ± 9 kJ/mol (see Table 2.1), and R is the universal gas constant (0.008314 kJ/mol-K).

The estimated radiolytic yield of hydrogen, based on laboratory data for SY-103 wastes and a correlation developed by Meisel et al. (1993), is

$$G_{SY103}^{H_2} = 0.031 + 0.15\,[TOC]_{SY103} \quad \text{molecules } H_2/100 \text{ eV} \qquad (2.2)$$

The radiolytic hydrogen generation rate from Tank X in mol/kg/day can be estimated based on SY-103 behavior by the following:

$$\dot{Q}_X^{RAD} = \dot{Q}_{SY103}^{RAD}\left(\frac{0.031+0.15[TOC]_X}{0.031+0.15[TOC]_{SY103}}\right)\left(\frac{\dot{R}_X}{\dot{R}_{SY103}}\right) \qquad (2.3)$$

where

$\dot{Q}_{SY103}^{RAD}$ is the baseline radiolytic hydrogen generation rate for SY-103:
1.63×10^{-6} mol/kg/day for a dose rate $\dot{R}_{SY103} = 444$ R/hr (Pederson and Bryan 1996) with $[TOC]_{SY103} = 0.74$ wt%.

2.3 Recommendations for Improving Gas Generation Models

The total rate of hydrogen generation is the sum of the thermal and radiolytic components. While these expressions provide qualitative guidance about the rates of hydrogen generation in the Hanford tanks, it is evident that they will need to be modified to quantitatively predict hydrogen generation. Factors such as the nature of the organic compounds (for example, sodium glycolate provides hydrogen but sodium oxalate does not) are not considered in the TOC parameter, and the synergisms between the radiolytic and thermal reactions are not considered in the analysis.

Significant differences exist in composition among Hanford waste tanks. As a result, gas generation behaviors are expected to vary considerably. Most of the technical work has focused on chelator and chelator fragments, which dissolve in the liquid fraction. Other wastes contain solvents that are largely insoluble in the liquid fraction and may decompose by totally different pathways. Laboratory gas generation studies using actual waste mixtures that represent different waste classes will significantly enhance our ability to predict gas generation behavior in Hanford wastes.

Pacific Northwest National Laboratory
Operated by Battelle for the U.S. Department of Energy

TWSFG97.51

July 15, 1997

Distribution

Holders of PNNL-11536,

PNNL-11536, *Gas Retention and Release Behavior in Hanford Double-Shell Waste Tanks,* published by Pacific Northwest National Laboratory in May 1997, contained errors. Please replace the erroneous pages with the identically numbered attached corrected versions.

The layer dimensions listed on the void fraction profile plots have been corrected and are now consistent with those listed in the corresponding tables. Equation 2.1 has also been corrected.

Also of importance, note that these corrections are to be made to PNNL-11536 Rev 1, which supercedes Rev 0.

Thanks,

Joe Brothers

jwb

Attachment

cc: File/LB

Battelle Boulevard ■ P.O. Box 999 ■ Richland, WA 99352

Telephone (509) 375-2396 ■ Email jw_brothers@pnl.gov ■ Fax (509) 372-4600

3.0 Gas Retention Models

This section of the report gives the current estimates of the retained gas volume, its distribution, and its composition from data obtained with the VFI and RGS over the past two years. The gas volume and distribution in each tank are provided in Section 3.1 (the gas compositions derived from RGS data and gas generation studies are given in Section 5). The barometric pressure effect (BPE) and surface level effect (SLE) models for determining the retained gas volume indirectly are derived and evaluated in Section 3.3. The collection of extrusion and waste surface photos is presented in Section 3.4. Recommendations for improving gas retention models and data are given in Section 3.5.

3.1 Retained Gas Volume

The gas volume of each waste in SY-101, SY-103, AW-101, AN-103, AN-104, and AN-105 was calculated from VFI measurements in Stewart et al. (1996a). Since then, the RGS has provided additional void fraction data in AN-103, AN-104, AN-105, and AW-101 that are now included in the overall data set. The non-RGS core samples also provided current nonconvective layer densities in AN-103 and AN-104 that were not available when the initial volume calculations were performed.[a] The revised data are

1. Void fractions determined from the RGS segments are included in gas volume calculations in AN-103,[b] AN-104, AN-105, and AW-101.

2. Nonconvective layer densities measured from 1996 cores from AN-103 and AN-104 are used in pressure and volume calculations (recent cores from AW-101 and AN-105 were already available for Stewart et al. [1996a]).

This section describes the updated volume calculations and the method by which the RGS void data were combined with the existing VFI measurements.

3.1.1 Average Void Fraction

The RGS void fractions are ascribed to their own risers to correctly capture the effect of improved spatial coverage. Because the RGS waste sample is 48 cm in length, which is approximately the vertical spacing between VFI measurements (30–60 cm), one RGS segment covers approximately the same vertical distance as two VFI samples.[c] Accordingly, each RGS result was converted to two data points: one at the reported value, the other allowed to vary randomly about the reported value to maintain the variance structure among the original RGS void data. The random variation was modeled by a normal distribution with zero mean and standard deviation equal to 10% of the data value, which is the approximate uncertainty ascribed to the RGS void measurement (Shekarriz et al. 1997). The elevation of both data points was set to the midpoint of the 48-cm (19-in.) sample. A single location was used because the distribution of gas in the segment is not known, and it is reasonable to use the midpoint for the average void.

(a) Density values were obtained from the LABCOR database by RL Bechtold on 12/18/96.
(b) The AN-103 RGS void fractions were corrected to account for changes in the extraction procedure for that tank and do not match the values given in Shekarriz et al. (1997).
(c) However, the 367-cm^3 VFI sample volume is actually larger than the 243 cm^3 of waste contained in a full RGS segment.

The VFI measurement error has a standard deviation of approximately ± 0.004 void fraction, which is negligible compared with uncertainty due to spatial nonuniformity of the void. The ± 10% measurement error of the RGS is modeled by adding random noise, as described above. The VFI void fraction is also multiplied by a factor of 1.1 before being combined with the RGS data to account for sample capture error (see Stewart et al. 1996a, Section 3.2.2, for a detailed discussion of VFI uncertainty). No sample capture error is applied to the RGS data. In all respects, the RGS void fraction is assumed to be equal in quality to a VFI measurement.

In some cases, a GRE occurred between the times the VFI and RGS were operated in a tank. Theoretically, this would place the two data sets in different populations. In reality, the gas releases are localized such that only a small fraction of the tank is disturbed. The volumes of gas released are much smaller than the uncertainty in the volume calculation. Only GREs in SY-101 prior to mixing caused a change in gas inventory large enough to potentially affect a VFI/RGS measurement, had the equipment been available at the time.

The average void fractions for the combined data set are computed with an ANOVA (analysis of variance) statistical procedure using a model that captures the major sources of uncertainty. The ANOVA model developed for averaging VFI data has the form

$$\alpha_{ijkl} = \bar{\alpha} + R_i + T_{j(i)} + D_k + RD_{ik} + TD_{j(i)k} + \varepsilon_{ijkl} \qquad (3.1.1)$$

where

$\bar{\alpha}$ = the mean void fraction in the tank
R_i = deviation of the void fraction at riser i from the mean
$T_{j(i)}$ = deviation of the void fraction of traverse j in riser i
D_k = the effect of kth layer (see discussion below)
RD_{ik} = the void fraction deviation at riser i and elevation k from the mean
$TD_{j(i)k}$ = deviation of the void fraction of traverse j and elevation k from the mean
ε_{ijkl} = sampling and instrument error (contains all uncertainty not accounted for in the terms above).

Each term in the model describes a source of variability in the measurement process. All terms except the mean void itself and the effect of layer, D, have a zero mean and represent deviation from the mean. Deviation due to interaction of traverse and elevation and riser and elevation are included in the terms TD and RD, respectively.

The model of Eq. (3.1.1) was modified to accommodate the void data from both sources by eliminating the terms involving "traverse within a riser." This source of uncertainty is not applicable to the RGS data. Removing the traverse terms increases the computed uncertainties ascribed to riser or to instrument and analytical errors or both. However, the overall uncertainty associated with layer mean void or tank mean void estimates are not noticeably affected.

The layers are chosen to be consistent with the overall waste configuration. The entire convective layer is treated as a single layer extending from the estimated base of the crust to the approximate top of the nonconvective layer. The latter elevation is chosen to be just above any significant void fractions (above 0.01) measured on the first pass. Higher void fractions in the convective layer from second or third pass measurements are discarded since they are assumed to result from gas released from below on the prior pass.

The nonconvective layer is split into two or three sublayers with boundaries determined by a visual interpretation of the variation in void fraction. The number and thickness of the sublayers are arbitrary, but each is chosen to yield a fairly uniform vertical void distribution. The ANOVA

model emphasizes predicting the mean void fraction in each layer of a tank. For estimating the total gas volume stored in a tank, this is more important than predicting the exact void fraction profile.

Although measurements are made in only a few risers (two VFI and two RGS), it is legitimate to estimate horizontal variation based on the data. There remains a potential for missing important horizontal variation, but if the void profile in the two risers is nearly the same, the chance of an undetected nonuniformity is small. Likewise, if the two risers show a very different void profile, it is unlikely that the uncertainty due to any undetected void variation would be larger. This procedure has been used to estimate the horizontal variation of tank chemical contents based on core samples from two risers (Hartley et al. 1995).

Table 3.1.1 shows the mean void in the nonconvective layer and the sources of uncertainty in the ANOVA model both before and after including RGS data. The column labeled R is the uncertainty ascribed to the riser, RD is that due to interaction of riser and layer, T and TD are the uncertainty of VFI traverse and interaction of traverse and layer (not used with RGS data), and ε is the remainder of the uncertainty, which could be considered the combination of sampling and instrumentation error. A zero riser uncertainty, R, does not imply that the void distribution is the same for all risers, but that more of the uncertainty is ascribed to the mismatch of individual layer void fractions between risers. The overall uncertainty due to lateral nonuniformity might best be characterized by the root-mean-square of R and RD. The total uncertainty is the square root of the sum of the squares of the uncertainty components. This is the expected uncertainty of a single measurement with respect to the mean. The uncertainty in the average is much lower.

Including the RGS data reduced the average void fraction in AW-101 and increased it slightly in Tanks AN-104 and AN-105. The overall uncertainty increased slightly in AN-104 and AN-105 but was unchanged in AW-101. The uncertainty in an individual void measurement increased significantly in all three tanks for which RGS data were used.

3.1.2 Gas Retention Model

The gas retention model comprises the calculation of in-situ and standard gas volume in each waste layer and in the whole tank from the average void fraction determined from the ANOVA model above. The model is essentially the same as that used in Stewart et al. (1996a), with some improvements to reflect better information and minor corrections as follows:

Table 3.1.1. Distribution of Void Measurement Uncertainties

Tank	Mean NC[a] Void (%)	Uncertainty (Void %)					
		R	RD	T	TD	ε	Total
SY-103 (VFI only)	6.0 ± 2.0	2.8	1.4	-	-	2.1	3.8
AW-101 (VFI only)	4.7 ± 0.5	0	0	0.9	0.7	1.4	1.8
(VFI + RGS)	3.8 ± 0.5	0.3	0.7	-	-	2.7	2.8
AN-103 (VFI only)	12.2 ± 0.4	0	0.1	0	0	4.3	4.3
(VFI + RGS)	10.7 ± 1.0	0	7.0	-	-	2.5	7.5
AN-104 (VFI only)	5.9 ± 0.4	0	0.3	0	0	1.4	1.4
(VFI + RGS)	6.2 ± 0.9	0	4.6	-	-	2.1	5.1
AN-105 (VFI only)	3.8 ± 0.6	1.1	0.4	0	0	1.2	1.7
(VFI + RGS)	4.2 ± 0.7	0.9	1.7	-	-	2.0	2.8

(a) Nonconvective layer.

1. Void fraction is included in nonconvective layer densities for pressure calculations in each layer.
2. Indications derived from thermocouple tree temperature profiles were eliminated from determining the average nonconvective layer depth. This affects all tanks except SY-101.
3. Crust gas volume calculation assumes crust consists of nonconvective layer material floating at a specified submergence.
4. The effective pressure of the gas held in the crust is computed from the hydrostatic pressure gradient rather than 1 atm.

The volume calculation procedure is explained below with these improvements emphasized as they apply.

Given the average void fraction, α_i, of a given layer, i, the in-situ volume, V_i, of the layer is the product of the void fraction, layer height, H_i, and the tank area, A:

$$V_i = \alpha_i A H_i \tag{3.1.2}$$

The standard volume of each layer, $\hat{V}_i$, is the product of the in-situ volume and the corrections for standard pressure and temperature conditions:[a]

$$\hat{V}_i = V_i \frac{p_i}{\hat{p}} \frac{\hat{T}}{T_i} \tag{3.1.3}$$

where p_i is the layer effective pressure, $\hat{p}$ is the standard atmospheric pressure at sea level (101,325 Pa), $\hat{T}$ is the standard temperature (288.15K), and T_i is the layer average temperature taken from available temperature profile measurements. The small variations in local ambient pressure due to weather and the ~200 m (700 ft) elevation of the Hanford tank farms are neglected in the pressure correction.

It is convenient to define an effective pressure ratio that includes both pressure and temperature corrections to standard conditions. The definition is

$$P_i = (p_i / \hat{p})(\hat{T} / T_i) \tag{3.1.4}$$

For a uniform void distribution, the pressure in Eq. (3.1.3) and (3.1.4) is equal to the local pressure at the midpoint of the layer. The pressure in layer i is calculated as the hydrostatic pressure exerted by the material above the midpoint of the layer.

The nonconvective layer densities obtained from core samples are assumed to represent degassed waste. However, the dimensions of the waste layers include the expansion due to accumulated gas. Therefore, the density used to calculate the local pressure should by reduced to account for the void fraction. The pressure in a nonconvective sublayer i is calculated by

$$p_i = \hat{p} + g\left[\rho_L(f_S H_{CR} + H_{CL}) + \rho_{NC}\left(\sum_{j<i} H_j(1-\alpha_j) + \tfrac{1}{2} H_i(1-\alpha_i)\right)\right] \tag{3.1.5}$$

(a) Standard conditions are taken from "U.S. Standard Atmosphere, 1976" as defined in *CRC Handbook of Chemistry and Physics, 71st Edition,* DR Lide, editor. CRC Press, Boston.

where ρ_L and ρ_{NC} are the liquid and degassed nonconvective layer densities, respectively; H_{CR} and H_{CL} are the crust and convective layer thickness, respectively; f_S is the fraction of crust submerged (see Figure 3.1.1 and discussion below); H_i is the nonconvective sublayer thickness; and α_i is the sublayer void fraction.

The convective layer thickness is measured from the bottom of the crust to the top of the nonconvective layer as given by

$$H_{CL} = L_W - H_{CR} - H_{NC} \tag{3.1.6}$$

where L_W is the measured tank waste level. The convective layer pressure is given similarly to Eq. (3.1.5) by

$$p_{CL} = \hat{p} + \frac{g}{2}\rho_{CL}(f_S H_{CR} + H_{CL}) \tag{3.1.7}$$

The elevation of the top of the nonconvective layer, H_{NC}, is estimated from the combination of available measurements. Those available include elevations determined from the ball rheometer, temperature profiles from the multifunction instrument tree (MIT) and the old thermocouple trees, MIT validation probe runs, and core samples to compute the average nonconvective layer height for the tank. Since the uncertainty in the elevation using the old thermocouple tree temperature profiles was an order of magnitude higher than that of the other measurements, we decided not to include it in the average. This changed the average nonconvective layer height by 1–5 cm and approximately halved the uncertainty compared to those calculated in Stewart et al. (1996a).

The total in-situ gas volume in the nonconvective waste is the sum of the gas volumes in the nonconvective sublayers:

$$V_{NC} = A\sum_{i=1}^{NC}\alpha_i H_i \tag{3.1.8}$$

The total standard volume is similarly computed, making use of Eq. (3.1.4), as

$$\hat{V}_{NC} = A\sum_{i=1}^{NC}\alpha_i H_i P_i \tag{3.1.9}$$

The overall average void fraction for the entire nonconvective layer can be determined from

$$\alpha_{NC} = \frac{\hat{V}_{NC}}{AH_{NC}} = \frac{1}{H_{NC}}\sum_{i=1}^{NC}\alpha_i H_i \tag{3.1.10}$$

For the nonconvective layer, the average pressure ratio is defined, again using Eq. (3.1.4), as

$$P_{NC} = \frac{\hat{V}_{NC}}{V_{NC}} = \frac{1}{H_{NC}\alpha_{NC}}\sum_{i=1}^{NC}\alpha_i H_i P_i \tag{3.1.11}$$

The convective layer in-situ gas volume is computed from the average convective layer void fraction as

$$V_{CL} = A\alpha_{CL}H_{CL} \tag{3.1.12}$$

The standard volume in the convective layer is the product of the in-situ volume and the pressure ratio derived from Eq. (3.1.4) and (3.1.7) as

$$\hat{V}_{CL} = V_{CL}P_{CL} \tag{3.1.13}$$

The crust volume calculation is the most significant change from the calculations in Stewart et al. (1996a), reducing the estimated gas volume in the crust by about half. The original calculation was derived for SY-101 (Brewster et al. 1995) and conservatively assumed a crust density of 2.0 g/cc floating on a liquid with a density of 1.46 g/cc (approximately that of centrifuged liquid from Window E samples). A void fraction of 0.25 was required to float this crust.

Observations from recent core samples indicate that the crust probably consists of the same material as the nonconvective layer. The extrusion photos from the few recent DST core samples that included crust material show that the crust and nonconvective layer have a very similar appearance (see Figures 3.4.2, 3.4.5, and 3.4.6). At the same time, the single RGS void fraction measurement from the crust of AN-103 indicates a void fraction of about 0.15, which is close to the estimated neutral buoyancy value and of the same magnitude as the peak void fraction in the nonconvective layer.

Consistent with these observations, the new model assumes that the crust consists of nonconvective layer material floating at slightly above neutral buoyancy such that a large fraction of its thickness, f_s, is submerged below the free liquid surface. The submergence fraction determines how much the crust void fraction exceeds the neutral buoyancy value. This model is illustrated in Figure 3.1.1. That portion above the surface is assumed to have the same void fraction as that below, but some of the liquid has drained away and occupies only a fraction of the porosity in the non-void region.

The density of the material above the free liquid surface in Figure 3.1.1 is given by

$$\rho_1 = [\rho_S(1-\phi) + \rho_L\phi\psi](1-\alpha_{CR}) \tag{3.1.14}$$

where ρ_s and ρ_L are the solid and liquid densities, respectively; ϕ is the porosity; ψ is the fraction of porosity occupied by liquid; and α is the void fraction. The density below the liquid surface is

$$\rho_2 = [\rho_S(1-\phi) + \rho_L\phi](1-\alpha_{CR}) = \rho_{NC}(1-\alpha_{CR}) \tag{3.1.15}$$

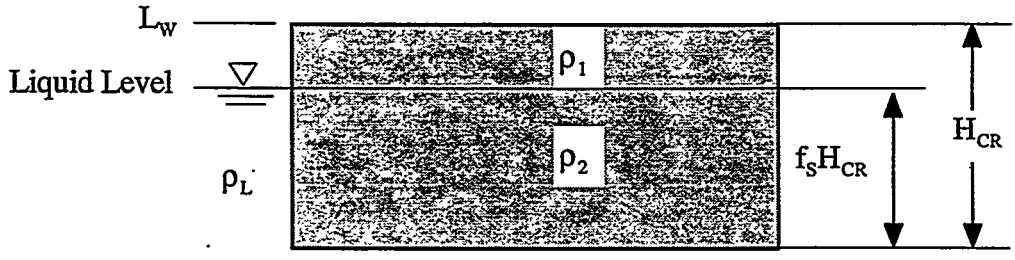

Figure 3.1.1. Floating Crust Model

Balancing the weight of the crust with buoyancy using Archimedes' principle and solving for the crust void fraction yields

$$\alpha_{CR} = 1 - \frac{f_S \rho_L}{\rho_{NC} - (1-f_S)(1-\psi)\rho_L \phi} \tag{3.1.16}$$

With $f_S = 1$, Eq. (3.1.16) degenerates to the expression for the neutral buoyancy void fraction.

As yet we have no reliable data on porosity or the moisture fraction, ψ, in the unsubmerged portion. However, with the $(1-f_s)$ coefficient, Eq. (3.1.16) is not very sensitive to the choice of values for these parameters. Assuming a porosity of 0.4 [(a)] and that capillary forces pull sufficient moisture into the unsubmerged portion that half of its porosity is occupied by liquid (ψ=0.5), Eq. (3.1.16) becomes

$$\alpha_{CR} = 1 - \frac{f_S \rho_L}{\rho_{NC} - 0.2(1-f_S)\rho_L} \tag{3.1.17}$$

where $\phi(1-\psi)=0.4*(1-0.5)=0.2$.

The value of the submergence fraction is quite subjective since there is a void measurement in only one tank. A submergence fraction of 0.95 was chosen for AN-103 so that the crust void fraction given by Eq. (3.1.17) agrees with the RGS measurement of 0.15. The difference between the two level instruments in SY-101 is about 18 cm, which indicates that only 82–85% of the crust is submerged. However, this yields a void fraction of over 0.20, which is far above neutral buoyancy. Thus we arbitrarily chose a 90% submergence, for a void fraction of 0.16. The submergence fraction in other tanks was chosen in the same subjective way.

The effective pressure is the hydrostatic pressure at the midpoint of the submerged portion of the crust:

$$p_{CR} = \hat{p} + \frac{g}{2}\rho_{CL} f_S H_{CR} \tag{3.1.18}$$

The gas in the crust was assumed to be held at 1 atm in the original model. While this is a good approximation, a better estimate is obtained using the hydrostatic pressure gradient.

The in-situ crust gas volume calculated using the void fraction from Eq. (3.1.17). The standard crust volume corrects the in-situ volume to standard conditions using Eq. (3.1.18) along with Eq. (3.1.4). The crust in-situ and standard volumes are given, respectively, by

$$V_{CR} = A\alpha_{CR} f_S H_{CR} \tag{3.1.19}$$

$$\hat{V}_{CR} = V_{CR} P_{CR} \tag{3.1.20}$$

The total in-situ and standard gas volumes in the entire tank are the sums of the contributions of individual layers. They are given, respectively, by

---

(a) Saltcake porosity was estimated at 0.3 to 0.4 in an unpublished report on BY-107 pumping tests by WP Metz in 1976: "A topical report on interstitial liquid removal from Hanford salt cakes," ARH-CD-545. The "drainable porosity" from saltwell pumping records in Caley et al. (1996) shows a range from <0.1 to 0.66 with an average around 0.4.

$$V_G = V_{NC} + V_{CL} + V_{CR} \tag{3.1.21}$$

$$\hat{V}_G = \hat{V}_{NC} + \hat{V}_{CL} + \hat{V}_{CR} \tag{3.1.22}$$

The overall tank effective pressure ratio is computed as the ratio of standard volume to in-situ volume.

$$P_{EFF} = \frac{\hat{V}_G}{V_G} \tag{3.1.23}$$

The degassed level represents the waste level after all the in-situ retained gas in the nonconvective layer was removed. It is computed by

$$L_{NO-GAS} = L_W - V_{NC}/A \tag{3.1.24}$$

3.1.3 Gas Volume Uncertainties

In general, uncertainties given represent one standard deviation and are estimated by linear propagation through their defining equations, assuming each parameter was independent. If y is a function of N variables, $y = F(x_1, x_2, \ldots x_N)$, each with uncertainty, σ_i, the standard error is expressed as

$$\sigma_F = \sqrt{\sum_{i=1}^{N}\left(\frac{\partial F}{\partial x_i}\sigma_i\right)^2} \tag{3.1.25}$$

The uncertainties in the in-situ and standard gas volume in each layer depend mainly on the uncertainty of mean void fraction in that layer. However, the uncertainties of layer height, pressure, and temperature are included for completeness. Based on Eq. (3.1.2), (3.1.3), and (3.1.25), these are expressed as

$$\sigma_{Vi} = A\sqrt{(H_i\sigma_{\alpha i})^2 + (\alpha_i\sigma_{Hi})^2} \tag{3.1.26}$$

and

$$\sigma_{\hat{V}i} = \sqrt{[p_i/\hat{p}(\hat{T}/T_i)\sigma_{Vi}]^2 + [V_i/\hat{p}(\hat{T}/T_i)\sigma_{Pi}]^2 + [V_i(p_i/\hat{p})(\hat{T}/T_i^2)\sigma_{Ti}]^2} \tag{3.1.27}$$

where the uncertainty in the void fraction is provided by the statistical model described in Section 3.2.3. Except for the convective layer, the layer heights are assigned and their uncertainty is zero. In the former, the uncertainties of the waste surface level and crust thickness are included.

The uncertainties of total in-situ and standard gas volumes in the nonconvective layer include the covariances of the layer void fractions. The covariances exist because the estimates of mean void fraction in each layer are not independent; they share a common deviation due to riser (horizontal variability). The uncertainties, derived from Eq. (3.1.26) and (3.1.27), are given by

$$\sigma_{V_{NC}} = \sqrt{\sum_{i=1}^{NC} \sigma_{Vi}^2 + A^2 \sum_{i \neq j} 2H_i H_j \, \mathrm{cov}(\alpha_i, \alpha_j)} \qquad (3.1.28)$$

and

$$\sigma_{\hat{V}_{NC}} = \sqrt{\sum_{i=1}^{NC} \sigma_{\hat{V}i}^2 + A^2 \sum_{i \neq j} 2(HP)_i (HP)_j \, \mathrm{cov}(\alpha_i, \alpha_j)} \qquad (3.1.29)$$

where $\mathrm{cov}(\alpha_i,\alpha_j)$ represents the covariance of mean void fraction between layers i and j, calculated from the estimate of riser variability and the structure of the ANOVA model. Covariances of the layer pressures and temperatures are considered to be negligible and are not included.

3.1.4 Retained Gas Volume Summary

The input values and results of the volume calculations for all six tanks are summarized in Table 3.1.2. All uncertainties in the table represent one standard deviation. The effect of episodic GREs on any of the waste parameters shown in Table 3.1.2 is insignificant. The typical GRE in SY-101 before mixing released a major fraction of the stored gas inventory and rearranged much of the waste. This is not the case in any other tank. The typical GRE is very small and local; waste temperatures are usually not measurably affected,[a] and the gas release volumes are much less than the uncertainty in the standard gas volume estimates.

The following is an explanation of the nomenclature used in Table 3.1.2:

1. Input Data

Waste Level (cm)	Waste level measured by Enraf or Food Instrument Corporation (FIC) gauge at approximately the time of the VFI measurements.
Dome Vol. (m^3)	Volume of the head space above the waste level.
CL Den. (kg/m^3)	Mean convective layer density determined from ball rheometer measurements.
NC Den. (kg/m^3)	Mean nonconvective layer density determined from core samples.

2. Nonconvective Layer

Thickness (cm)	Thickness of the nonconvective layer as determined from averaging indications from the ball rheometer, temperature profiles (MIT only), and core samples, as available.
Mean Void (%)	Average gas volume fraction computed from VFI and RGS data using the ANOVA model represented by Eq. (3.1.1). Only VFI data are available for SY-101 and SY-103.

(a) The temperature profiles in AN-105 and SY-103 have occasionally showed small changes before and after GREs.

Table 3.1.2. Best Estimate Retained Gas Volume Summary

	AN-103	AN-104	AN-105	AW-101	SY-101[a,b]	SY-103[b]
Input Data						
1. Waste Level (cm)	884±5	979±4	1041±7	1040±7	1019±5	691±3
2. Dome Vol. (m^3)	1712±20	1323±18	1066±21	1070±30	1159±22	2503±13
3. CL Den. (kg/m^3)	1530±50	1440±30	1430±30	1430±30	1600±30	1470±30
4. NC Den. (kg/m^3)	1730±110	1590±60	1590±40	1570±30	1700±43	1570±50
Nonconvective Layer						
5. Thickness (cm)	379±9	415±9	452±11	283±22	200±0	334±25
6. Mean Void (%)	10.7±1.1	6.2±0.9	4.2±0.8	3.8±0.6	4.5±0.7	6.4±2.1
7. In-Situ Vol.(m^3)	167±16	105±15	77±15	44±6	37±5	88±27
8. Eff. Pres. Ratio	1.88±0.04	1.97±0.03	2.09±0.04	2.11±0.04	2.24±0.05	1.69±0.05
9. Std. Volume (m^3)	314±31	207±28	161±30	94±13	83±12	148±45
Convective Layer						
10. Thickness (cm)	413±16	524±10	559±11	693±19	717±22	337±19
11. Mean Void (%)	0.4±1.6	0.4±1.3	0.5±1	0.3±0.8	0.8±0.7	0.4±2
12. In-Situ Vol. (m^3)	8±27	9±28	10±23	8±23	23±21	5±29
13. Eff. Pres. Ratio	1.44±0.04	1.42±0.02	1.43±0.02	1.56±0.03	1.70±0.05	1.27±0.02
14. Std. Vol. (m^3)	10±36	12±37	14±31	12±34	35±33	6±35
Crust Layer						
15. Thickness (cm)	92±20	40±10	30±10	64±15	102±30	20±10
16. Submerged Fraction	0.95±0.03	0.98±0.01	0.98±0.01	0.92±0.05	0.90±0.10	0.98±0.01
17. Void (%)	15±6	11±4	12±3	15±5	16±10	8±4
18. In-Situ Vol. (m^3)	55±26	18±8	14±6	36±15	62±41	6±4
19. Eff. Pres. Ratio	1.02±0.01	0.99±0.01	0.98±0.01	1.00±0.01	1.03±0.01	0.97±0.01
20. Std. Vol. (m^3)	56±25	17±7	14±6	36±15	64±40	6±4
Whole Tank						
21. In-Situ Vol. (m^3)	229±41	132±33	101±34	89±30	122±48	99±56
22. Eff. Pres. Ratio	1.7±0.10	1.8±0.12	1.9±0.13	1.6±0.13	1.5±0.22	1.6±0.13
23. Std. Vol. (m^3)	380±54	236±47	189±53	141±43	181±57	160±78
24. Degassed Level (cm)	843±5	953±5	1022±5	1030±3	1010±5	670±7

(a) SY-101 data represent post-mixer pump conditions.
(b) SY-101 and SY-103 entries based on VFI data only.

In-Situ Vol. (m^3)	Gas volume existing at the local pressure and temperature (Eq. 3.1.8).
Eff. Pres. Ratio	The factor required to convert in-situ volume to standard pressure and temperature. Includes both temperature and pressure correction (Eq. 3.1.11)
Std. Vol. (m^3)	Stored gas volume at standard pressure and temperature (Eq. 3.1.9).

3. Convective Layer

Thickness (cm)	Thickness of the convective layer from the bottom of the crust to the top of the nonconvective layer (Eq. 3.1.6)
Mean Void (%)	See #2.
In-Situ Vol. (m^3)	Gas volume existing at the local pressure and temperature (Eq. 3.1.12).
Eff. Pres. Ratio	The factor required to convert in-situ volume to standard pressure and temperature. Includes both temperature and pressure correction (Eq. 3.1.7 and 3.1.4)
Std. Vol. (m^3)	Stored gas volume at standard pressure and temperature (Eq. 3.1.13).

4. Crust Layer

Thickness (cm)	Crust thickness as determined from MIT validation probe temperature profiles, core samples, or other indications.
Submerged Fraction	Fraction of crust estimated submerged below the free liquid level.
Void Fraction	Gas volume fraction required to float the crust Eq. (3.1.17).
In-Situ Vol. (m^3)	Gas volume existing at the local pressure and temperature (Eq. 3.1.19).
Eff. Pres. Ratio	The factor required to convert in-situ volume to standard pressure and temperature. Includes both temperature and pressure correction (Eq. 3.1.18 and 3.1.4).
Std. Vol. (m^3)	Stored gas volume at standard pressure and temperature (Eq. 3.1.20).

5. Whole Tank

In-Situ Vol. (m^3)	Sum of in-situ volume of crust, convective, and nonconvective layers (Eq. 3.1.21).
Eff. Pres. Ratio	The overall effective pressure ratio for the entire tank. Equal to the standard volume divided by the in-situ volume (Eq. 3.1.23).
Std. Vol. (m^3)	Sum of the standard volumes of crust, convective, and nonconvective layers (Eq. 3.1.22).
Degassed Level (cm)	The waste level (see #1) less the nonconvective layer in-situ volume (see #2) divided by tank area (Eq. 3.1.24).

3.2 Individual Tank Gas Retention Summaries

Retained gas volume calculations for each tank are given in Sections 3.2.1 through 3.2.6. The local void fraction measurements are plotted along with the location of risers from which the measurements were made and other important instrumentation. The detailed gas volume calculations are given for each waste layer in a table for each tank. Note that, since no RGS void measurements were made in SY-101 and SY-103, the data for these two tanks are unchanged from Stewart et al. (1996a) except for crust volume estimates.

Many of the void distributions plotted in the subsections that follow reveal regions in which the local void fraction exceeds the neutral buoyancy void fraction. This could be taken to indicate that a buoyant displacement ("rollover") is imminent. But only comparing the local void to the neutral buoyancy void does not predict incipient buoyant displacements for three main reasons. First, there is considerable uncertainty in the neutral buoyancy void fraction. The neutral buoyancy void fraction is the gas fraction necessary to make the density of nonconvective layer material locally equal to the supernatant liquid above it. It can be expressed as

$$\alpha_{NB} = 1 - \frac{\rho_{CL}}{\rho_{NC}} \qquad (3.2.1)$$

Eq. (3.2.1) amplifies the uncertainties in the layer densities resulting in 50–60% uncertainty in the neutral buoyancy void (see row 8 in Table 4.2.2). Second, the yield strength of the nonconvective layer material makes the void fraction required for an instability higher than the neutral buoyancy value, as discussed in Section 4.3.

Third, and most importantly, the net buoyancy integrated from the top down, not the local void fraction, determines whether a buoyant displacement can occur. For example, Figure 3.2.9 shows that AN-103 has a 200-cm layer in which the local void far exceeds the neutral buoyancy void fraction of $12 \pm 6\%$. But this region lies beneath a layer in which the local void fraction is considerably lower. The integration of net buoyancy confirms that AN-103 is stable by a small margin considering only neutral buoyancy and by a more comfortable margin considering the additional effect of material strength.

3.2.1 SY-101 Void Distribution and Gas Volume

No further core sampling or RGS data are available for SY-101. The only changes in the gas volume result from revisions to the model, as discussed above, with the most significant being a reduction in estimated crust gas volume. The locations of important instruments and VFI and ball rheometer tests are shown in Figure 3.2.1, and the void profile is given in Figure 3.2.2. The gas volume calculations in each sublayer are summarized in Table 3.2.1.

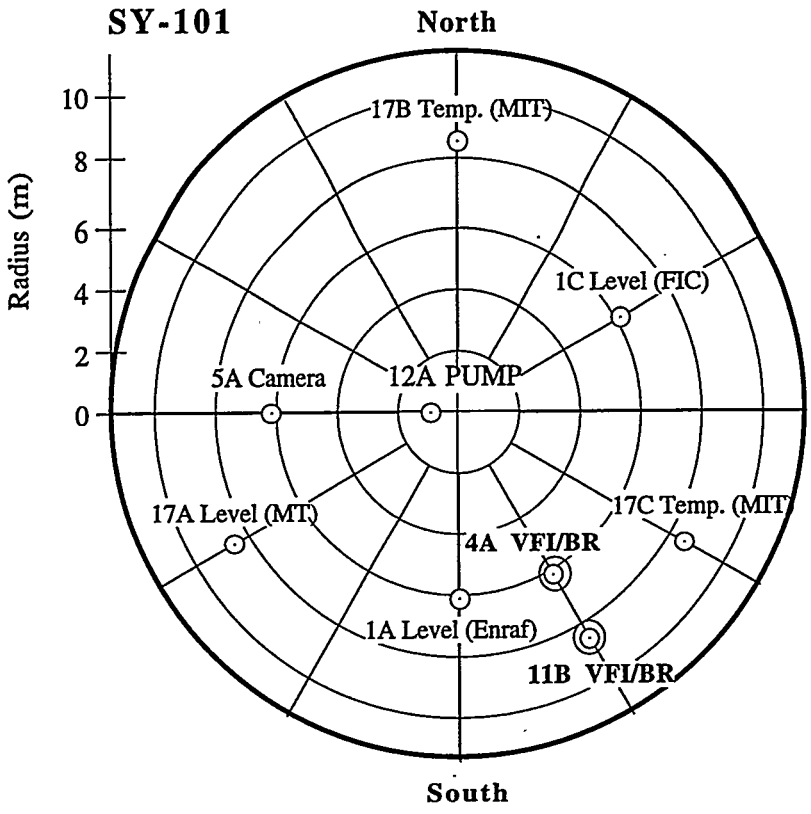

Figure 3.2.1. SY-101 Sample and Instrumentation Risers

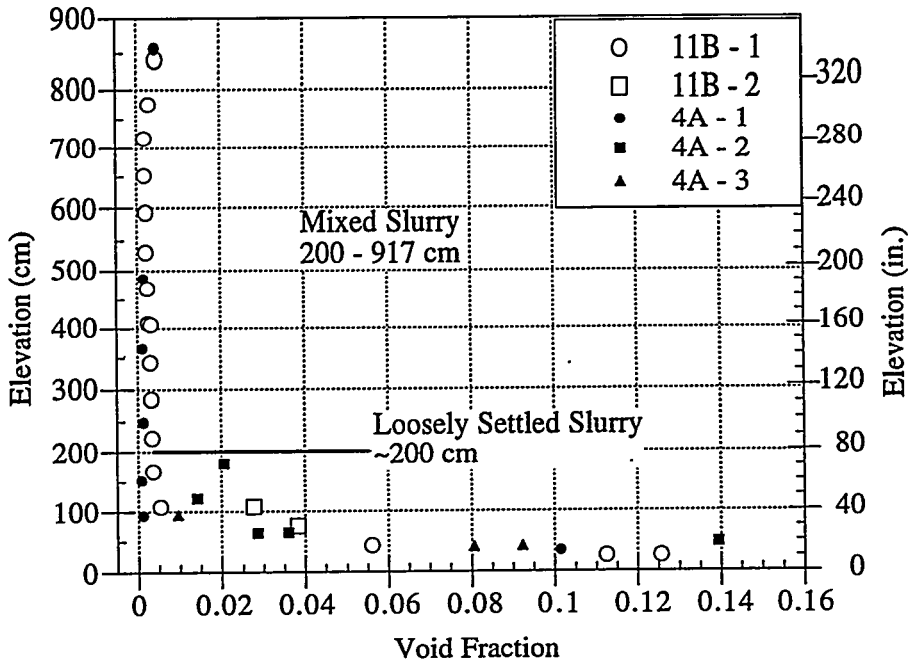

Figure 3.2.2. SY-101 Void Profile

Table 3.2.1. Retained Gas Volume in SY-101

Layer ID, Dimensions (cm)	Mean Void (%)	In-situ Volume (m^3)	Pressure Ratio	Standard Volume (m^3)
Crust 917 - 1019	16 ± 10	62 ± 41	1.03 ± 0.02	64 ± 40
#0 200 - 917	0.8 ± 0.7	23 ± 21	1.63 ± 0.05	35 ± 33
#1 60 - 200	1.5 ± 0.7	9 ± 4	2.13 ± 0.06	18 ± 9
#2 0 - 60	11.6 ± 0.8	28 ± 2	2.27 ± 0.06	65 ± 5
Total (or Avg.)	N/A	122 ± 48	1.49 ± 0.22	181 ± 57

3.2.2 SY-103 Void Distribution and Gas Volume

No further core sampling or RGS data are available for SY-103. The only changes in the gas volume result from revisions to the model, as discussed above, with the most significant change being a reduction in estimated crust gas volume. The locations of important instruments and VFI and ball rheometer tests are shown in Figure 3.2.3, and the void profile is given in Figure 3.2.4. The gas volume calculations in each sublayer are summarized in Table 3.2.2.

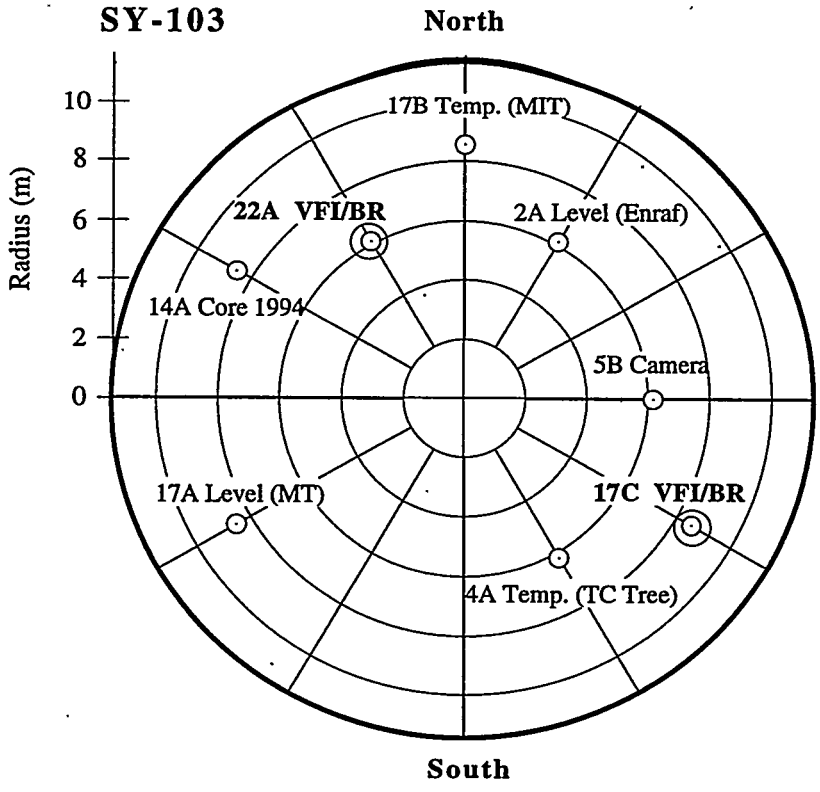

Figure 3.2.3. SY-103 Sample and Instrumentation Risers

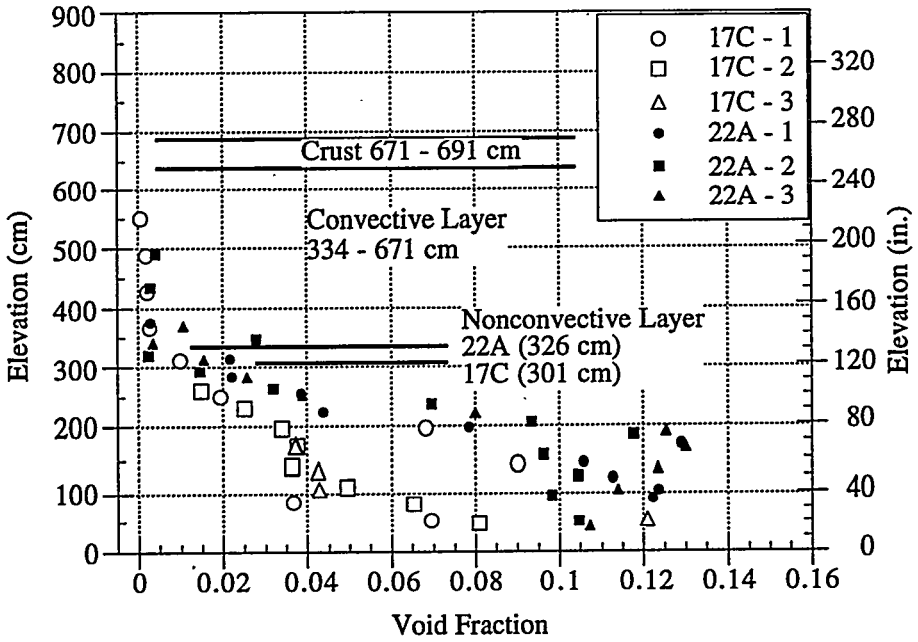

Figure 3.2.4. SY-103 Void Profile

Table 3.2.2. Retained Gas Volume in SY-103

Layer ID, Dimensions (cm)	Mean Void (%)	In-Situ Volume (m^3)	Pressure Ratio	Standard Volume (m^3)
Crust 671–691	7.9 ± 3.6	6 ± 4	0.97 ± 0.01	6 ± 4
Convective 334–671	0.4 ± 2.1	5 ± 29	1.22 ± 0.02	6 ± 35
#1 207–334	1.8 ± 2.1	9 ± 11	1.51 ± 0.04	14 ± 16
#2 0–207	9.2 ± 2.0	78 ± 17	1.73 ± 0.05	134 ± 29
Total Nonconvective	6.4 ± 2.1	88 ± 27	1.69 ± 0.05	148 ± 45
Total Tank	NA	99 ± 56	1.62 ± 0.13	160 ± 78

3.2.3 AW-101 Void Distribution and Gas Volume

Core samples and RGS void measurements were obtained from two additional risers in AW-101 in March and May 1996, six and seven months after VFI and ball rheometer testing. Four GREs were observed in standard hydrogen monitoring system (SHMS) data in AW-101 between VFI and RGS tests, and another took place between core sampling in risers 24A and 24B (Wilkins et al. 1996). One GRE, on December 29, 1995, was relatively large. Approximately the same number and size of GREs occurred in the six months prior to VFI operation. The risers tested and the location of important instruments are shown in Figure 3.2.5, and the void profile, including RGS and VFI values, is given in Figure 3.2.6. Combining RGS voids with the

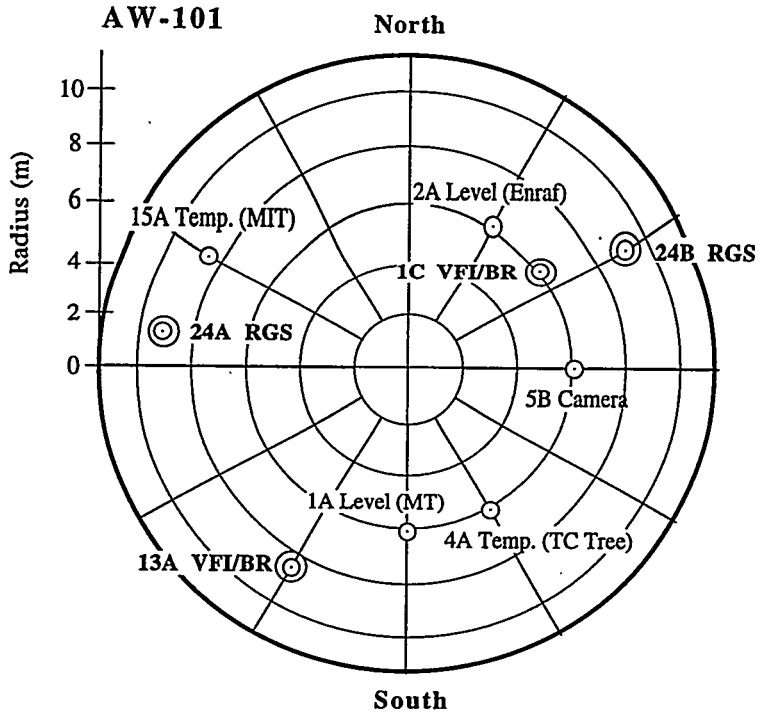

Figure 3.2.5. AW-101 Sample and Instrumentation Risers

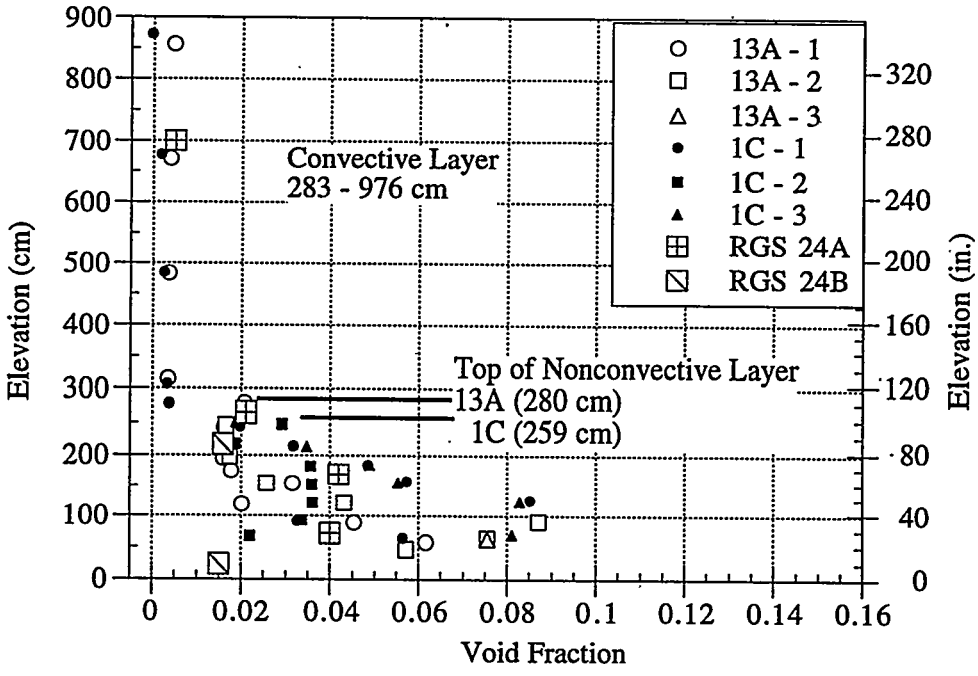

Figure 3.2.6. AW-101 Void Profile

existing VFI data set reduces the nonconvective layer gas volume by about 25%, and the revised crust model lowers the crust gas volume by about 40%. The total standard volume decreased by about 32%. The gas volume calculations in each sublayer are summarized in Table 3.2.3.

Table 3.2.3. Retained Gas Volume in AW-101

Layer ID, Dimensions (cm)	Mean Void (%)	In-situ Volume (m^3)	Pressure Ratio	Standard Volume (m^3)
Crust 976 - 1040	15 ± 5.2	36 ± 15	1.00 ± 0.01	36 ± 15
Convective 283 - 976	0.3 ± 0.8	8 ± 23	1.50 ± 0.02	12 ± 34
#1 190 - 283	2.0 ± 0.7	8 ± 3	1.96 ± 0.05	15 ± 6
#2 140 - 190	4.0 ± 0.8	8 ± 2	2.03 ± 0.05	17 ± 3
#3 0 - 140	5.0 ± 0.6	28 ± 4	2.15 ± 0.05	62 ± 8
Total Nonconvective	3.8 ± 0.6	44 ± 6	2.11 ± 0.04	93 ± 12
Total Tank	NA	89 ± 30	1.60 ± 0.13	141 ± 43

3.2.4 AN-103 Void Distribution and Gas Volume

Core samples and RGS void measurements were obtained in AN-103 in two additional risers in September 1996, four months after VFI and ball rheometer testing. There were no GREs between the VFI and RGS tests (Wilkins et al. 1996). The gas volume calculations using the updated models in each sublayer are summarized in Table 3.2.4. The risers tested and the location of important instruments are shown in Figure 3.2.7, and the void profile, including both RGS and VFI values, is given in Figure 3.2.8.

Table 3.2.4. Retained Gas Volume in AN-103

Layer ID, Dimensions (cm)	Mean Void (%)	In-Situ Volume (m^3)	Pressure Ratio	Standard Volume (m^3)
Crust	15 ± 7	55 ± 26	1.02 ± 0.01	56 ± 25
Convective 379–792	0.4 ± 1.6	8 ± 27	1.38 ± 0.03	10 ± 36
#1 267–379	7.3 ± 2.0	15 ± 5	1.64 ± 0.05	24 ± 8
#2 140–267	10.9 ± 1.4	85 ± 11	1.80 ± 0.05	152 ± 20
#3 0–140	11.8 ± 1.9	68 ± 11	2.02 ± 0.06	139 ± 23
Total Nonconvective	10.7 ± 1.1	167 ± 16	1.88 ± 0.04	314 ± 31
Total Tank	N/A	229 ± 41	1.66 ± 0.10	380 ± 54

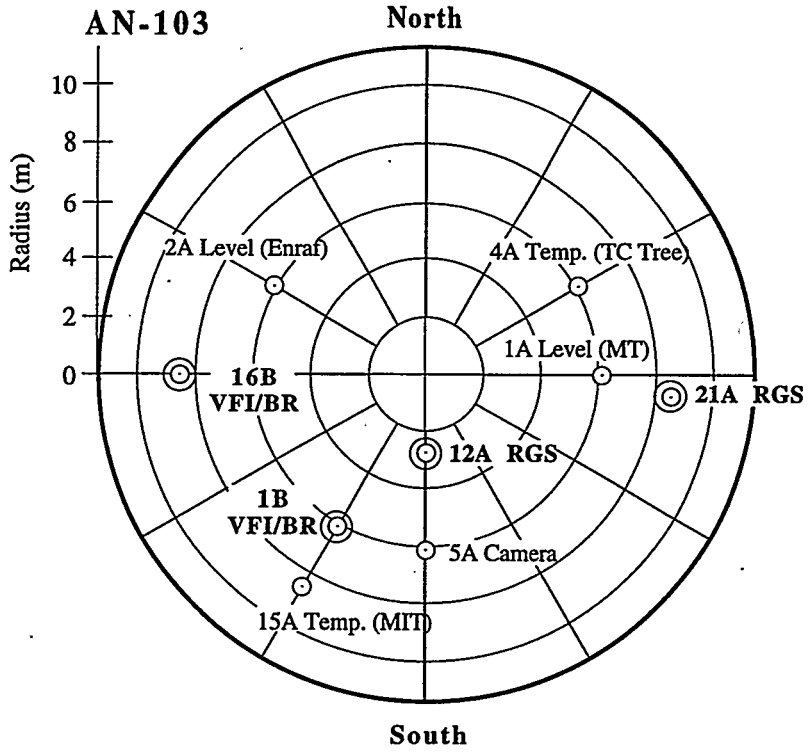

Figure 3.2.7. AN-103 Sample and Instrumentation Risers

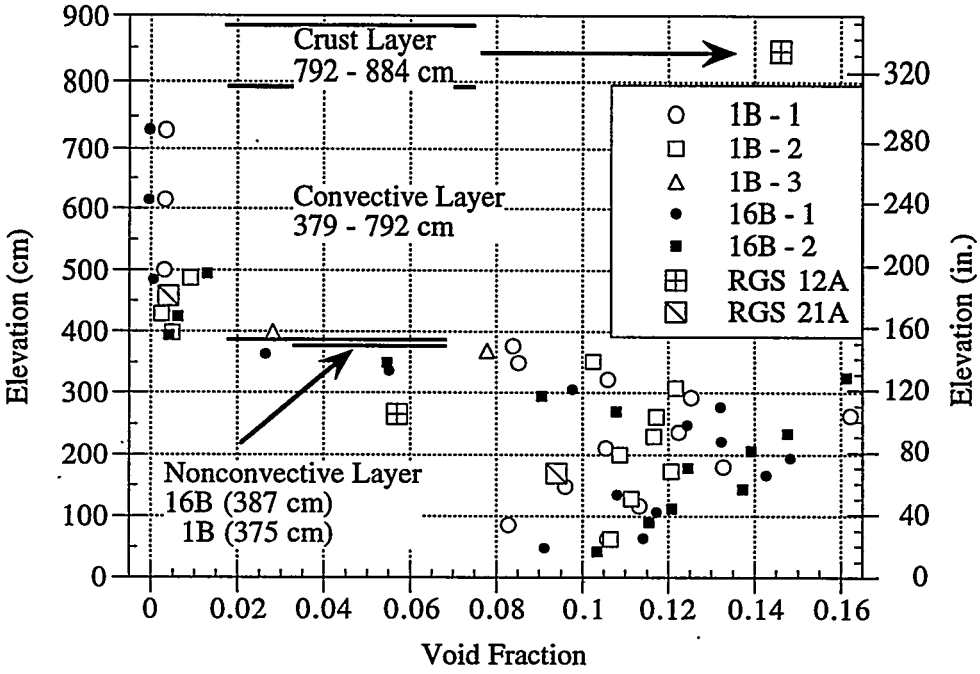

Figure 3.2.8. AN-103 Void Profile

3.2.5 AN-104 Void Distribution and Gas Volume

In August and September 1996, four and five months after VFI and ball rheometer testing, core samples and RGS void measurements were obtained in two additional risers in AN-104. One relatively large GRE was observed in the SHMS data in AN-104 three months before the RGS tests (Wilkins et al. 1996). A similar large GRE occurred six months before VFI operation.

The risers tested and the locations of important instruments are shown in Figure 3.2.9. Note that all four risers tested are essentially in one quadrant of the tank. The void profile, including both RGS and VFI values, is given in Figure 3.2.10. The RGS supplies an important measurement near the tank bottom that the VFI did not cover. Combining RGS voids with the existing VFI data set increases the nonconvective layer gas volume by about 5%, and the revised crust model lowers the crust gas volume by about 50%. The total standard volume increased by about 4%. The gas volume calculations in each sublayer are summarized in Table 3.2.5.

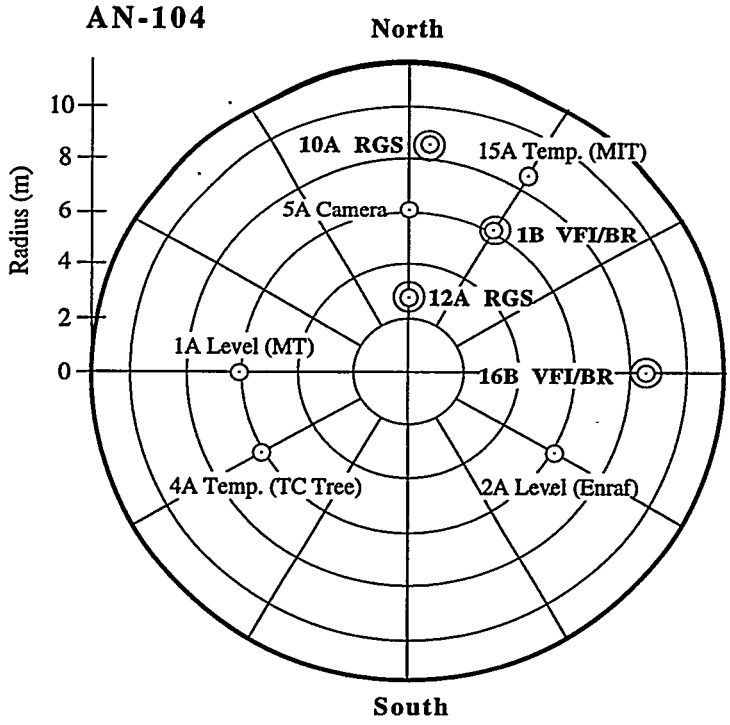

Figure 3.2.9. AN-104 Sample and Instrumentation Risers

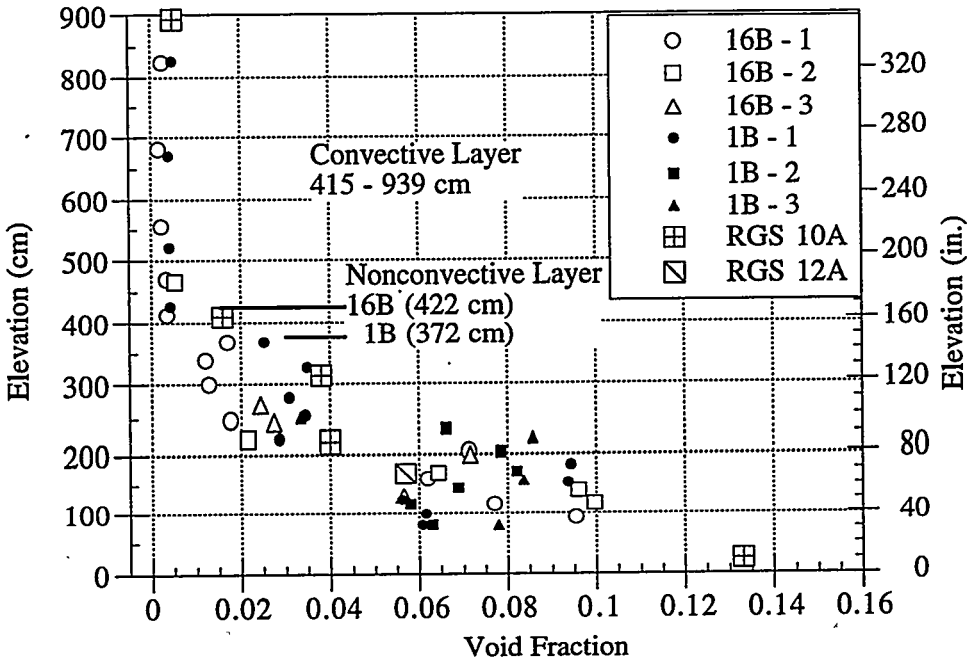

Figure 3.2.10. AN-104 Void Profile

Table 3.2.5. Retained Gas Volume in AN-104

Layer ID, Dimensions (cm)	Mean Void (%)	In-Situ Volume (m^3)	Pressure Ratio	Standard Volume (m^3)
Crust 939 - 979	11 ± 4	18 ± 8	0.99 ± 0.01	17 ± 7
Convective 415 - 939	0.4 ± 1.3	9 ± 28	1.36 ± 0.02	12 ± 37
#1 210–415	3.3 ± 1.3	28 ± 11	1.80 ± 0.03	49 ± 19
#2 0–210	9.0 ± 1.2	77 ± 10	2.03 ± 0.03	159 ± 20
Total Nonconvective	6.2 ± 0.9	105 ± 15	1.97 ± 0.03	207 ± 28
Total Tank	NA	135 ± 33	1.80 ± 0.12	236 ± 47

3.2.6 AN-105 Void Distribution and Gas Volume

Core samples and RGS void measurements were obtained in two additional risers in Tank AN-105 in June 1996, six months after VFI and ball rheometer testing. One relatively large GRE was observed in SHMS data in AN-105 one month before the RGS tests (Wilkins et al. 1996). A similar large GRE occurred four months before VFI operation.

The risers tested and the locations of important instruments are shown in Figure 3.2.11. The four risers tested cover approximately half the tank. The void profile, including both RGS and VFI values, is given in Figure 3.2.12. One problem with gas volume calculation in AN-105 is the lack of VFI data below 150 cm. The RGS supplies a measurement in this region that is consistent with the lowest VFI data. The 11% void fraction measured by the RGS at ~175 cm has a gas composition consistent with the other RGS data and is not an outlier.

Combining RGS voids with the existing VFI data set increases the nonconvective layer gas volume by about 9%, and the revised crust model lowers the crust gas volume by about 50%. The total standard volume increased by about 3%. The gas volume calculations in each sublayer are summarized in Table 3.2.6.

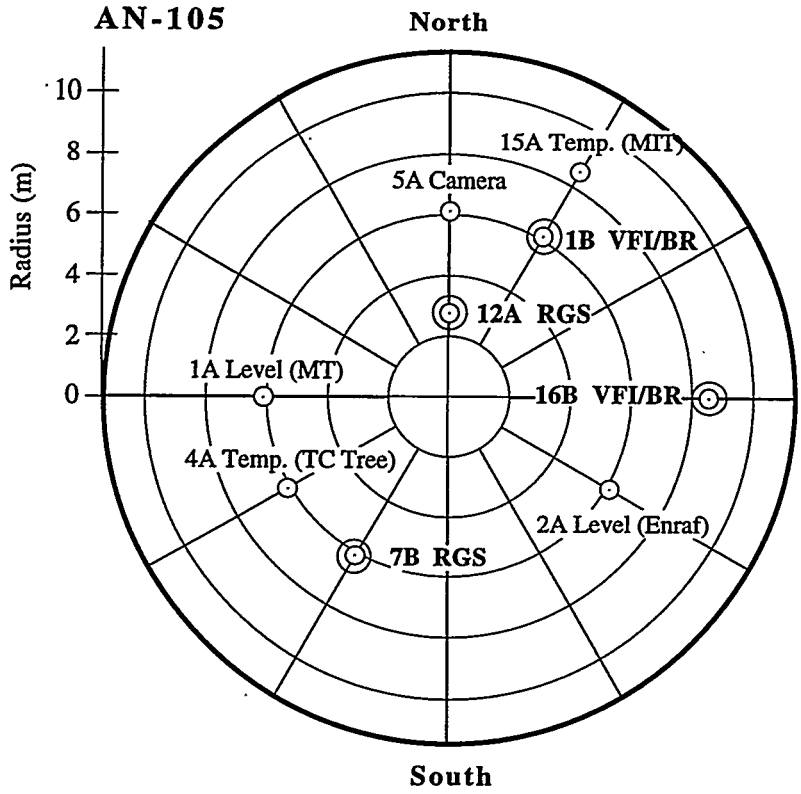

Figure 3.2.11. AN-105 Sample and Instrumentation Risers

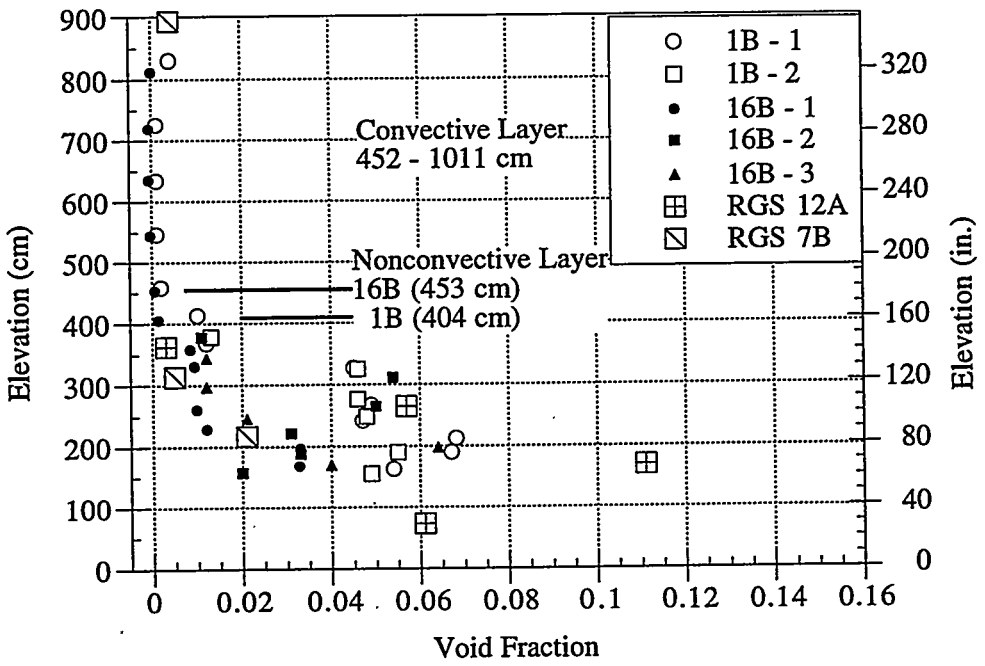

Figure 3.2.12. AN-105 Void Profile

Table 3.2.6. Retained Gas Volume in AN-105

Layer ID, Dim. (cm)	Mean Void (%)	In-situ Volume (m^3)	Pressure Ratio	Standard Volume (m^3)
Crust 1011–1041	12 ± 3	14 ± 6	0.98 ± 0.01	14 ± 6
Convective 452–1011	0.5 ± 1.0	10 ± 23	1.37 ± 0.02	14 ± 31
#1 330–452	0.7 ± 1.0	4 ± 5	1.78 ± 0.03	6 ± 9
#2 215–330	3.8 ± 0.9	18 ± 4	1.93 ± 0.03	34 ± 8
#3 0–215	6.3 ± 1.0	56 ± 9	2.13 ± 0.03	121 ± 19
Total Nonconvective	4.2 ± 0.8	77 ± 15	2.09 ± 0.04	161 ± 30
Total Tank	NA	101 ± 34	1.86 ± 0.13	189 ± 53

3.3 Surface Level Effect Models for Retained Gas Volume

In-situ measurements of local void fraction provide a relatively accurate estimate of a tank's retained gas volume. But it is not practical to operate the VFI or RGS each time the gas volume is needed. Fortunately, alternative methods have been developed for estimating stored gas volume based on two basic physical processes: 1) the response of the waste surface level to fluctuations in barometric pressure due to compression and expansion of stored gas; 2) changes in waste level

over time, in the absence of significant leaks, evaporation, additions, or changes in surface features resulting from changes in in-situ gas volume. The method relying on changes in surface level will be referred to as the SLE model, and the one depending on the response of the waste to barometric pressure fluctuations as the BPE model.

The BPE model can be used at any time without prior knowledge of the gas volume. However, it requires sensitive and frequent level measurements over some period of time to determine the in-situ gas volume accurately. It also requires an estimation of the vertical distribution of gas. Nevertheless, the BPE model remains the only nonintrusive, independent means available to assess the total stored gas volume.

The SLE model is quite robust in that it does not require exceptionally accurate or frequent level measurements or any knowledge about the vertical distribution of gas to measure the in-situ volume. However, it must reference an independent determination of the stored gas volume (e.g. VFI, RGS or gas volume at the last fill). Also, it is subject to the uncertainty of water evaporation or condensation and structural changes in the upper waste surface. Nevertheless, depending on the tank, the SLE can probably be used with confidence over a period of several years before or after an intrusive gas volume measurement.

Both the SLE and BPE models can quantify the retained gas volume in some tanks, provided the waste conditions are consistent with the assumptions of their derivation. Used with an independent in-situ gas volume measurement, the SLE and BPE models can also detect major changes in the location and volume of stored gas occurring over relatively long periods. However, neither method is suitable for interpreting small level fluctuations or quantifying episodic gas releases whose volumes are less than the models' uncertainty. The uncertainty in SLE estimates is at least that of the initial volume measurement, which is probably ± 20-25% of the in-situ volume at best. The uncertainty of the BPE model may be ± 30-50% of the in-situ volume. A typical GRE in all but SY-101 prior to mixing releases only 5–15% of the in-situ volume (see Section 4.1).

3.3.1 Barometric Pressure Effect Model

The BPE model for estimating retained gas volume is derived in detail in this section, and all the assumptions and requirements are listed. Conditions that may compromise the application of the model are developed based on these assumptions.

The volume of gas contained within a larger volume of waste can be determined by integrating the local instantaneous gas indicator function over the waste volume (Kataoka 1986; Zhang and Prosperetti 1993). The gas indicator function is defined as

$\beta(\mathbf{x}) = 1$: gas is present at position $\mathbf{x}$

$\beta(\mathbf{x}) = 0$: gas is not present.

The gas volume contained in a cylinder of uniform radius, R, between elevations L_0 and L_1 is

$$V_G = \int_{L_0}^{L_1} \int_0^{2\pi} \int_0^R \beta(r,\theta,z)\pi r dr d\theta dz \qquad (3.3.1)$$

Define the area average gas fraction, $\alpha(z)$ as

$$\alpha(z) = \frac{1}{A}\int_0^{2\pi}\int_0^{R}\beta(r,\theta,z)\pi r dr d\theta \qquad (3.3.2)$$

where $A = \pi R^2$. Substituting Eq. (3.3.2) into Eq. (3.3.1) gives

$$V_G = A\int_{L_0}^{L_1}\alpha(z)dz \qquad (3.3.3)$$

The barometric pressure response is the derivative of Eq. (3.3.3) with respect to ambient atmospheric pressure, p_0:

$$\frac{dV_G}{dp_0} = A\frac{d}{dp_0}\int_{L_0}^{L_1}\alpha(z)dz \qquad (3.3.4)$$

Recognizing that only that volume of the waste that is gas varies with pressure, and applying Leibnitz' rule for differentiation of integrals, we can write Eq. (3.3.4) as

$$\frac{dH}{dp_0} = \frac{\alpha(L_1)-\alpha(L_0)}{1-\alpha(L_0)}\frac{dL_1}{dp_0} + \frac{1}{1-\alpha(L_0)}\int_{L_0}^{L_1}\frac{d\alpha(z)}{dp_0}dz \qquad (3.3.5)$$

where $H = L_1 - L_0$.

If the stored gas is in intimate contact with the waste, the infinitesimal compression and expansion process resulting from barometric pressure fluctuations can be considered isothermal. For an isothermal process in an ideal gas, the product of the pressure and gas volume is constant. This is expressed in differential form as

$$\frac{dV_G}{dp} = -\frac{V_G}{p} \qquad (3.3.6)$$

where p is the local pressure of the gas volume, V_g. Applying the definition of the gas volume fraction yields

$$\frac{d\alpha}{dp} = -\frac{\alpha(1-\alpha)}{p} \qquad (3.3.7)$$

The derivative of local gas pressure in the waste in Eq. (3.3.7) is related to external barometric pressure via the chain rule:

$$\frac{d\alpha}{dp_0} = \frac{d\alpha}{dp}\frac{dp}{dp_0} \qquad (3.3.8)$$

Expressions for dp/dp_0 can be derived from models for waste yield stress (Whitney et al. 1996), capillary pressure, time lag between the dome space and atmosphere, changes in the gas elevation due to pressure changes, or any other effects that prevent the gas in the waste from sensing the

exact, instantaneous effect of a barometric pressure change. For the balance of this derivation, however, we assume that none of these phenomena occur and that dp/dp_0 is unity.

Substituting Eq. (3.3.7) into Eq. (3.3.4) gives an expression for the barometric pressure release:

$$\frac{dH}{dp_0} = \frac{\alpha(L_1)-\alpha(L_0)}{1-\alpha(L_0)}\frac{dL_1}{dp_0} + \frac{1}{1-\alpha(L_0)}\int_{L_0}^{L_1}\frac{\alpha(z)[1-\alpha(z)]}{p(z)}dz \qquad (3.3.9)$$

The vertical gas distribution, $\alpha(z)$, can be inferred from the waste configuration (as determined by temperature profiles or core extrusions, for example) or measured directly (i.e., with the VFI or RGS). In either case, the functional form of $\alpha(z)$ is unknown. Therefore, the average gas fraction in the layer of waste between L_0 and L_1 is applied as a uniform value independent of elevation. However, the pressure is allowed to vary linearly with elevation according to the average density and gas fraction as

$$p(z) = p + (1-\alpha)\rho g(L_1 - z - H/2) \qquad (3.3.10)$$

where p is the pressure at the layer midpoint, $\alpha = V_w/AH$ is the average gas fraction in the layer, ρ is the average ungassed density, L_1 is the elevation of the top of the layer, and H is the layer thickness, $H = L_1 - L_0$. Substituting Eq. (3.3.10) into Eq. (3.3.9), applying the stated assumptions, and performing the integration yields

$$\frac{dH}{dp_0} = -\frac{\alpha}{(1-\alpha)\rho g}\ln\left\{\frac{1+(1-\alpha)\rho gH/2p}{1-(1-\alpha)\rho gH/2p}\right\} \qquad (3.3.11)$$

Eq. (3.3.11) can be simplified by expanding the natural log as a Taylor series and retaining the first order term to give

$$\frac{dH}{dp_0} = -\frac{\alpha H}{p} \qquad (3.3.12)$$

The additional error introduced by this approximation to the natural logarithm can be estimated by $[(1-\alpha)\rho gH/p]^3/12$ (which is the next term in the Taylor series). In the extreme case, where a single layer is used to represent a deep tank with a small gas fraction, and where the midpoint pressure is equal to the pressure difference across the layer, this error is less than 10%.

If the entire waste volume is represented by N layers, the overall barometric pressure response of the waste surface, L, is the sum of Eq. (3.3.12) over all the layers.

$$\frac{dL}{dp_0} = -\sum_{i=1}^{N}\frac{\alpha_i H_i}{p_i} \qquad (3.3.13)$$

The familiar expression for calculating the total in-situ gas volume in the tank from the barometric pressure response can be derived by rearranging Eq. (3.3.13) as

$$V_G = -Ap_{EFF}\frac{dL}{dp_0} \tag{3.3.14}$$

where the effective pressure is defined by

$$\frac{1}{P_{EFF}} = \sum_{i=1}^{N}\left[\frac{f_i}{P_i}\right] \tag{3.3.15}$$

and f_i is the fraction of the total in-situ gas stored in layer i

$$f_i = \frac{A\alpha_i H_i}{V_G} \tag{3.3.16}$$

Eq. (3.3.13) provides an estimate of the barometric pressure response when the gas distribution and its pressure are known. If a suitable measurement of the barometric response and an estimate of the gas distribution are available, Eq. (3.3.14) gives the in-situ gas volume.

All gas volumes discussed up to now were at their local pressure and temperature. The true measure of the total amount of stored gas is the standard volume, which brings the in-situ volume to standard pressure and temperature. The in-situ gas volume is given by Eq. (3.3.2). Including the pressure and temperature correction yields the standard volume as

$$\hat{V}_G = \int_{L_0}^{L_1}\int_0^{2\pi}\int_0^R P(r,\theta,z)\beta(r,\theta,z)\pi r dr d\theta dz \tag{3.3.17}$$

The pressure ratio, P(r,θ,z), is defined by

$$P(r,\theta,z) = \frac{p(r,\theta,z)}{\hat{p}}\frac{\hat{T}}{T(r,\theta,z)}$$

where p(r,q,z) and T(r,q,z) are the local pressure and temperature, respectively; $\hat{p}$ is the standard atmospheric pressure of 101,320 Pa; and $\hat{T}$ is the standard temperature, 288K. Define the area average gas pressure ratio, $\overline{P\alpha}(z)$, as

$$\overline{P\alpha}(z) = \frac{1}{A}\int_0^{2\pi}\int_0^R P(r,\theta,z)\beta(r,\theta,z)\pi r dr d\theta \tag{3.3.18}$$

and an area average pressure ratio, P(z), by

$$P(z) = \frac{1}{A}\int_0^{2\pi}\int_0^R P(r,\theta,z)\pi r dr d\theta \tag{3.3.19}$$

If the pressure is uniform over area A, or if the pressure and local gas indicator are uncorrelated, the product of the average gas fraction and pressure is equal to the average of the product so that

$$\overline{P\alpha}(z) = P(z)\alpha(z) \tag{3.3.20}$$

Substituting Eq. (3.3.20) and (3.3.18) into Eq. (3.3.17) gives the standard volume between elevations L_0 and L_1 as

$$\hat{V}_G = A\int_{L_0}^{L_1} P(z)\alpha(z)dz \tag{3.3.21}$$

The total standard volume in the tank is obtained by summing over N layers represented by a uniform average gas fraction as in Eq. (3.3.10). Let the pressure ratio vary linearly within each layer according to the layer average density, gas fraction, and temperature as

$$P(z) = P + (1-\alpha)\frac{\rho g \hat{T}}{\hat{p}T}(L_i - z - H/2) \tag{3.3.22}$$

where P is the pressure ratio at the layer midpoint. Summing Eq. (3.3.21) over all layers with the above assumptions, performing the integration of Eq. (3.3.22) for P(z), and applying the definition of layer gas fraction yields this familiar expression for standard volume:

$$\hat{V}_G = V_G P_{EFF} \tag{3.3.23}$$

where the effective pressure ratio, P_{EFF}, is defined as

$$P_{EFF} = \sum_{i=1}^{N} f_i P_i$$

where P_i is the pressure ratio at the midpoint of layer i, and f_i is defined by Eq. (3.3.16). Substituting Eq. (3.3.14) for the in-situ volume yields the final result for estimating the standard volume from a measured barometric pressure response:

$$\hat{V}_G = -AP_{EFF}p_{EFF}\frac{dL}{dP_0} \tag{3.3.24}$$

The assumptions that were made in the above derivations are summarized below. Though not part of the derivation, it is essential to assume the response of the waste surface can be measured with sufficient precision and frequency. Assumptions 1–5 apply to the in-situ volume determined from Eq. (3.3.14). Additional assumption 6 applies to the standard volume computed from Eq. (3.3.24):

1. The gas-bearing waste is contained entirely in a cylinder of fixed radius and uniform but temporally variable height (true for a radially stiff tank structure whose waste and gas fraction are relatively uniform radially and azimuthally).
2. The process of expansion and compression due to barometric pressure fluctuation is isothermal (true for expected large gas surface-to-volume ratio and very slow pressure changes).
3. The gas stored in the waste behaves as an ideal gas (true for small pressure changes and relatively low temperatures with the expected gas composition and local pressures).

4. The local pressure of all the gas in the waste changes as the barometric pressure (true for relatively weak waste in which the gas elevation does not change measurably with pressure).
5. Vertical waste configuration and in-situ gas volume distribution can be estimated or is known to within an appropriate level of uncertainty (depends on information available).
6. The local pressure is radially and azimuthally uniform, or the radial and azimuthal variation of the pressure and gas fraction are uncorrelated (true if assumption 4 is met).

From these assumptions it can be inferred that, without careful consideration, the BPE model should *not* be applied to tanks

- in which a high lithostatic load results from an interstitial liquid level well below the waste surface where the gas is stored as pore-filling bubbles (potentially violates assumptions 1 and 4)
- with a very low waste level (potentially violates assumptions 1 and 4)
- that have been salt-well pumped (potentially violates assumptions 1, 4, and 5)
- with a forest of suspended hardware such as airlift circulators, cooling coils, etc. (potentially violates assumptions 1 and 4)
- in which the waste is periodically disturbed by mixing, specifically SY-101 (violates assumption 4)
- in which the gas elevation changes during the time of the barometric pressure response measurement (violates assumption 5)
- in which an appropriately precise waste level instrument is not available, or readings are not taken with sufficient frequency.

The best prospects for an accurate volume determination with the BPE model are tanks with relatively deep, wet waste, where the vertical gas distribution can be estimated with fair confidence. Currently, this includes the DSTs and few of the SSTs. More confidence will be gained in applying the model to SSTs as more are assayed with the RGS.

Nevertheless, it is almost impossible to attribute a correlation of waste level and barometric pressure to anything but the presence of stored gas. Therefore, while a negligible barometric pressure response does not necessarily indicate the absence of gas, a strong measured barometric pressure response should *always* be taken as an indication of stored gas, regardless of how well a tank satisfies all the above requirements.

The BPE model has a significant inherent uncertainty in the best of conditions. The smaller the retained gas volume, the less accurately the BPE model can estimate it. We can derive the minimum detectable volume for a given uncertainty threshold and measurement error. The barometric response in Eq. (3.3.14) can be rewritten in finite difference form as

$$V_G = -Ap_{EFF}\frac{\Delta L}{\Delta p_0} \tag{3.3.25}$$

where ΔL is the specific level change in response to a corresponding barometric pressure change of Δp_0.[(a)] Assuming the uncertainties in the barometric pressure change and tank area are small, the relative uncertainty in the volume in Eq. (3.3.25) can be estimated by linear error propagation as

(a) The pressure fluctuation should be only the amount that exceeds twice the yield stress of the material according to Whitney et al. (1996). However, the yield stress in the DSTs is small, ~150 Pa, compared with barometric pressure changes.

$$\left(\frac{\sigma_V}{V_G}\right)^2 = \left(\frac{\sigma_p}{p_{EFF}}\right)^2 + \left(\frac{\Delta L_{min}}{\Delta L}\right)^2 \qquad (3.3.26)$$

Here, the relative uncertainty in level response has been approximated by the instrument precision, ΔL_{min}, divided by the actual level change, ΔL. Solving Eq. (3.3.25) for ΔL, substituting the result into Eq. (3.3.26), and solving for V_G yields

$$V_{MIN} = A p_{EFF} \frac{\Delta L_{min}}{\Delta p_0 \left[\left(\frac{\sigma_V}{V_G}\right)^2 - \left(\frac{\sigma_p}{p_{EFF}}\right)^2\right]^{1/2}} \qquad (3.3.27)$$

where V_{MIN} is the minimum in-situ gas volume that is measurable with the given uncertainties in volume and pressure and the given instrument precision.

Figure 3.3.1 shows the gas volume and void fraction as a function of barometric pressure change for a typical DST. This tank is assumed to have a 10-m waste level and a 4-m nonconvective layer yielding an effective pressure of 1.8 ± 0.4 atm. An Enraf level gauge with a precision of ± 0.1 cm is used to measure level changes. The effective detection threshold might be defined as 100% error. The nominal barometric pressure change is about 1 kPa, with a maximum of 3 kPa in the late fall and winter and a minimum of 0.3 kPa in the summer (Whitney 1995).

Under these assumptions, it is clear from the figure that the BPE method (assuming all assumptions and conditions prescribed earlier are met) can calculate the in-situ gas volume to within ± 25% only if the gas volume is ~300 m^3 or more and if the pressure change is above about 2 kPa. For nominal conditions, an in-situ volume of volume of 200 m could be measured with an uncertainty under ± 50%. This is consistent with the uncertainties presented in the comparisons of BPE and VFI/RGS volume estimates to follow.

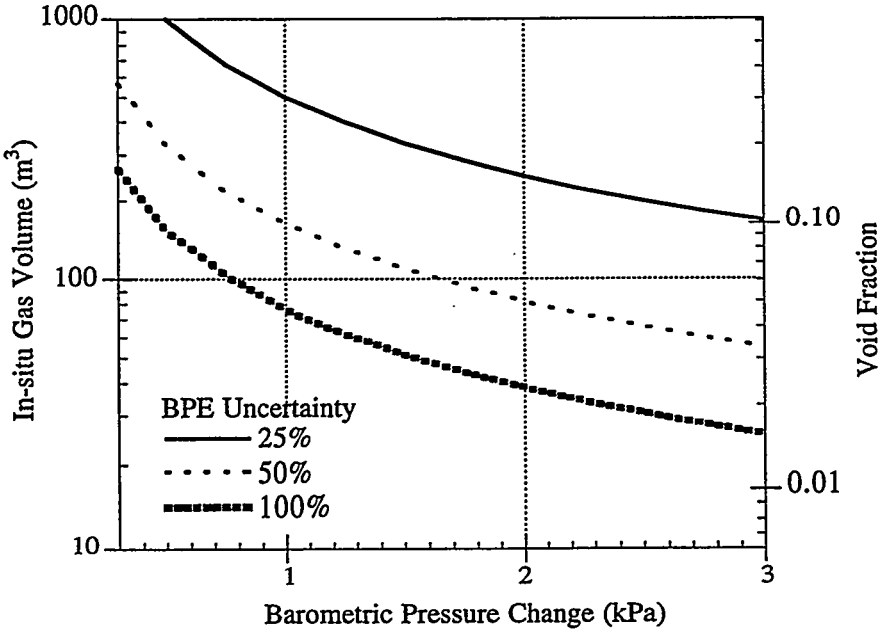

Figure 3.3.1. BPE Uncertainty for a Typical DST

Figure 3.3.2 shows the detection threshold (defined as 100% error) for other measurement instruments as well as the Enraf for the same typical DST. The FIC probe has an assumed precision of 0.2 cm and the manual tape 0.4 cm. The actual uncertainty varies considerably from tank to tank (Whitney 1995). The manual tape requires a such a large pressure change and gas volume as to be essentially unusable. The precision afforded by the Enraf gauge is clearly required for reasonably accurate BPE volume calculations.

Another complicating factor of the BPE model is that it senses only noncondensible gases. The volume of water vapor (or other soluble gas at saturation) in trapped bubbles does not respond to barometric pressure changes because its partial pressure is a function only of the local temperature on the time scale of a barometric pressure swing. Water vapor evaporates or condenses as necessary to maintain a constant partial pressure during barometric pressure changes.

For a total pressure of 2 atm, the water vapor volume fraction of the bubbles is less than 10% below waste temperatures of about 140°F. This is shown in Figure 3.3.3. Above this temperature, water vapor is an important contributor to waste buoyancy and barometric pressure response and must be accounted for. However, since water vapor acts as a diluent, it does not influence flammability calculations.

With the exception of SY-101,[a] the BPE model should provide good estimates of stored gas volume in the DSTs on the FGWL. Surface level readings from highly sensitive Enraf buoyancy gauges have now been recorded for a sufficient time to obtain very good barometric pressure measurements. At the same time, VFI operation has provided a detailed measurement of the gas distribution as well as an independent calculation of the in-situ gas volume. Therefore, the BPE estimates of in-situ gas volume in these tanks should be the most accurate possible.

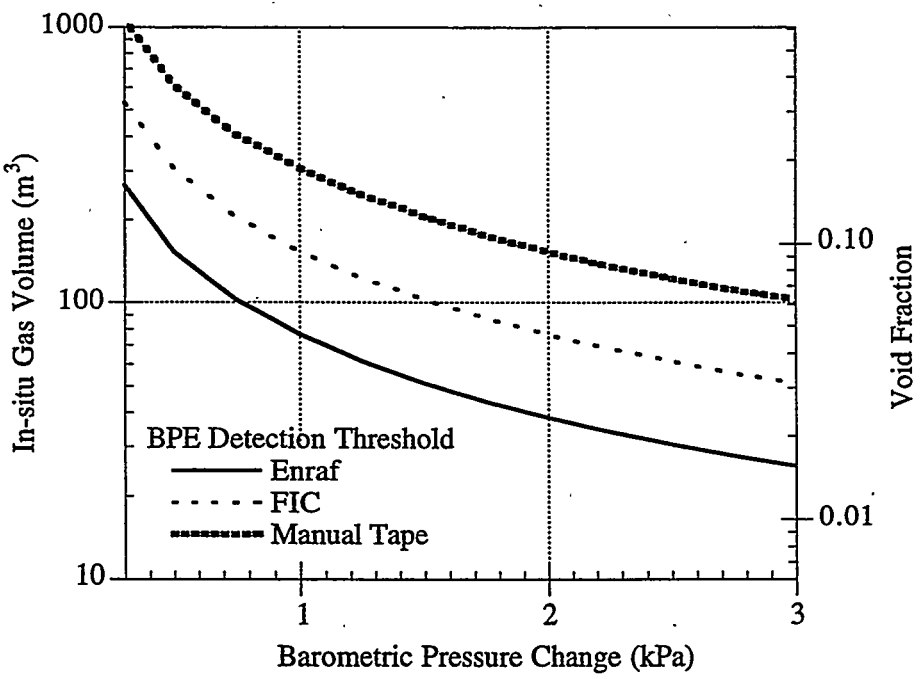

Figure 3.3.2. Threshold BPE Gas Volume for Several Level Instruments

(a) The periodic vertical motion of small bubbles induced by the mixer pump and the subsequent settling greatly amplifies the apparent compressibility and makes an accurate dL/dP measurement extremely difficult (see Brewster et al. 1995).

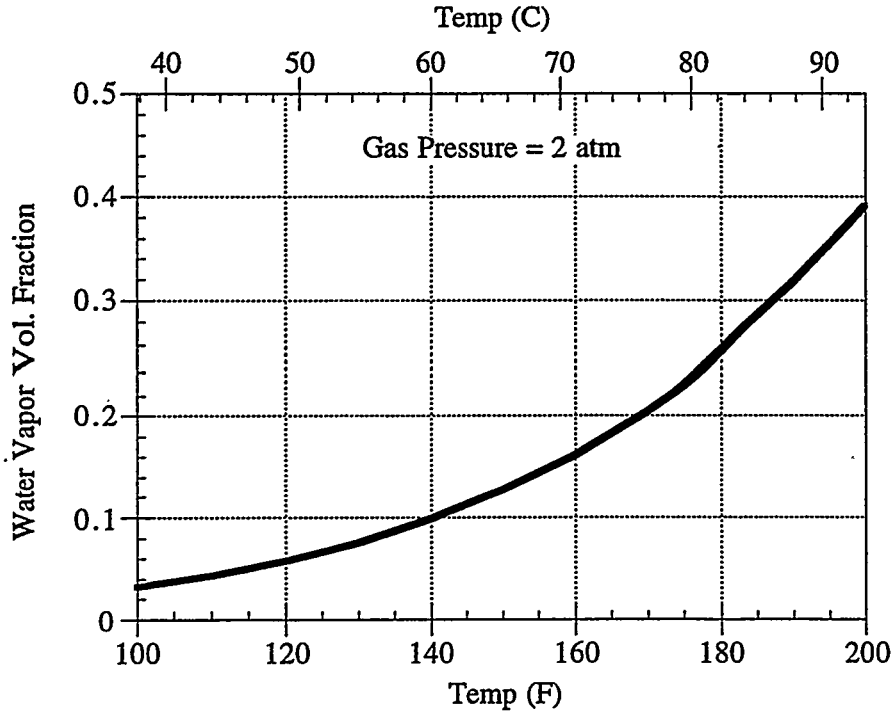

Figure 3.3.3. Bubble Water Vapor Fraction Versus Waste Temperature

In Table 3.3.1, the BPE volume estimates are compared with those calculated from the VFI results. The BPE estimates use the measured barometric pressure response with the effective pressure and pressure ratio calculated from the gas distribution derived in the VFI and RGS data using Eq. (3.3.13). The table conveys the same information as Stewart et al. (1996a) but uses a better measured barometric pressure response, applies the improved gas volume models described in Section 3.1.1, and includes a comparison of the standard volume.[a] No reliable barometric pressure response could be obtained from SY-101 because of the regular disturbance of mixer pump operation, so it is not shown in the table.

The difference between the BPE and VFI/RGS estimates of in-situ and standard volumes is within the uncertainty of the VFI/RGS volumes. But in AN-104, the BPE model predicts a higher gas volume than that obtained from the VFI. The uncertainty for the BPE result is significantly larger than for the VFI calculation in AN-103 and SY-103, but they are of the same order in AN-104, AN-105, and AW-101. As mentioned in Section 3.1, episodic gas releases are insignificant with respect to stored gas volume estimates in these tanks since the release volumes are less than the uncertainty of the inventory.

We conclude that gas volumes can be estimated relatively accurately with the BPE model when the gas distribution is known precisely. However, such precise data are seldom available, which raises the question of how sensitive the BPE model is to the gas distribution. To evaluate this, two approximate models were tested: a two-layer model assuming the gas is stored in the crust and nonconvective layers and a one-layer model assuming the gas is distributed uniformly over the entire tank.

(a) These barometric pressure response values were calculated by PD Whitney, PNNL, January 3, 1997, from Enraf data recorded over all of 1996. The barometric pressure response for SY-103 includes 1995 data as well.

Table 3.3.1. Measured and BPE Gas Volume Estimates in DSTs

	AN-103	AN-104	AN-105	AW-101	SY-103
Values derived from VFI/RGS data (see Table 3.1.2)					
In-situ volume (m^3)	229 ± 41	132 ± 33	101 ± 34	89 ± 30	99 ± 56
Standard volume (m^3)	380 ± 54	240 ± 47	190 ± 53	140 ± 43	160 ± 78
dL/dP P_{EFF} (atm)	1.7 ± 0.5	1.8 ± 0.7	1.8 ± 0.9	1.5 ± 0.7	1.7 ± 1.2
Volumes derived from BPE model with measured dL/dP					
Measured dL/dP from Enraf data (cm/kPa)	-0.39 ± 0.11	-0.15 ± 0.05	-0.15 ± 0.05	-0.16 ± 0.05	-0.14 ± 0.11
In-situ volume (m^3)	265 ± 76	115 ± 38	111 ± 38	100 ± 31	100 ± 77
VFI/RGS - BPE (m^3)	-36	17	-10	-11	-1
Standard volume (m^3)	440 ± 130	210 ± 69	210 ± 72	160 ± 51	163 ± 130
VFI/RGS - BPE (m^3)	-60	30	-20	-20	-3

The two-layer model is tailored specifically to DSTs. It assumes knowledge of nonconvective layer height, overall waste level, and temperature profile and makes use of the independent gas volume estimate for the crust. The crust gas is assumed to be at 1 atm, and the gas in the nonconvective layer is assigned the pressure of the midpoint of that layer. Expanding Eq. (3.3.14) for the two layers gives

$$V_G = -\left[A p_{NC} \frac{dL}{dp_0} + \left(\frac{p_{NC}}{p_{CR}} - 1\right) V_{CR} \right] \tag{3.3.28}$$

where p_{NC} is the pressure evaluated at the midpoint of the nonconvective layer; p_{CR} is the average pressure of gas stored in the crust; and V_{CR} is the independent crust volume estimate from Eq. (3.1.19) and listed in Table 3.1.2. The standard volume is computed as

$$\hat{V}_G = P_{NC} V_G - (P_{NC} - P_{CR}) V_{CR} \tag{3.3.29}$$

where P_{NC} is the pressure ratio (including temperature effects) of the nonconvective layer, and P_{CR} is the pressure ratio of the crust layer.

The one-layer model assumes only that the overall waste height and temperature profile are known. No knowledge of waste properties, configuration, or gas distribution is required. The gas is assumed to be distributed uniformly and stored at the midpoint of the entire waste column. The waste density is assumed to be 1600 kg/m^3, which is appropriate for the average waste in the DSTs being considered. The uncertainty of the pressure is assumed to be half of the waste midpoint gauge pressure, which implies that the gas is stored somewhere between the waste surface and the tank bottom at a 95% confidence level. The in-situ and standard volumes for the one-layer model are given by the following expressions:

$$V_G = -A\bar{p}\frac{dL}{dp_0} \tag{3.3.30}$$

$$\hat{V}_G = \bar{P} V_G \tag{3.3.31}$$

where the average pressure is defined as the hydrostatic pressure at the midpoint of the waste column, assuming a density of 1600 kg/m^3, and the average pressure ratio includes the correction for the average waste temperature.

Table 3.3.2 summarizes the results of these two models as well as the "best estimate" BPE results and those calculated directly from VFI/RGS measurements from Table 3.2. It is remarkable that, except for AW-101, even the simplest possible one-layer model predicts the in-situ gas volume within one standard deviation of the VFI/RGS value and, except in AN-103, the two-layer model also predicts the standard volume within one standard deviation of the VFI/RGS standard volume. In all cases, the VFI/RGS estimate lies within one standard deviation computed for the BPE models. The uncertainty is higher in the two-layer model because it compounds the high uncertainty in the crust volume with that of the barometric pressure correlation.

It is clear that the BPE model provides estimates of the in-situ volume accurate to within 30% and standard volumes to within about 40% in DSTs (or tanks with a configuration typical of DSTs). A precise prior knowledge of the gas distribution is not necessary to apply the method. Changes in gas volume or position due to GREs are negligible compared with the uncertainty.

Table 3.3.2. Evaluation of Approximate BPE Models

	AN-103	AN-104	AN-105	AW-101	SY-103
In-Situ Volume (m^3)					
VFI/RGS (Table 3.1.2)	229 ± 41	132 ± 33	101 ± 34	89 ± 30	99 ± 56
BPE model (Table 3.3.2)	265 ± 76	115 ± 38	111 ± 38	100 ± 31	100 ± 77
Two-layer model	273 ± 98	114 ± 45	115 ± 45	106 ± 51	100 ± 81
One-layer model	270 ± 95	111 ± 44	110 ± 45	121 ± 46	91 ± 72
Standard Volume (m^3)					
VFI/RGS (Table 3.1.2)	380 ± 54	236 ± 47	189 ± 53	141 ± 43	160 ± 78
BPE model (Table 3.3.2)	440 ± 130	210 ± 69	210 ± 72	160 ± 51	163 ± 130
Two-layer model	472 ± 190	202 ± 86	216 ± 90	181 ± 110	160 ± 133
One-layer model	420 ± 150	180 ± 70	184 ± 75	202 ± 80	132 ± 104

3.3.2 Surface Level Effect Model

The SLE model is based on the premise that the rate of change in waste surface level is a result of gas accumulation in addition to liquid evaporation, waste addition, or leakage; changes in liquid or solid density; or large structural changes in the waste surface (e.g., subsidence). This is expressed by

$$\frac{dL}{dt} = \frac{1}{A}\frac{dV_G}{dt} + \sum_i \frac{\partial L}{\partial x_i}\frac{dx_i}{dt} \qquad (3.3.32)$$

where x_i represents factors other than stored gas volume that affect the waste level. The partial derivatives on the right side of Eq. (3.1.32) can be evaluated from mathematical models if they are available. Integrating Eq. (3.1.32) over a period of time, Δt, which can be positive or negative, and solving for the gas volume change yields

$$V_G(t+\Delta t) = V_G(t) + A[L(t+\Delta t) - L(t) - A\sum_i \left[\int_t^{t+\Delta t} \frac{\partial L}{\partial x_i} \frac{dx_i}{dt} dt \right] \quad (3.3.33)$$

where $V_G(t)$ is the total in-situ gas volume at time t. The in-situ gas volume and waste level that comprise this required starting point can be determined relatively accurately from the local gas volume fractions measured with the VFI/RGS. The last tank fill can also be a suitable starting point if the level and the gas volume are known at that time.

The major sources of uncertainty in the gas volume can be estimated by rearranging Eq. (3.1.33) to represent the change in gas volume over a given time period, Δt, to yield

$$\Delta V_G = A[\Delta L_W - \Delta L_E - \Delta L_A] \quad (3.3.34)$$

where ΔV_G is the change in in-situ gas volume, A is the tank cross-sectional area, ΔL_W is the measured surface level change, ΔL_E is the equivalent level rise due to evaporation, and ΔL_A is the level rise due to net waste addition, removal, or other similar effects. The relative uncertainty in the gas retention can be expressed by linear combination of uncertainties in Eq. (3.1.34) as

$$\left(\frac{\sigma_V}{\Delta V_G}\right)^2 = A\left[\frac{\Delta L_W}{\Delta V_G}\left(\frac{\sigma_L}{\Delta L_W}\right)\right]^2 + A\left[\frac{\Delta L_E}{\Delta V_G}\left(\frac{\sigma_E}{\Delta L_E}\right)\right]^2 + A\left[\frac{\Delta L_A}{\Delta V_G}\left(\frac{\sigma_A}{\Delta L_A}\right)\right]^2 \quad (3.3.35)$$

where σ_i represents the standard error in each quantity.

The SLE model does not require a high-accuracy level measurement. Waste level change in DSTs is now typically measured by an Enraf buoyancy gauge to within a precision (σ_L) of $\pm$ 0.1 cm or better. This small error represents less than half a cubic meter of in-situ gas retention. Even the relatively low precision of a manual tape measurement that is on the order of $\pm$ 1 cm represents an error of less than 5 m^3 of gas. Therefore, if any significant volume of gas is being retained, the first term of Eq. (3.1.35) quickly becomes small as gas accumulates.

Large waste transfers may invalidate subsequent SLE model predictions. Waste transfers occur over a relatively short time. The resulting net level change, ΔL_A, then remains fixed, and the last term in the right side of Eq. (3.1.35) decreases with time as the retained gas volume grows. But the magnitude of the uncertainty ($\sigma_A/\Delta L_A$) may be large if a large amount of waste is transferred, or if the remaining waste is disturbed. A large waste addition increases the hydrostatic pressure and reduces the volume of the existing stored gas by a predictable amount. The incoming waste is assumed to have no gas, which may not be exactly true. A large waste removal produces a reverse change in hydrostatic pressure but is also likely to cause a significant gas release that is difficult to measure accurately. We conclude that the SLE model can probably be applied across moderate waste additions but only for small volumes of waste removal. However, complete waste removal can serve as a new starting point if the gas content of the following addition is known.

In the absence of waste transfers, the major source of uncertainty in Eq. (3.1.35) can be the effect of evaporation. Long-term (1994–1997) evaporation effects have only been measured in SY-101.[a] The head-space water vapor mass balance indicates that this tank is very slowly

(a) Net water gain or loss is reported in informal quarterly reviews of SY-101 mixer pump data prepared by PNNL.

accumulating water. There is net water loss only occasionally during the winter when the ambient air is driest. The high salt concentration (especially sodium hydroxide) reduces the water vapor pressure and therefore inhibits evaporation. One could expect the error to be similarly negligible in other DSTs with a crust layer; however, evaporation could be significant in tanks that do not have a crust layer and that contain dilute waste at a relatively high temperature.

The evaporation rate is difficult to estimate unless the ventilation rate and the head-space humidity are well established. If both quantities are measured to within ± 20%, the relative uncertainty in evaporation ($\sigma_E/\Delta L_E$) could be as low as 30%. The uncertainty is much higher if evaporation is estimated indirectly (e.g., waste heat load, mass transfer correlations, numerical simulation, etc.).

If the level change due to evaporation can be shown to be small relative to gas retention ($A\Delta L_E/\Delta V_G \ll 1$), the overall uncertainty contribution will also be small, regardless of the uncertainty in evaporation. Also, since both evaporation loss and retained gas volume increase linearly over time, the relative uncertainty does not accumulate with time. On the other hand, if little gas is being retained compared with evaporation ($A\Delta L_E/\Delta V_G > 1$), the overall uncertainty may be large enough to disqualify it even with a relatively accurate evaporation estimate.

We conclude that the SLE model provides a reasonable estimate of long-term retained gas accumulation when gas retention is the dominant influence on waste level change. This is demonstrably the case in the six DSTs on the FGWL. Evidence of this condition would be a steady rise in waste level over several years, periods of steady level rise interrupted by sudden drops due to episodic gas releases, or seasonal level variation with a maximum in September and October and a minimum in March and April.[a] A constant or declining waste level would indicate constant or declining gas volume only if evaporation and other effects can be specifically shown to be negligible.

3.4 Visual Study of Core Extrusions and Waste Surface

Core sample extrusion photographs were shown in Stewart et al. (1996a) for SY-103, AW-101, AN-103, and AN-105, but only those from SY-103, AW-101, and AN-105 were from the most recent sampling. In this section, photographs from the most recent cores from AN-103 and AN-104 are added (Figures 3.4.1 to 3.4.7). Waste surface photos for all six tanks are also given to complete the picture (see Figures 3.4.8 through 3.4.14), including one of GRE Event I (June 26, 1993) in progress in SY-101 (Figure 3.4.13).

3.4.1 Core Extrusion Photographs

Extrusion photographs of AN-103 core samples from 1986 and 1996 are shown in Figures 3.4.1 and 3.4.2. The 1986 core was taken only a few months after the last fill, in February 1986, before most of the gas accumulation had occurred. Bubbles are clearly visible in all segments of the 1996 cores but only in segment 12 of the 1986 core. Segment 15 (1996 core) is in the location of the maximum void of 12–15%. The 1996 core appears dryer and stiffer than the 1986 core. 1996 segments 16 and 17 are especially dry compared with 1986 segments at the same level (15 and 16). The ball rheometer stopped at elevations represented by segment 16. In Figure 3.4.2, note the similarity of the crusts in segments 1 and 13 at the top of the nonconvective layer.

(a) This indicates a significant gas volume that changes cyclically in response to the average waste temperature. Thermal inertia creates the time lag between the waste and ambient temperature seasonal maxima.

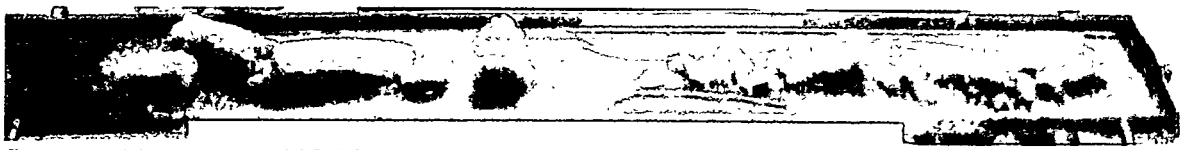

Segment 11, elevation 338-386 cm (133-152 inches)

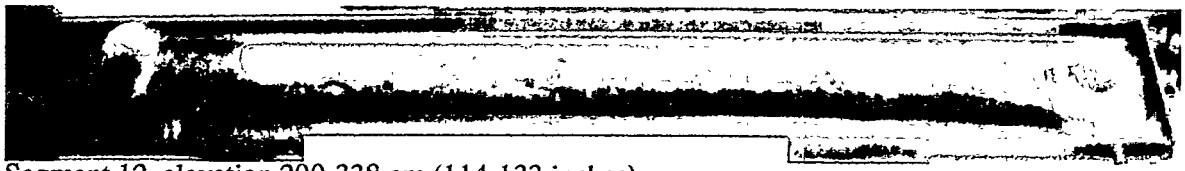

Segment 12, elevation 290-338 cm (114-133 inches)

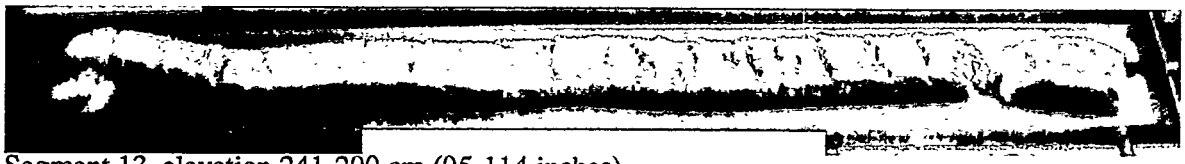

Segment 13, elevation 241-290 cm (95-114 inches)

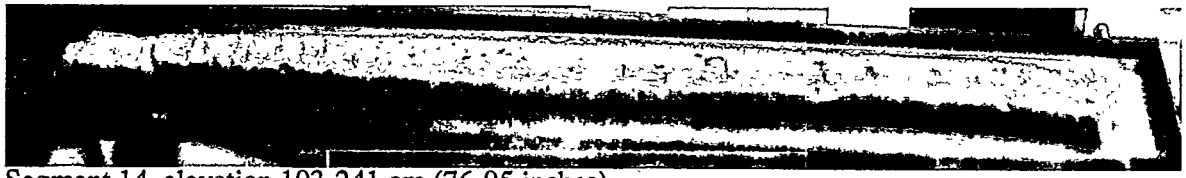

Segment 14, elevation 193-241 cm (76-95 inches)

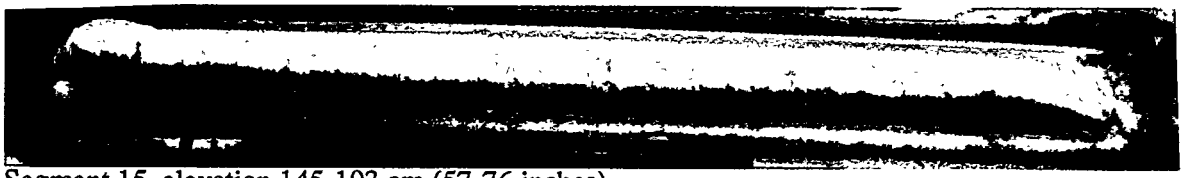

Segment 15, elevation 145-193 cm (57-76 inches)

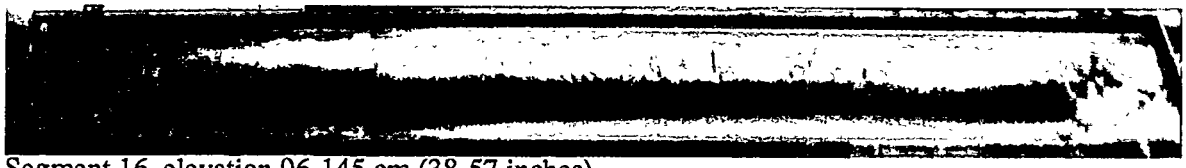

Segment 16, elevation 96-145 cm (38-57 inches)

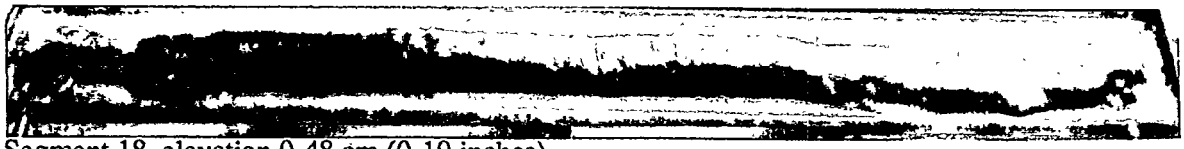

Segment 18, elevation 0-48 cm (0-19 inches)

Figure 3.4.1. AN-103 Core Extrusions, 1986

Segment 1, elevation 868-916 cm (342-361 inches) [Partial segment, waste surface at 884 cm].

Segment 13, elevation 290-338 cm (114-133 inches)

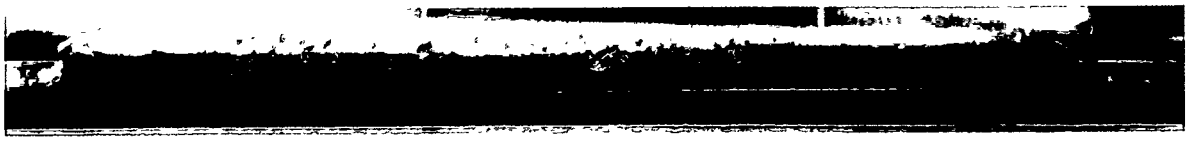

Segment 15, elevation 193-241 cm (76-95 inches)

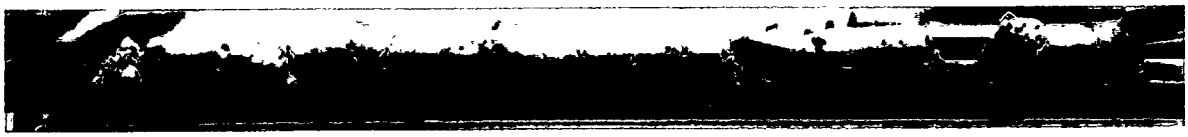

Segment 16, elevation 145-193 cm (57-76 inches)

Segment 17, elevation 96-175 cm (38-52 inches)

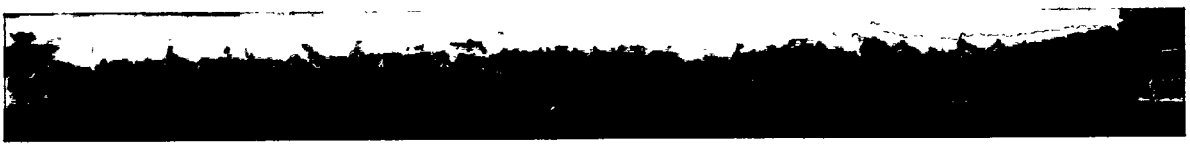

Segment 18, elevation 48-96 cm (19-38 inches)

Figure 3.4.2. AN-103 Core 166 Extrusions, 1996

Figure 3.4.3 shows extrusion photographs of the 1996 core 164 sample from AN-104. Bubbles are visible in all segments. The waste appears generally more fluid than that in AN-103, especially in segments 14, 15, and 19.

AN-105 extrusion photos from the 1996 core 152 sample are shown in Figure 3.4.4. Fewer bubbles are apparent than in either AN-103 or AN-104. Segment 18 had the highest void fraction, 8–13%. AN-105 waste is also more liquid than the other two tanks. Only segment 18 appears able to hold its shape on the extrusion tray.

The extrusion photos from the 1996 core 132 sample from AW-101 are shown in Figure 3.4.5. Bubbles are not obvious except in segment 1. The nonconvective layer appears quite uniform in texture, midway in moisture between AN-103 and AN-105. Again, note the similarity of the two crust segments (1 and 2) and the top of the nonconvective layer in segment 18.

Figures 3.4.6 and 3.4.7 are extrusion photographs of SY-103 cores from 1986 and 1994, respectively. The images in Figure 3.4.7 were obtained from video tapes taken through the 222S hot cell window. The 1986 core was taken prior to the last fill that caused SY-103 to begin episodic gas releases. The lower portion of the 1986 core appears extremely dry and stiff. The 1994 core also appears relatively firm and uniform, similar to the upper segments of AN-103 (see Figure 3.4.2). The ball rheometer was supported in the region represented by segment 13. Few bubbles are clearly identifiable in either core. Note the similarity of the partial crust sample of segment 2 with the nonconvective layer waste of segment 7 in Figure 3.4.6.

The extrusions generally show that the tanks with the larger, more frequent GREs have wetter, weaker waste. Those storing the most gas have generally dryer, stiffer waste with more bubbles visible in the cores. Where samples are available, the material composing the crust layer appears very similar to the waste in the upper part of the nonconvective layer.

3.4.2 Waste Surface Appearance

The waste surface of AN-103 is shown in Figure 3.4.8. Except for SY-101, AN-103 has the thickest crust layer of the six DSTs. The view is toward the newly installed MIT, which has a diameter of about three inches (see Figure 3.2.7). A sludge weight cable is visible to the left of the MIT. The cable is hanging vertically, indicating the crust has been stationary.

The crust in AN-104 is relatively thin and is not completely continuous. The waste surface is shown in Figure 3.4.9, with about the same view toward the MIT as AN-103, above. Instead of hanging vertically as in AN-103, the sludge weight is pulled clockwise (camera is closer to the tank center—see Figure 3.2.9). We attribute this to the tendency of Earth's rotation to pull the sludge weight's attachment to the tank dome counter-clockwise against the crust, which is rotating at a slightly slower speed. This is consistent with the deflection of a second sludge weight near the camera, just visible in the lower right corner of Figure 3.4.9. The crust in AN-103 is apparently more tightly attached to the tank wall, so it rotates with the Earth. Others have attributed these deflections to crust motion caused by prior gas releases.

The waste surface in AN-105 is shown in Figure 3.4.10. The view is apparently toward the thermocouple tree in riser 4A (see Figure 3.2.11). The crust in this tank is thinner than that in AN-104, but the surface appears similar to AN-104, with no large vertical features.

The AW-101 crust surface is shown in Figure 3.4.11. This tank is estimated to have the third thickest crust of the six. Note the large vertical features in the foreground. The pattern of deposits on the tank wall in the background also indicate a highly irregular surface.

Segment 14, elevation 338-386 cm (133-152 inches)

Segment 15, elevation 290-338 cm (114-133 inches)

Segment 16, elevation 242-290 cm (95-114 inches)

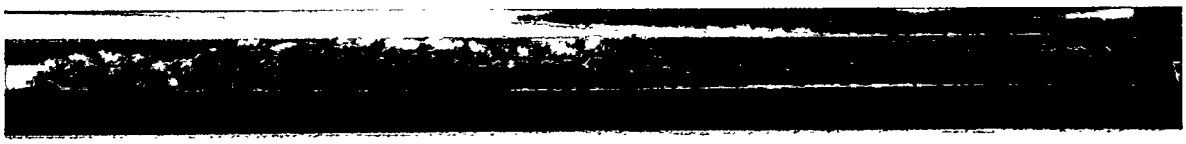

Segment 17, elevation 193-242 cm (76-95 inches)

Segment 19, elevation 96-145 cm (38-57 inches)

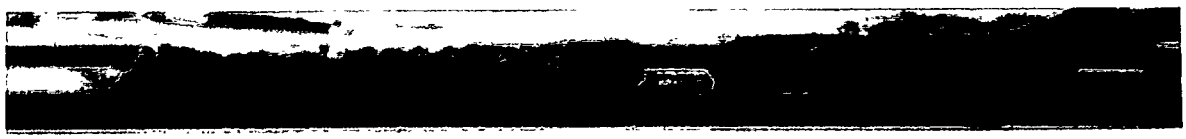

Segment 20, elevation 48-96 cm (19-38 inches)

Figure 3.4.3. AN-104 Core 164 Extrusions, 1996

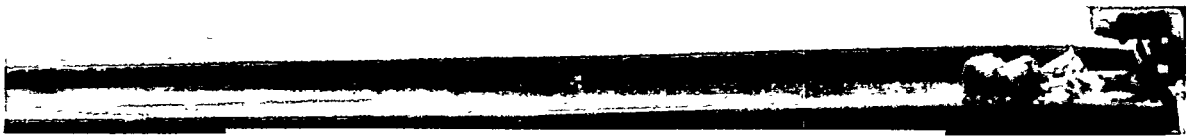

Segment 1, elevation 1013-1041 cm (399-410 inches)

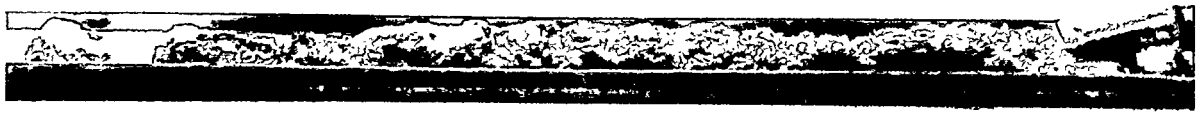

Segment 16, elevation 290-338 cm (114-133 inches)

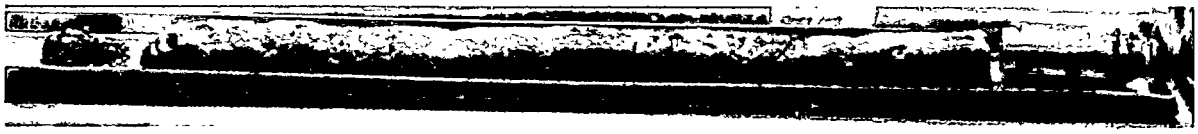

Segment 18, elevation 193-241 cm (76-95 inches)

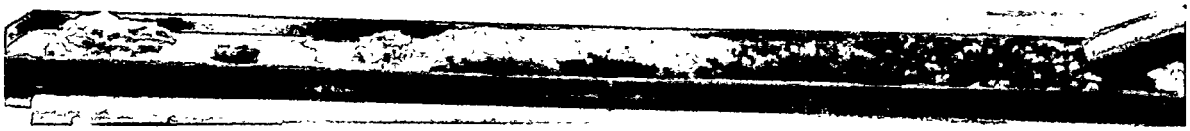

Segment 20, elevation 96-145 cm (38-57 inches)

Segment 22, elevation 0-48 cm (0-19 inches)

Figure 3.4.4. AN-105 Core 152 Extrusions, 1996

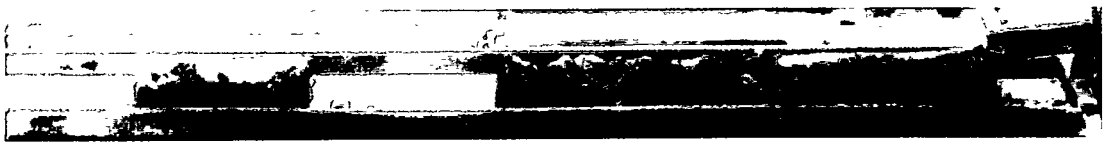

Segment 1, elevation 1013-1040 cm (399-409 inches)

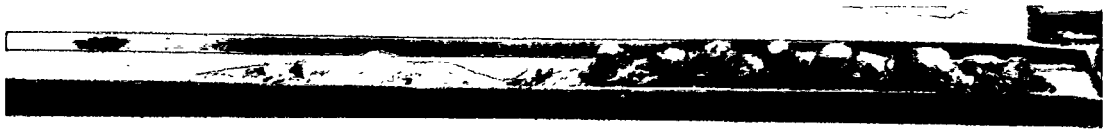

Segment 2, elevation 965-1013 cm (380-399 inches)

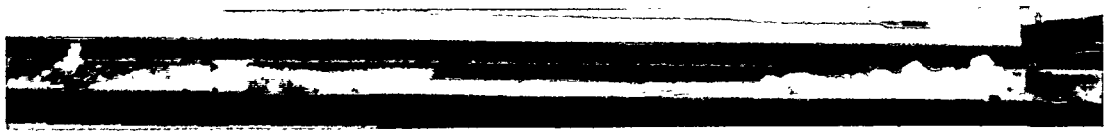

Segment 16, elevation 290-338 cm (114-133 inches)

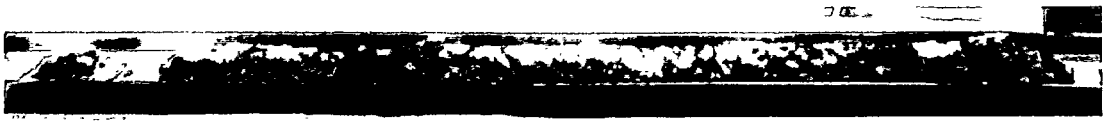

Segment 18, elevation 193-241 cm (76-95 inches)

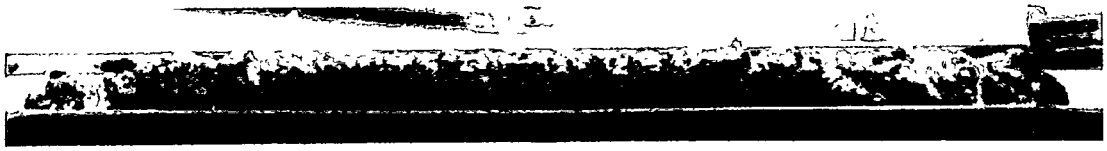

Segment 20, elevation 96-145 cm (38-57 inches)

Segment 22, elevation 0-48 cm (0-19 inches)

Figure 3.4.5. AW-101 Core 132 Extrusions, 1996

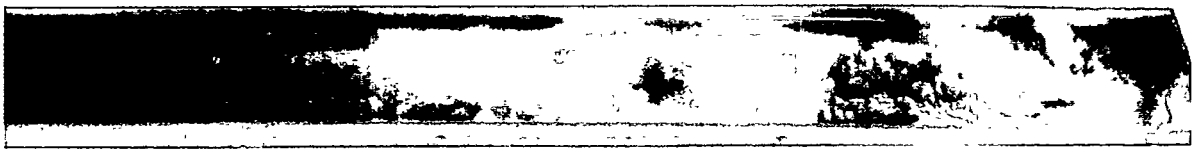

Segment 2, elevation 531-579 cm (209-228 inches)

Segment 7, elevation 290-338 cm (114-133 inches)

Segment 10, elevation 145-193 cm (57-76 inches)

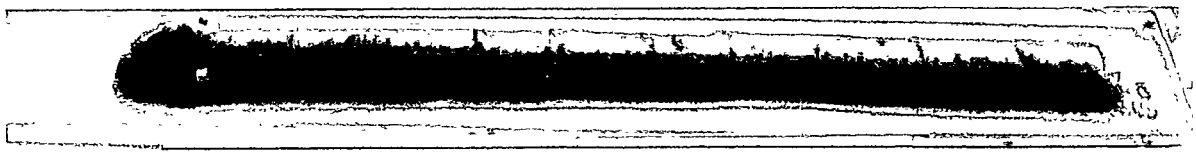

Segment 12, elevation 48-96 cm (19-38 inches)

Figure 3.4.6. SY-103 Core 1 Extrusions, 1986

Segment 4, elevation 531-579 cm (209-228 inches)

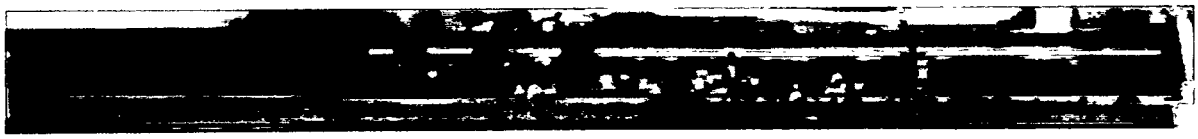

Segment 10, elevation 241-289 cm (95-114 inches)

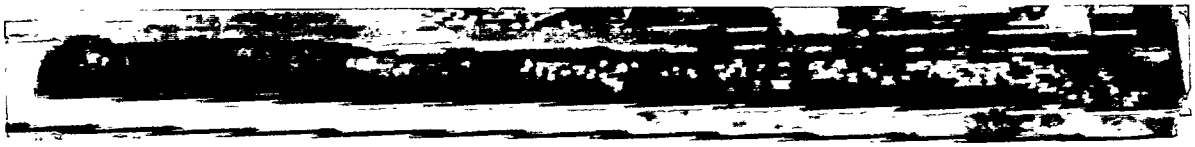

Segment 11, elevation 193-241 cm (76-95 inches)

Segment 12, elevation 145-193 cm (57-76 inches)

Segment 13, elevation 96-145 cm (38-57 inches)

Segment 14, elevation 48-96 cm (19-38 inches)

Figure 3.4.7. SY-103 Core 62 Extrusions, 1994

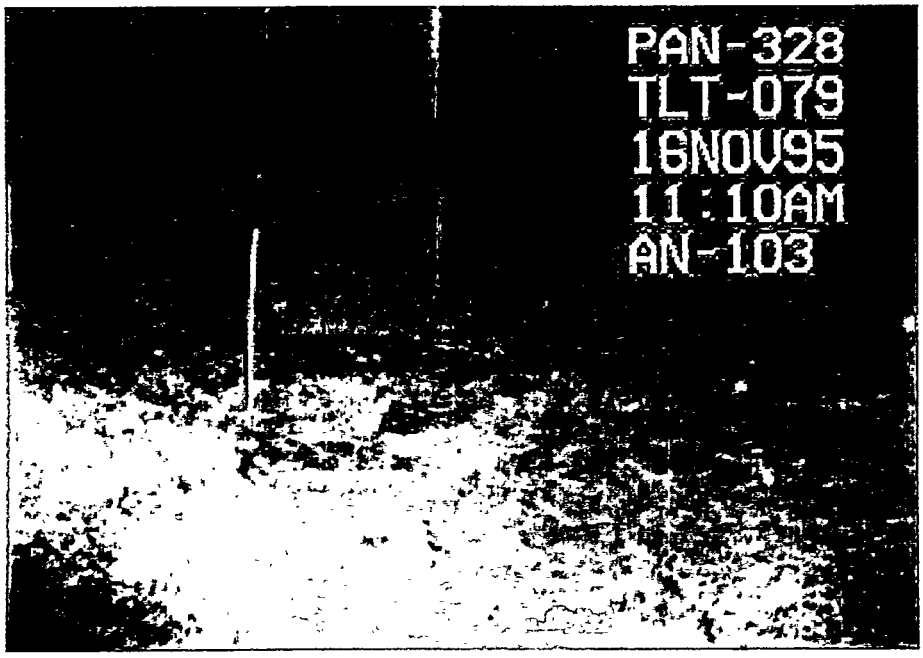

Figure 3.4.8. AN-103 Waste Surface, 1995

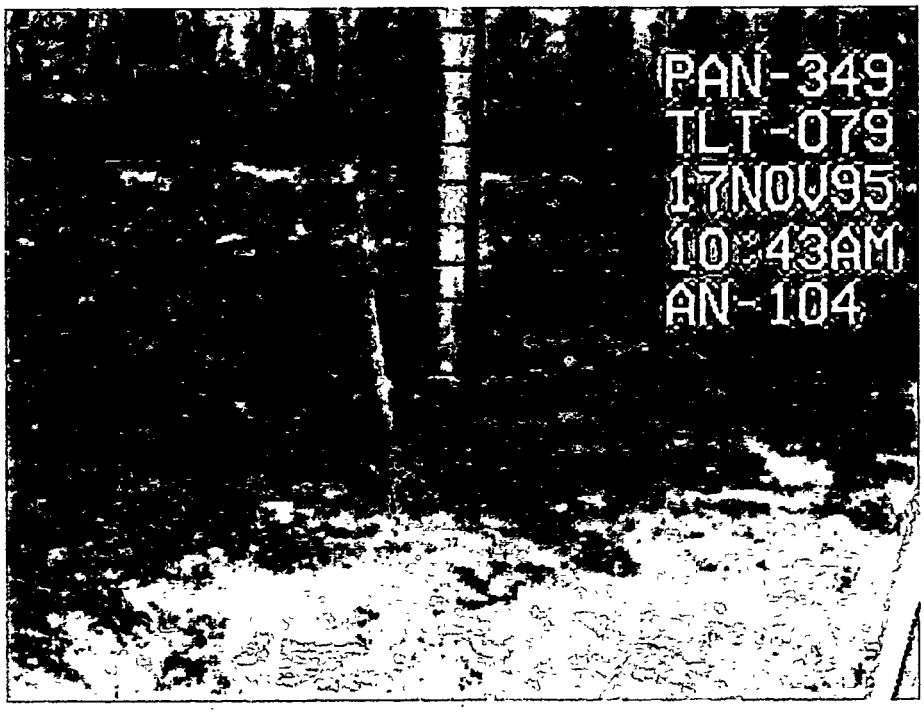

Figure 3.4.9. AN-104 Waste Surface, 1995

Figure 3.4.10. AN-105 Waste Surface, 1995

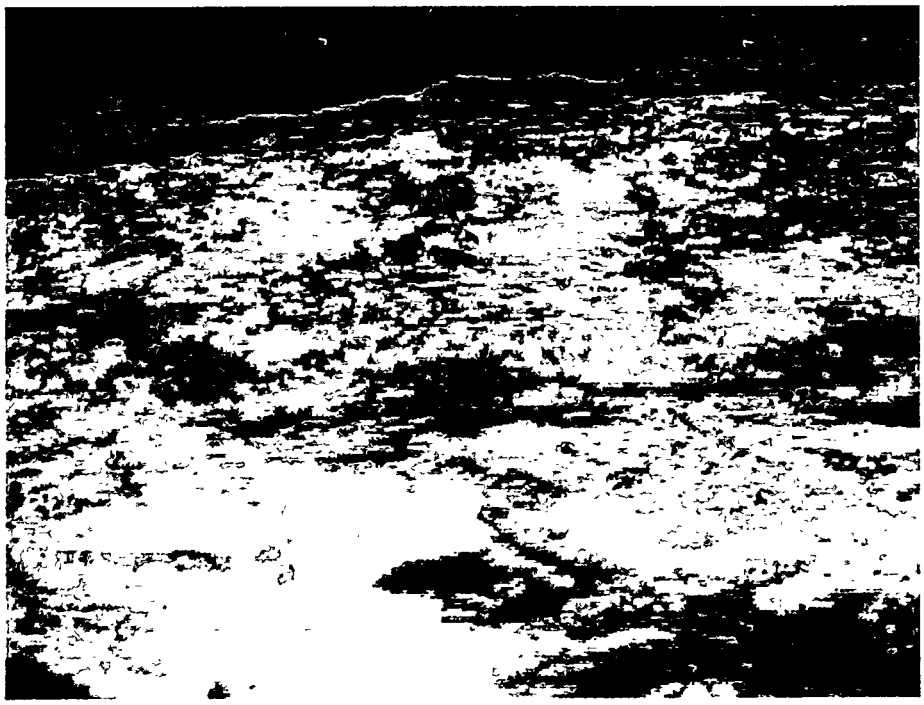

Figure 3.4.11. AW-101 Waste Surface, 1995

Figure 3.4.12 shows the waste surface of Tank SY-101 in October 1994. The mixer pump is in the center of the frame, and one of the velocity-density-temperature trees (VDTTs) is visible in the upper right. Comparison of surface features from December 1993 to 1995 shows absolutely no motion (Brewster et al. 1995). The dark areas are not liquid "lakes" but smoother areas of crust left after Event I, the last natural GRE in the tank. Figure 3.4.13 shows the waste disturbance during Event I on June 26, 1993. The view is from the side of the tank opposite Figure 3.4.12 above, in the direction of the VDTTs. Note the boil of waste to the right of the farthest VDTT and the splash at the base of the near one. The entire waste surface is moving to the left.

Figure 3.4.14 shows the crust floating on the surface of SY-103. This tank has the thinnest and least continuous crust of the six DSTs studied. Note the liquid surface near the tank walls.

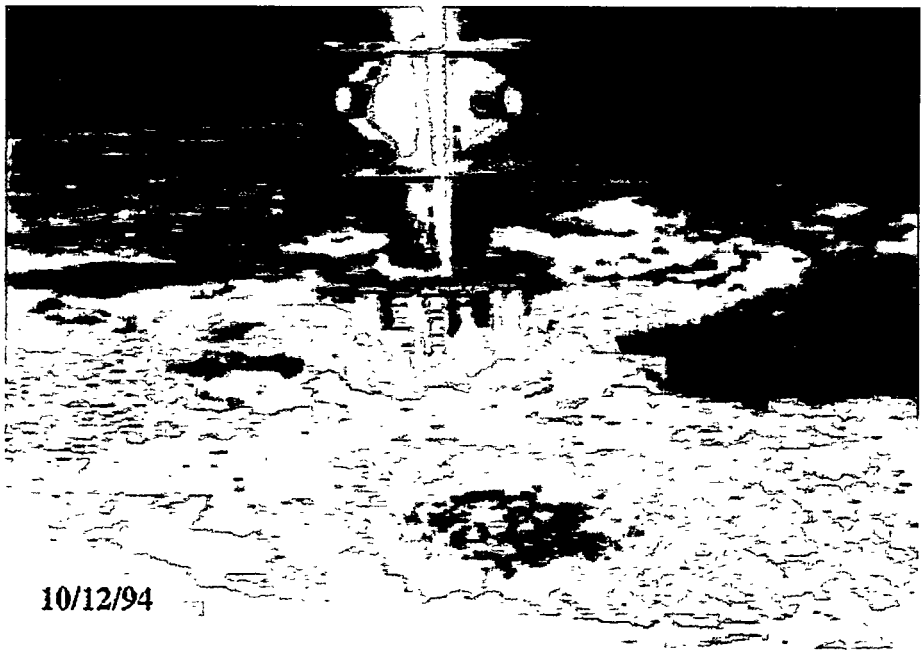

Figure 3.4.12. SY-101 Waste Surface, 1994

Figure 3.4.13. SY-101 Waste Surface During Event I, June 26, 1993

Figure 3.4.14. SY-103 Waste Surface, 1994

3.5 Recommendations for Improving Gas Retention Models

The data summarized in this section of the report present a reasonably complete picture of the condition and behavior of the waste in each of the six DSTs on the FGWL. The local void measurements allow a reasonably accurate estimate of the retained gas volume, its vertical distribution, and some information about its horizontal variability. The waste level and temperature data give a record of past tank behavior and reveal trends that predict at least the immediate future. The gas composition data permit an accurate assessment of the flammability potential following a release. The rheology and density data from the ball rheometer and core sample analysis give a detailed picture of the waste physical configuration and are essential elements of the predictive models described in later sections.

Though the data are probably sufficient for current analyses, some important information is lacking that would improve our confidence in predicting consequences of future actions and long-term effects. First, there is almost no reliable information on the size distribution and shape of the solid particles that retain the gas. The same is true for porosity. Without these data we cannot relate the other data (e.g., local void fraction, yield stress, etc.) to the configuration of the retained gas using the correlations developed by Gauglitz et al. (1995, 1996). Some means needs to be developed to measure particle size, capture particle shape, and assess the porosity/permeability of the solid-liquid matrix in-situ. Tests on core samples are suspect because of uncontrolled temperatures and the disturbance caused by sampling.

There are very few data of any kind from the crust layer. While this layer is stable, and there is no indication that it poses any significant hazard, the crust does contain a significant volume of gas and needs to be understood better. The only direct indication of crust thickness comes from the temperature profile (i.e., validation probe run in an MIT). It is impossible to estimate the crust thickness much closer than about 10 cm with this method. Also, the crust is known from in-tank video to vary considerably over the waste surface. Currently, we have no other information of what the horizontal variability in thickness, composition, or properties might be. Since the gas in the submerged part of the crust supports weight of the material above the liquid surface, there is an inverse lithostatic pressure gradient that peaks at the free liquid level. This effect has not yet been investigated in gas retention tests, and bubble configuration in the crust may differ from that shown in the tests of Gauglitz et al. (1996).

Indirect data on the dynamic behavior of the waste are also important. While not directly addressed in this report, the head-space gas composition and humidity and the active and passive ventilation flow rates are important in assessing the safety state of the tank. SHMS and gas characterization systems (GCS) have been installed on many tanks, and more are being installed. The most urgent improvement needed in gas monitoring is high-quality data. Strip charts are still being used to record the data in many cases, and the system calibration often drifts so far that only changes in concentration can be determined (see Wilkins et al. 1996). The gas monitoring systems need to be modified to record data digitally, on a network, and their calibration needs to be stabilized.

This brings up possibly the most important recommendation regarding data. Data management must be made as high a priority as the measurement and analysis. Data management is becoming increasingly important as more data are generated. We strongly recommend that data management be elevated in importance and that a major effort be mounted to modernize the data stream.

The ball rheometer data in the six DSTs provide a unique opportunity to validate a more sophisticated BPE model that includes the effects of waste strength. The model, developed by

Whitney et al. (1996), assumes that expansion or compression of retained gas bubbles is resisted elastically by the waste until it yields. After yielding, the waste is assumed to deform plastically as the bubbles expand further. The model duplicates the "parallelogram" hysteresis behavior observed in plots of surface level versus barometric pressure in several SSTs. An example is sketched in Figure 3.5.1. The arrows indicate the path for passage of a single low-pressure system over a 1–3 day period. Long-term plots show a series of overlaid parallelograms.

Applying the improved BPE model not only gives a better gas volume estimate but also provides an indicator of the waste yield stress. Since the yield stress has already been measured in the six DSTs, and an accurate determination has been made of the gas volume, this improved model could be easily validated for use in other tanks. This would be extremely valuable in determining the tendency for waste newly transferred into a DST to retain gas.

To provide the required information, precise hourly waste level measurements are required. The Enraf level gauges currently installed in the six DSTs are sufficiently precise. Unfortunately, they are being read manually only once a day. We strongly recommend that automated hourly level measurements be made with the Enraf gauges in the DSTs as soon as possible.

The BPE model provides better estimates of stored gas volume the better the vertical distribution of gas is known. Since the gas distribution has been measured in DSTs, relatively accurate predictions are possible. However, the gas distribution is currently known in only one SST as a result of the RGS measurements. After the RGS has been operated in several SSTs, estimates of the gas distribution can be made for other tanks of similar waste type. We recommend that RGS testing continue to supply these data.

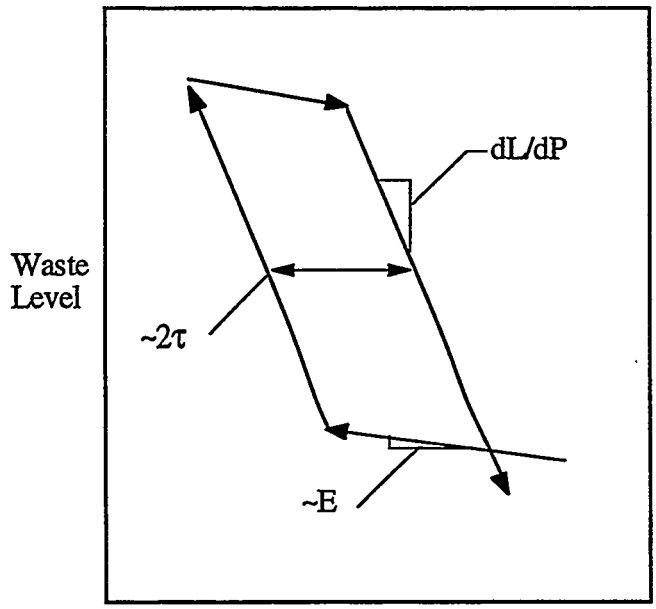

Figure 3.5.1. Pressure-Level Hysteresis Example

4.0 Prediction of Gas Release Behavior

Section 3 presented the retained gas volume derived from local void measurements obtained from the six DSTs on the FGWL. Section 5 discusses the potential consequences in terms of peak dome pressure resulting from a deflagration involving all or part of the gas inventory. This section describes the historical gas release behavior of the six tanks and presents new models to predict gas release volume. An important consideration in flammable gas safety is the potential for the expected gas release volume to vary with long-term changes in the waste. It is also highly desirable to be able to predict the size of potential GREs following waste transfers. The data have enabled us to develop models that can predict how large a gas release to expect in these situations.

As discussed in Section 1, the episodic GREs historically observed in the six DSTs on the FGWL are believed to occur by the process of *buoyant displacement.* In a buoyant displacement, the nonconvective layer near the tank bottom accumulates gas until it becomes lighter than the convective layer above it. At this point, a portion, or *gob,* of nonconvective material suddenly breaks away and rises through the supernatant liquid layer. The stored gas bubbles may expand as the gob rises. Where bubble expansion is sufficient to fail the ambient matrix, gas will be released from the gob and, if not trapped by existing crust, may escape into the head space

We hypothesize that the characteristic size of a buoyant gob (and the subsequent gas content) is controlled by two competing physical phenomena. The first phenomenon relates to static forces and buoyancy. Since the nonconvective layer is a viscoplastic material, the concept of buoyancy is somewhat modified from the familiar meaning in Newtonian fluids. The forces resulting from normal stresses around a region of low-density viscoplastic material must overcome both the weight of the region and the material strength on the boundaries of the region. Hence, a larger buoyant force is required to achieve an instability. The amount of gas accumulation required for buoyancy will depend on the size and shape (surface area) of a gob as well as the yield strength of the material.

The second phenomenon relates to dynamic instabilities. A viscoplastic material behaves like a fluid once the yield stress is surpassed. We know that when a heavier fluid layer is superposed on a lighter fluid layer, regions of heavier fluid will fall and regions of lighter fluid will rise according to the well-known Rayleigh Taylor instability theory. The wavelength, or characteristic size of the moving regions, depends on the relative densities and viscosities of the two layers. Hence, if we view the nonconvective layer as a viscous fluid, the size of an unstable gob will depend on density (gas accumulation) as well as viscosity.

The average size of an unstable gob undergoing buoyant displacement is dictated by the combined effects of the mechanisms described above. The actual size of a GRE will be determined by the size of the gob, the volume of gas within the gob, and the fraction of gas that escapes during a buoyant displacement. After a buoyant displacement occurs, we assume the gob sinks back to the nonconvective layer with a reduced gas inventory. Over time, heterogeneities develop in the nonconvective layer as buoyant gobs rise, release gas, sink, then repeat the process. This dynamic cycle could provide slow mixing in the nonconvective layer over time. The average time required for a single GRE is dictated by a gob's initial gas content (immediately after a GRE), the amount of gas required to initiate buoyant displacement, and the gas generation rate. The average GRE frequency in a given tank is related to the total number of gobs possible and the GRE frequency for each gob.

The physical processes described above form the basis of the analytical models presented in this section. The modeling approach is to capture the first-order effects of the assumed physical processes by making heuristic arguments and simplifying assumptions wherever possible. We do

not deny the complexity of the dynamic physical situations in the DSTs, and we recognize that simple models will not accurately represent all the details of the actual heterogeneous waste behavior. However, we believe a simplified approach is appropriate for understanding and predicting basic GRE behavior.

This section is organized in the following way: Section 4.1 summarizes the historical GRE behavior of each tank, and Section 4.2 addresses waste properties and the assumed waste configuration to be modeled. Section 4.3 examines the essential mechanism of buoyancy, the stabilizing effect of material yield strength, and the geometry of the buoyant gob. Section 4.4 presents results of a stability analysis for the buoyant nonconvective layer. In Section 4.5, the results of the previous two sections are combined to obtain predictive models for the size and frequency of GREs. Section 4.6 presents a criterion for gas release during buoyant displacement. This is a complementary analysis that considers the energetics of the buoyant displacement process. Section 4.7 provides recommendations for improving gas release models.

4.1 Historic Gas Release Behavior

This section describes the historical gas releases in the six tanks studied in this report as observed in the waste level history. The GRE history for a typical tank prior to the mid-1990s must be derived from the waste level history, usually as measured by an FIC contact probe or Enraf buoyancy gauge (since about 1995). The manual tape or other devices are suitable for identifying but not quantifying some of the larger releases. GREs are identified by a sudden level drop following a long period of steady level rise. The initial drop is usually followed by a slower decline to a minimum level several days or even a couple of weeks after the main event. Often there is an accelerated or even abrupt level rise just before the event.

During a buoyant displacement event, the expansion of the gas in the rising gob will produce a level rise if it occurs slowly or if the gas is not released immediately. At the surface, gas is released until the gob returns to approximately neutral buoyancy at the surface. This causes the sudden level drop that is the signature of a classic "rollover." Then the gob may disintegrate as pieces sink back to the bottom, compressing the gas that remains trapped. This final process produces the slower level decline that occurs days or even weeks after the actual release. Only the initial level drop should be used to compute the release since only this phase of the GRE is accompanied by a rapid release of gas into the head space.

A gas release is assumed to be indicated by a sharp level drop of at least 0.75 cm, which is essentially the limit of detection, or a sharp rise immediately followed by a sudden drop. To ensure that all level drops were evaluated, a procedure was applied that locates statistically significant breaks in the level history (rises or drops) that might indicate a GRE (Whitney et al. 1996). Once the level breaks are identified, the waste level history must be screened to weed out false positives resulting from occasional FIC flushes or spurious readings recorded in the operations log. The validated list of breaks in each tank must then be evaluated one by one, by inspecting the daily level data with a generous application of human judgment. There is a good bit of art in this step, and different analysts could record different sets of GREs.[a] There is no doubt about the larger ones (e.g., SY-101 prior to mixing), but there is considerable doubt about the barely detectable drops in AN-101 and AW-101, for example.

(a) The GREs listed in this section were identified by CW Stewart. Use of the procedure in Whitney et al. (1996) produced slightly different list than given in Stewart et al. (1996a), which was also identified by Stewart directly from the level data.

Once the list of GREs is selected, the gas release is calculated from the difference between the peak waste level immediately before the drop and the level on the next day, even if the level on subsequent days is lower. The gas release is assumed to originate in the nonconvective layer, because the convective layer contains essentially no gas and the gas stored in the crust apparently does not participate heavily, as evidenced by the quick re-establishment of the crust layer in SY-101 following large releases. The standard gas release volume is computed as

$$\hat{V}_{REL} = \Delta L_{GRE} A P_{NC} \tag{4.1.1}$$

where ΔL_{GRE} is the initial level drop, A is the tank area, and P_{NC} is the average pressure ratio (includes both temperature and pressure effects) of the gas stored in the nonconvective layer defined by Eq. (3.1.15). In some tanks, gas releases occur with no surface level change, or the releases are so small as to challenge the resolution of the level measurement—this is particularly true of AW-101 and AN-103.

The gas inventory in the nonconvective layer immediately before the GRE is calculated from the difference between the pre-GRE waste level and the effective waste level if all the gas in the nonconvective layer were removed. The pre-GRE standard volume in the nonconvective layer is given by

$$V_{Pre-GRE} = (L_{GRE} - L_{NO-GAS}) A P_{NC} \tag{4.1.2}$$

where L_{GRE} is the pre-GRE waste level, and L_{NO-GAS} is the waste level that would exist if all gas in the nonconvective layer were removed. The degassed level was derived from the local void measurements in Section 3.1 (see Eq. (3.1.24). Note that volumes calculated by Eq. (4.1.2) will differ from those given in Table 3.1.2, row 9 because L_{GRE} differs from the level at the time the void measurements were made.

The release fraction is estimated from the tank level history as the ratio of gas volume released to the gas volume in the nonconvective layer immediately prior to the GRE. The release fraction is calculated by

$$F_{REL} = \frac{\Delta L_{GRE}}{L_{GRE} - L_{NO-GAS}} \tag{4.1.3}$$

where ΔL_{GRE} is the level drop from immediately prior to one day following the GRE. Note that the release fraction is independent of gas pressure.

The gas release history of each of the six DSTs on the FGWL was given earlier in Stewart et al. (1996a).[a] We had hoped to be able to add a list of GREs derived from the SHMS, particularly for AW-101 and AN-103, whose level history is not a good indicator of gas release. However, calculating gas release volumes from SHMS data requires assuming the head space is fully mixed at all times (unless a detailed computational simulation is performed). Since the mixing time is on the order of one hour, it is clear that this assumption is not valid for the initial stages of small releases, and the gas release volumes so calculated would be highly uncertain, although SHMS data remain the clearest evidence that a GRE has occurred. Therefore, we believe that level drop remains the best characterization of historic GRE behavior at this time.

(a) All gas release parameters for SY-101 represent conditions prior to installation of the mixer pump July 4, 1993.

The rest of this section contains, for each of the six tanks, a table describing each recorded GRE (Tables 4.1.2 through 4.1.7), a histogram representing the distribution of GRE sizes taken from the table, and a plot of the waste level history (Figures 4.1.1 through 4.1.12). The GRE behavior of each tank determined from this information is summarized in Table 4.1.1. Except for SY-101, the GRE period was averaged from only the most recent five years. Note that, also except for SY-101, the periods have such a high uncertainty as to be unpredictable.

Table 4.1.1. Gas Release History

Tank	Pre-GRE Volume (m^3 at STP)	GRE Volume (m^3 at STP)	Release Fraction	GRE Period (days)
AN-103	280 ± 17	14 ± 4	0.05 ± 0.02	160 ± 120
AN-104	236 ± 23	23 ± 16	0.10 ± 0.06	120 ± 90
AN-105	184 ± 29	26 ± 11	0.15 ± 0.06	160 ± 130
AW-101	64 ± 15	14 ± 10	0.23 ± 0.15	220 ± 230
SY-101	394 ± 84	131 ± 47	0.34 ± 0.13	110 ± 24
SY-103	151 ± 21	13 ± 6	0.09 ± 0.04	90 ± 70

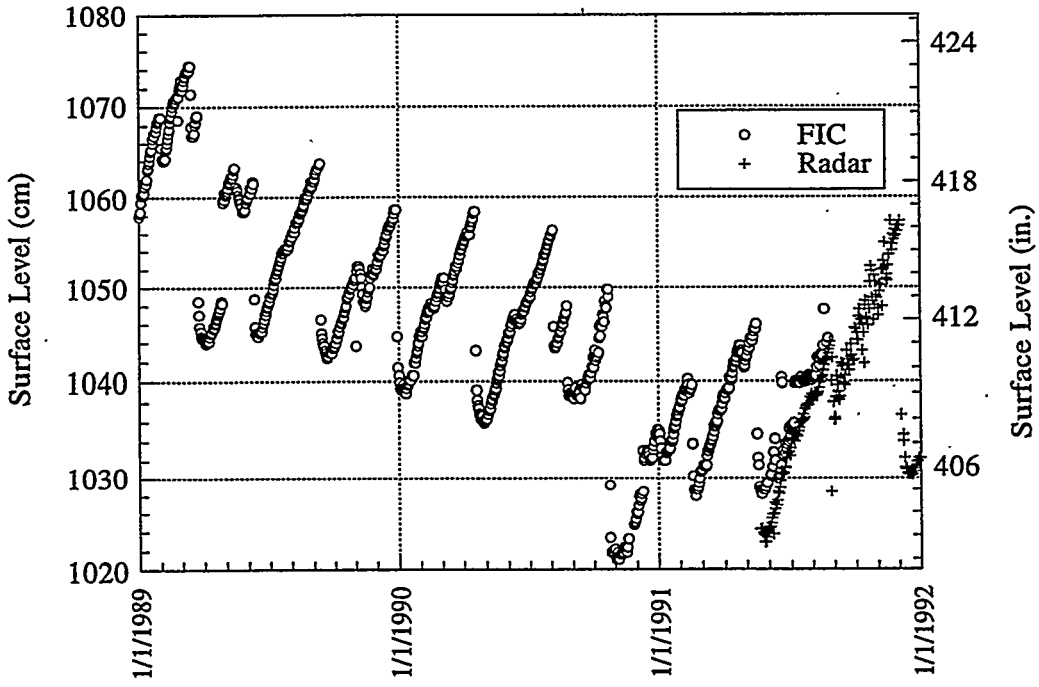

Figure 4.1.1. SY-101 Waste Level History, January 1989 to January 1992

Table 4.1.2. SY-101 GRE History

Event	Date	Level (cm)			Standard Volume (m^3)			Period
		Before	After	Drop	Release	Before	Fraction	(days)
	03/25/89	1074.9	1054.3	20.6	186.3	586.4	0.318	0
	06/10/89	1062.7	1050.0	12.7	115.0	476.3	0.242	77
	09/12/89	1063.5	1046.2	17.3	156.2	483.1	0.323	94
	12/30/89	1057.9	1044.7	13.2	119.3	432.7	0.276	109
	04/19/90	1057.9	1038.9	19.0	171.7	432.7	0.397	110
	08/05/90	1056.6	1048.0	8.6	78.0	421.2	0.185	108
A	10/24/90	1050.3	1036.1	14.2	128.1	363.9	0.352	80
B	02/16/91	1039.1	1033.3	5.8	52.5	262.9	0.200	115
C	05/16/91	1046.5	1037.9	8.6	77.5	329.5	0.235	89
D	08/27/91	1049.0	1035.1	14.0	126.2	352.4	0.358	103
E	12/04/91	1057.4	1036.7	20.7	187.0	428.1	0.437	99
F	04/20/92	1051.6	1044.5	7.1	63.8	375.3	0.170	138
G	09/03/92	1043.6	1021.1	22.5	203.2	303.4	0.670	136
H	02/02/93	1044.7	1029.0	15.7	141.8	313.4	0.452	152
I	06/26/93	1048.5	1030.9	17.6	159.1	347.8	0.457	144
			Avg.	14.5	131.0	393.9	0.338	110
			St. Dev.	5.2	47.3	83.6	0.133	24

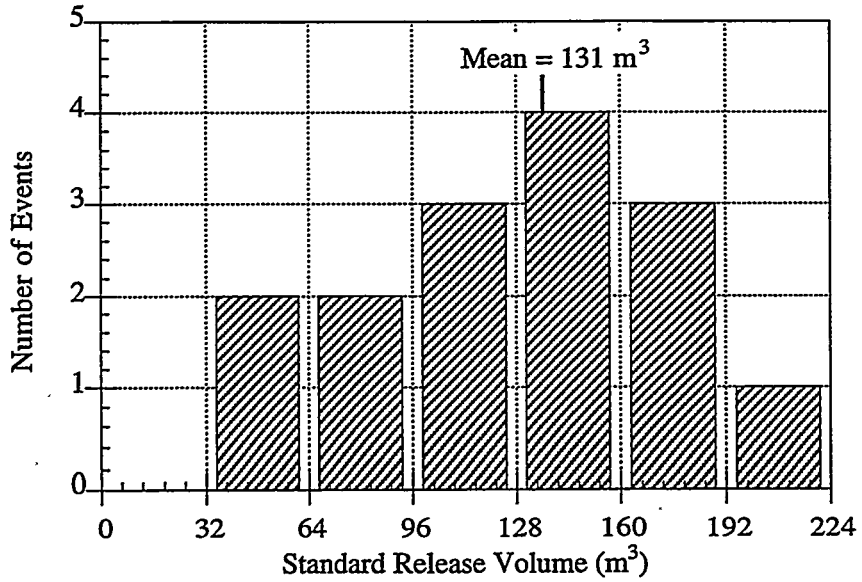

Figure 4.1.2. Historical Gas Release Distribution in SY-101

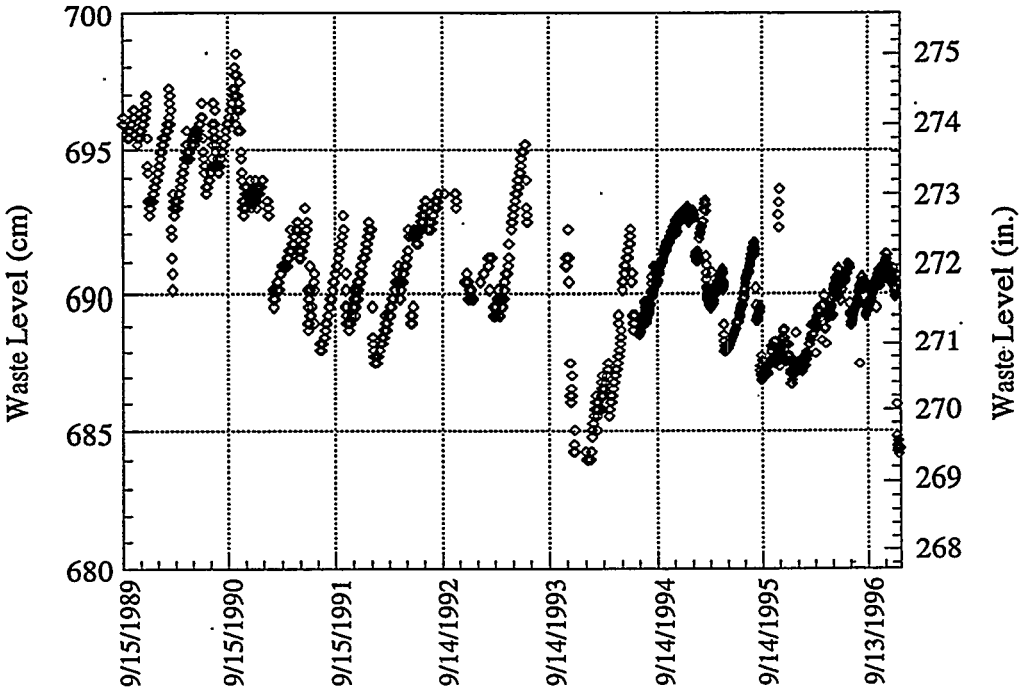

Figure 4.1.3. SY-103 Waste Level History, October 1989 to January 1997

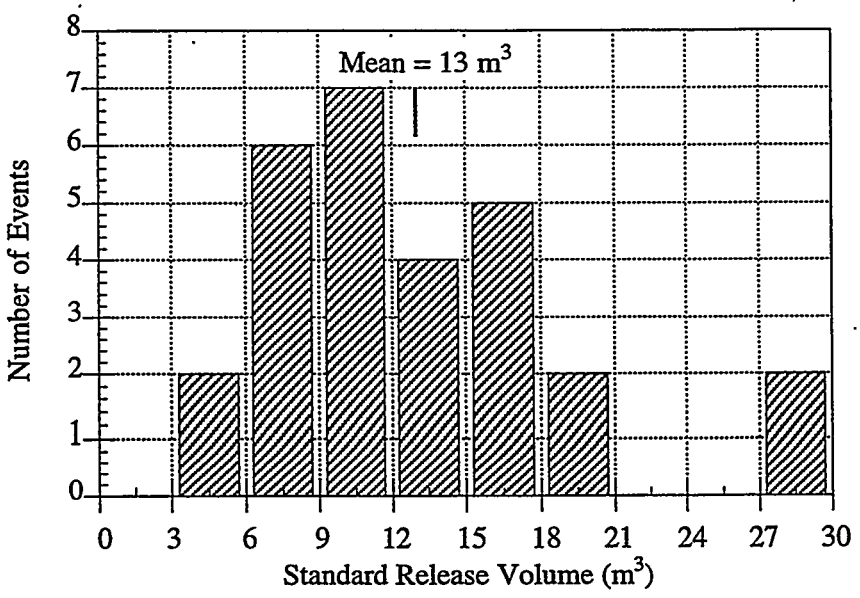

Figure 4.1.4. Historical Gas Release Distribution in SY-103

Table 4.1.3. Summary of GREs in SY-103

Date	Level (cm)			Volume (m^3)			Period (days)
	Before	After	Drop	Released	Before	Fraction	
12/8/89	697.0	695.5	1.5	10.2	187.1	0.055	0
3/2/90	696.5	692.2	4.3	29.6	183.6	0.161	84
6/20/90	696.2	694.9	1.3	9.1	181.9	0.050	110
8/2/90	696.5	694.9	1.6	11.1	183.8	0.060	43
10/27/90	696.5	694.9	1.6	11.1	183.8	0.060	86
2/1/91	692.7	689.9	2.8	19.1	157.2	0.122	97
5/12/91	692.4	691.4	1.0	6.9	155.4	0.045	100
6/11/91	692.4	690.1	2.3	15.8	155.4	0.102	30
7/6/91	690.6	689.1	1.5	10.6	143.1	0.074	25
1/17/92	692.2	689.6	2.5	17.6	153.7	0.115	195
5/27/92	691.9	689.4	2.5	17.6	151.9	0.116	131
11/21/92	693.2	688.9	4.3	29.6	160.7	0.184	178
7/1/93	695.2	693.9	1.3	8.8	174.8	0.050	222
11/22/93	690.4	687.6	2.8	19.4	141.3	0.137	144
12/5/93	686.5	684.3	2.2	15.3	114.5	0.133	13
2/20/94	686.1	685.0	1.0	7.0	111.3	0.063	77
3/10/94	687.1	685.8	1.3	8.8	118.4	0.074	18
4/2/94	687.6	685.6	2.0	14.1	122.0	0.115	23
6/16/94	692.2	690.4	1.8	12.3	153.7	0.080	75
6/22/94	690.6	689.4	1.3	8.8	143.1	0.062	
1/22/95	692.7	691.2	1.5	10.4	157.4	0.066	214
3/2/95	693.0	690.9	2.1	14.8	159.8	0.093	39
5/2/95	690.2	688.4	1.8	12.3	140.3	0.088	61
8/233/95	691.5	690.2	1.3	9.0	149.2	0.060	113
9/6/95	689.5	687.3	2.2	15.2	135.0	0.113	14
12/4/95	688.3	687.7	0.6	4.2	127.0	0.033	89
6/6/96	690.8	690.0	0.8	5.5	144.3	0.038	185
7/14/96	690.8	689.7	1.1	7.6	144.3	0.053	38
		Average	1.9	12.9	151.2	0.086	90
		St. Dev.	0.9	6.2	21.5	0.039	65

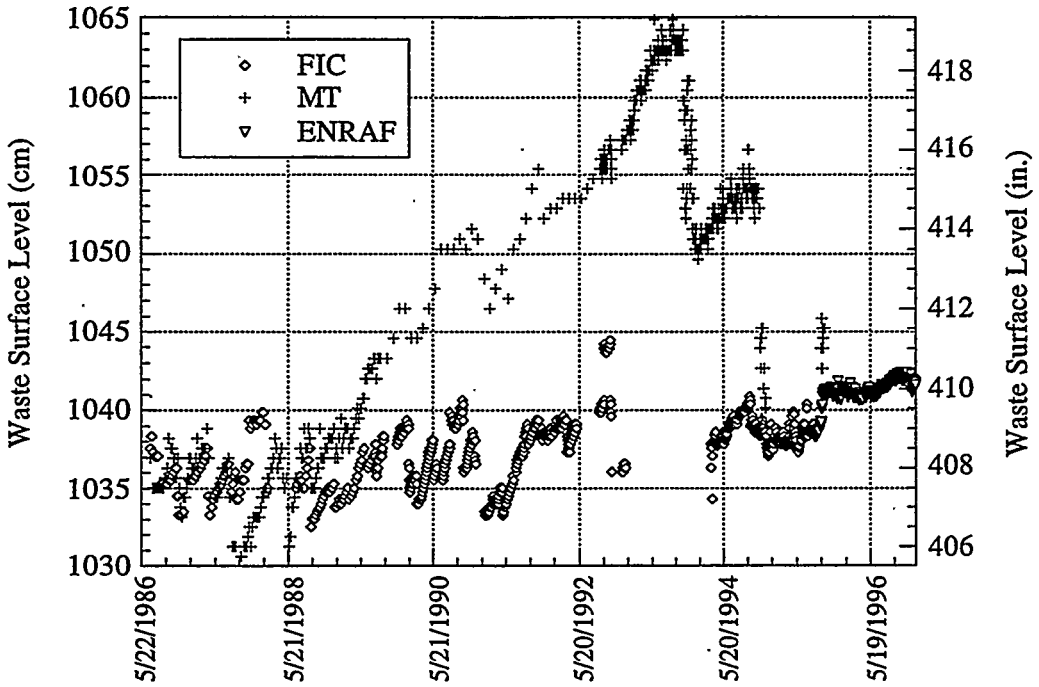

Figure 4.1.5. AW-101 Waste Level History, 1986–1996

Table 4.1.4. AW-101 GRE History

	Level (cm)			Standard Volume (m^3)			Period
Date	Before	After	Drop	Released	Before	Fraction	(days)
11/17/86	1036.32	1034.5	1.8	15.8	55.0	0.288	0
4/20/87	1037.6	1034.5	3.1	27.0	66.1	0.408	154
8/3/87	1036.1	1034.8	1.3	11.3	53.1	0.213	105
9/7/87	1036.1	1034.3	1.8	15.7	53.1	0.295	35
9/12/88	1037.6	1032.5	5.1	44.4	66.1	0.671	371
1/9/89	1035.3	1033.8	1.5	13.1	46.1	0.283	119
3/20/89	1035.1	1034.3	0.8	7.0	44.4	0.157	70
8/4/89	1037.1	1036.3	0.8	7.0	61.8	0.113	137
1/17/90	1038.8	1036.6	2.3	19.7	77.1	0.255	166
2/28/90	1035.3	1034.0	1.3	11.3	46.1	0.245	42
5/3/91	1035.1	1033.3	1.8	15.7	44.4	0.353	429
9/10/91	1038.9	1038.1	0.8	7.0	77.5	0.090	130
11/3/91	1039.4	1038.6	0.8	7.0	81.8	0.085	54
3/21/92	1039.4	1037.3	2.1	18.3	81.8	0.223	139
4/10/94	1038.6	1037.8	0.8	7.0	74.8	0.093	750
10/4/94	1040.4	1039.0	1.4	12.2	90.5	0.135	177
12/22/94	1038.4	1037.8	0.6	5.2	73.1	0.071	79
		Average	1.7	14.4	64.3	0.234	220
		St. Dev.	1.1	9.7	15.1	0.151	230

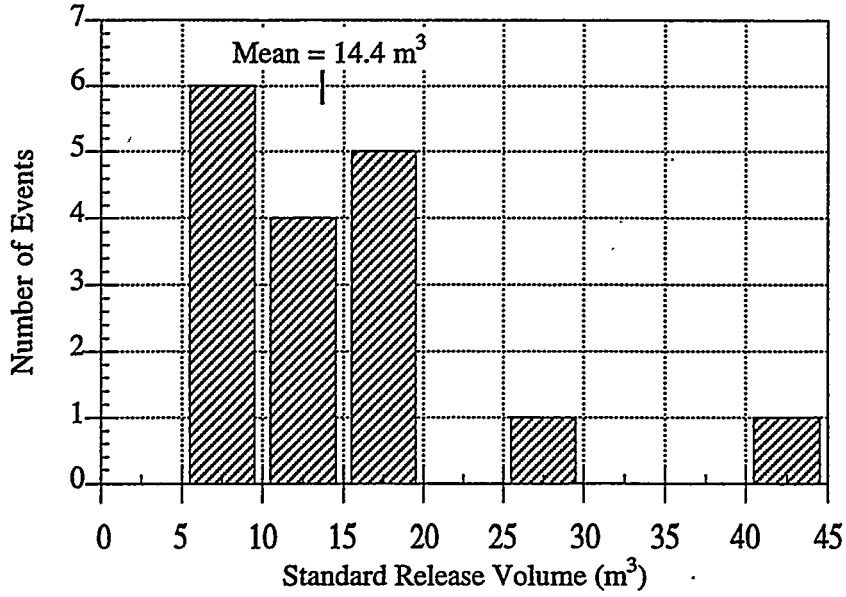

Figure 4.1.6. Historical Gas Release Distribution in AW-101

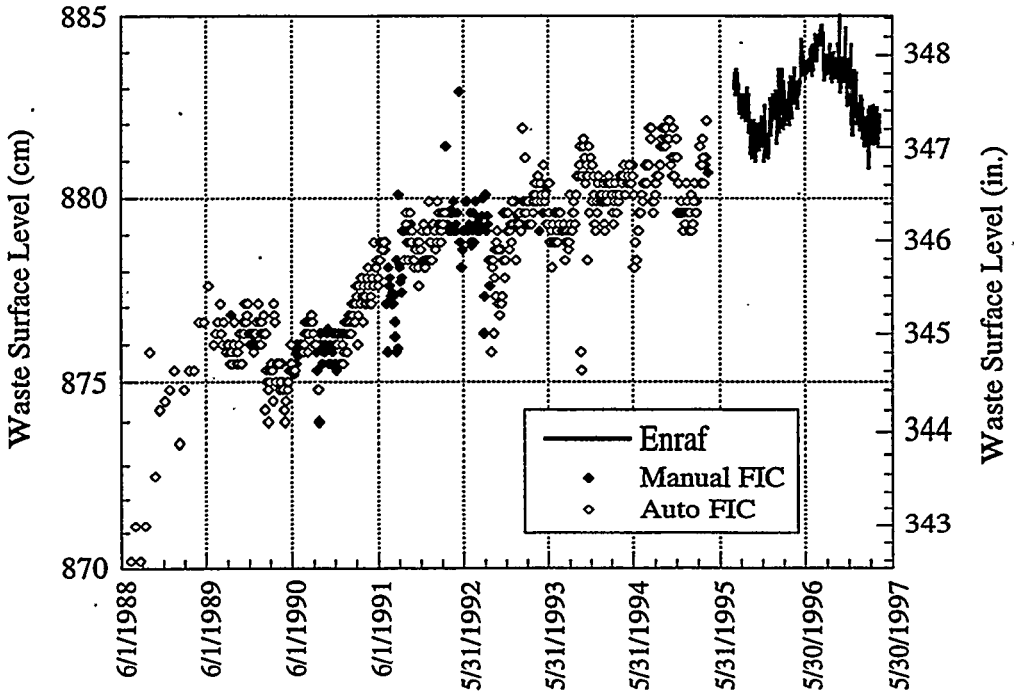

Figure 4.1.7. AN-103 Waste Level History, June 1988 to June 1997

Table 4.1.5. AN-103 GRE History

Date	Level (cm)			Standard Volume (m^3)			Period (days)
	Before	After	Drop	Released	Before	Fraction	
6/1/89	877.1	876.0	1.1	8.4	261.7	0.032	0
8/4/89	877.3	876.3	1.0	7.7	263.3	0.029	64
2/11/90	876.3	874.8	1.5	11.5	255.6	0.045	191
2/18/90	875.0	874.0	1.0	7.7	245.6	0.031	
9/26/90	878.6	877.1	1.5	11.5	273.2	0.042	220
7/6/91	878.8	877.1	1.7	13.0	274.8	0.047	283
8/24/91	878.3	875.9	2.4	18.4	270.9	0.068	49
9/14/91	880.4	879.1	1.3	10.0	287.0	0.035	21
8/25/92	878.8	876.3	2.5	19.2	274.8	0.070	346
9/25/92	878.3	876.3	2.0	15.4	270.9	0.057	31
10/23/92	879.1	876.3	2.8	21.5	277.1	0.078	28
11/23/92	879.6	878.1	1.5	11.5	280.9	0.041	31
2/10/93	881.6	880.1	1.5	11.5	296.3	0.039	79
11/15/93	880.4	878.3	2.1	16.1	287.0	0.056	278
11/23/93	881.4	878.6	2.8	21.5	294.7	0.073	
8/20/94	882.1	879.9	2.2	16.9	300.1	0.056	270
12/4/94	880.6	878.8	1.8	13.8	288.6	0.048	106
8/17/95	882.9	881.7	1.2	9.2	306.2	0.030	256
2/10/96	883.5	881.8	1.7	13.0	310.8	0.042	177
		Average	1.8	13.6	280.0	0.048	155
		St. Dev.	0.6	4.4	17.3	0.015	118

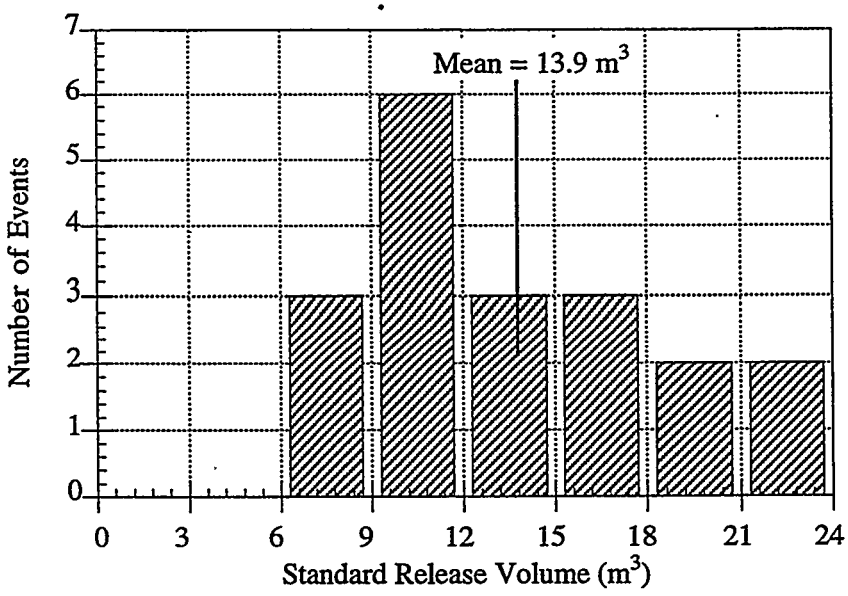

Figure 4.1.8. Historical Gas Release Distribution in AN-103

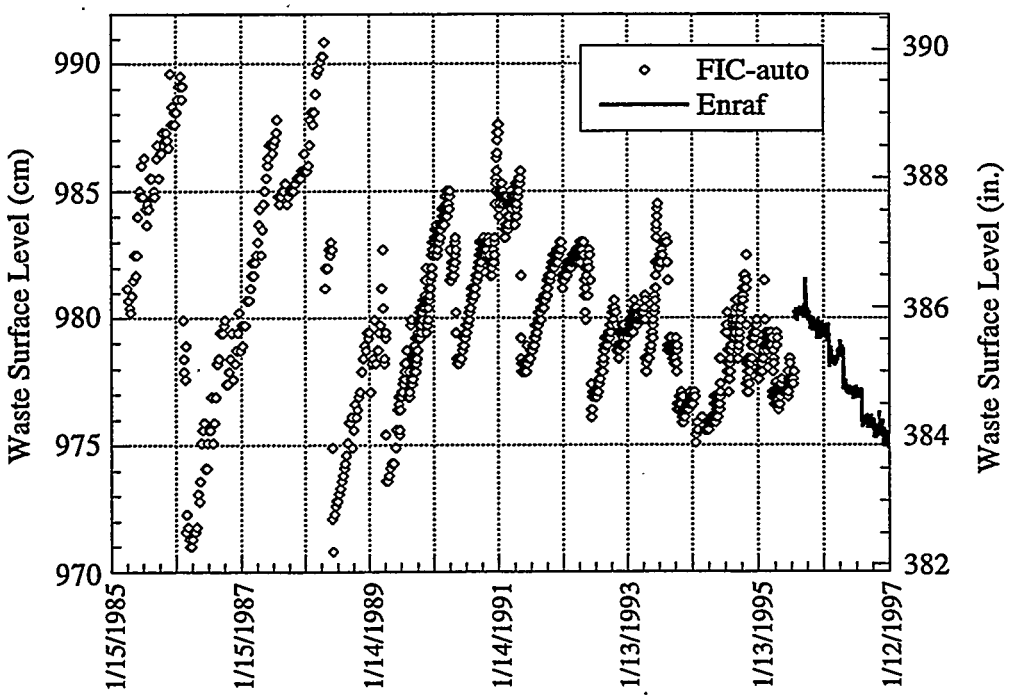

Figure 4.1.9. AN-104 Waste Level History, January 1985 to January 1997

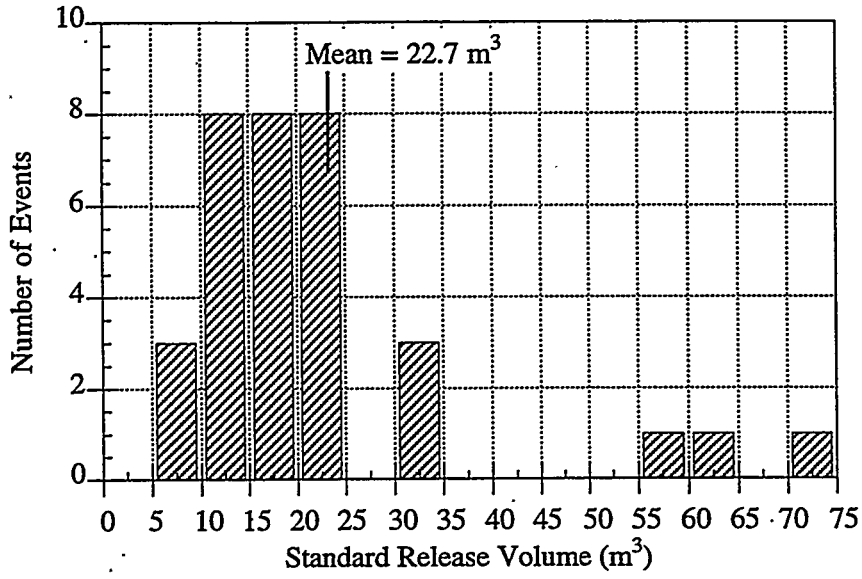

Figure 4.1.10. Historical Gas Release Distribution in AN-104

Table 4.1.6. AN-104 GRE History

Date	Level (cm)			Standard Volume (m^3)			Period (days)
	Before	After	Drop	Released	Before	Fraction	
2/27/86	989.1	979.9	9.2	74.4	291.9	0.255	
3/13/86	978.9	971.6	7.3	59.0	209.4	0.282	14
10/27/86	979.9	977.4	2.5	20.2	217.5	0.093	228
8/17/87	987.8	984.8	3.0	24.3	281.4	0.086	294
6/17/88	982.7	974.9	7.8	63.1	240.1	0.263	305
4/19/89	979.4	975.4	4.0	32.3	213.5	0.152	306
11/1/89	980.4	979.2	1.2	9.7	221.5	0.044	196
12/4/89	982.0	979.7	2.3	18.6	234.5	0.079	33
1/31/90	983.7	982.5	1.2	9.7	248.2	0.039	58
4/16/90	985.0	982.7	2.3	18.6	258.7	0.072	75
5/20/90	982.7	980.2	2.5	20.2	240.1	0.084	34
1/18/91	987.3	984.3	3.0	24.3	277.3	0.087	243
2/17/91	984.8	983.2	1.6	12.9	257.1	0.050	30
5/20/91	985.8	981.7	4.1	33.2	265.2	0.125	92
5/21/91	981.7	979.2	2.5	20.2	232.1	0.087	
1/3/92	983.0	981.7	1.3	10.5	242.6	0.043	227
5/12/92	983.0	981.2	1.8	14.6	242.6	0.060	130
6/18/92	981.5	977.4	4.1	33.2	230.4	0.144	37
4/27/93	979.9	977.9	2.0	16.2	217.5	0.074	313
7/9/93	984.5	982.0	2.5	20.2	254.7	0.079	73
8/31/93	981.5	978.9	2.6	21.0	230.4	0.091	53
10/24/93	978.9	976.6	2.3	18.6	209.4	0.089	54
2/1/94	976.9	975.5	1.4	11.3	193.2	0.059	100
7/25/94	980.2	977.9	2.3	18.6	219.9	0.085	174
9/19/94	980.7	978.4	2.3	18.6	224.0	0.083	56
11/7/94	982.5	979.7	2.8	22.6	238.5	0.095	49
2/17/95	981.5	979.9	1.6	12.9	230.4	0.056	
10/2/95	981.5	979.2	2.3	18.6	230.4	0.081	227
10/8/95	981.0	979.6	1.4	11.3	226.4	0.050	
5/4/96	978.7	977.2	1.5	12.1	207.8	0.058	209
		Average	2.9	23.4	236.2	0.098	121
		St. Dev.	1.9	15.8	23.0	0.063	88

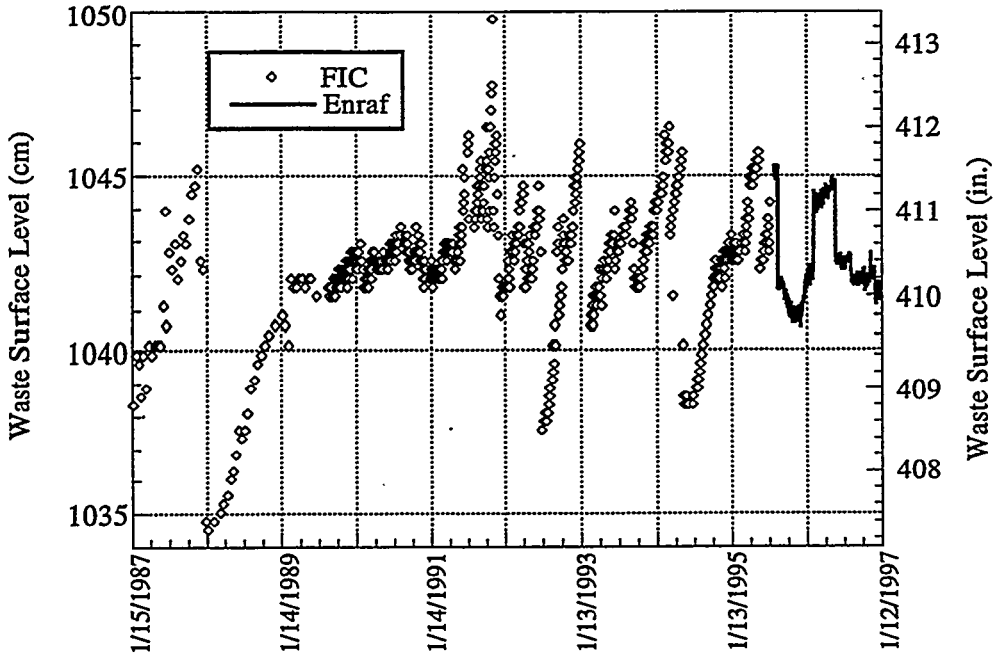

Figure 4.1.11. AN-105 Waste Level History, January 1987 to January 1997

Table 4.1.7. AN-105 GRE History

Date	Level (cm)			Standard Volume (m^3)			Period (days)
	Before	After	Drop	Released	Before	Fraction	
5/20/85	1036.8	1034.5	2.3	19.7	127.0	0.155	0
12/2/85	1036.8	1033.8	3.0	25.7	127.0	0.203	196
8/11/86	1041.9	1035.8	6.1	52.3	170.7	0.307	252
1/5/87	1040.9	1038.4	2.5	21.4	162.1	0.132	147
2/24/87	1041.1	1038.6	2.5	21.4	163.8	0.131	50
8/17/87	1042.9	1041.1	1.8	15.4	179.3	0.086	174
12/7/87	1045.2	1041.9	3.3	28.3	199.0	0.142	112
1/4/88	1042.2	1038.4	3.8	32.6	173.3	0.188	28
1/8/88	1038.4	1034.8	3.6	30.9	140.7	0.220	4
7/19/91	1047.2	1043.7	3.5	30.0	216.2	0.139	
9/17/91	1045.5	1043.7	1.8	15.4	201.6	0.077	60
11/15/91	1049.8	1043.9	5.9	50.6	238.5	0.212	59
12/6/91	1046.2	1044.4	1.8	15.4	207.6	0.074	21
4/14/92	1044.7	1042.9	1.8	15.4	194.7	0.079	130
7/6/92	1042.7	1038.1	4.6	39.5	177.6	0.222	83
9/27/92	1043.4	1040.9	2.5	21.4	183.6	0.117	83
1/23/93	1046.0	1043.7	2.3	19.7	205.9	0.096	118
9/19/93	1046.0	1042.9	3.1	26.6	205.9	0.129	239
5/17/94	1045.7	1042.9	2.8	24.2	203.5	0.119	240
8/24/95	1045.2	1041.6	3.6	31.0	199.1	0.156	464
5/31/96	1044.8	1043.1	1.7	14.8	195.6	0.075	281
		Average	3.1	26.3	184.4	0.146	162
		St. Dev.	1.3	10.7	28.7	0.061	132

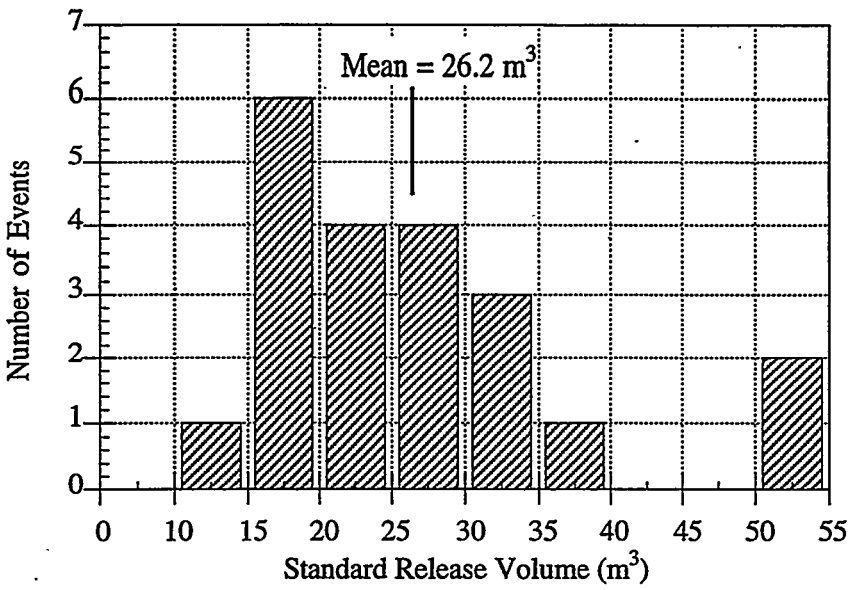

Figure 4.1.12. Historical Gas Release Distribution in AN-105

4.2 Waste Configuration and Properties

A simplified model for DST waste configuration is shown in Figure 4.1.1. The typical waste configuration in tanks subject to buoyant displacement consists of a convective liquid layer overlying a layer of nonconvective sludge-like material. In some cases there is a crust layer above the liquid layer. In-situ measurements with the ball rheometer (Stewart et al. 1996a) indicate that the convective layer is a Newtonian fluid, whereas the nonconvective layer is a shear-rate-dependent material with a finite yield strength (viscoplastic) that is able to retain gas generated in the waste.

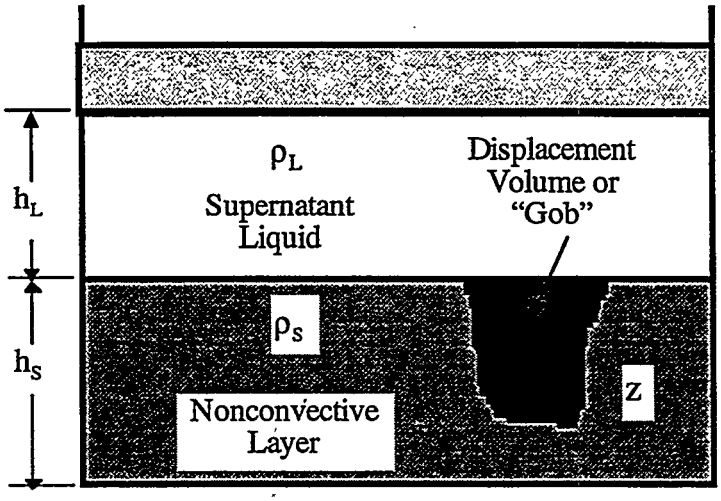

Figure 4.2.1. Waste Configuration for a Typical DST Experiencing GREs

The properties of the waste (density, gas fraction, yield strength) generally vary temporally and spatially. To formulate simple predictive models we use average, or mean, properties. This is consistent with our modeling philosophy since we are seeking to capture first-order physical effects that relate to the general magnitude of properties and not to subtle variations. Furthermore, the present data set is inadequate to accurately represent property variability. It is possible that some characteristic behaviors of GREs are fundamentally attributed to heterogeneous waste. No such behaviors would be captured by the models presented here.

Figure 4.2.2 shows the temperature profiles from MIT validation probe runs (except MIT thermocouples in AW-101) on the dates given. Figure 4.2.3 gives the convective layer density profiles obtained with the ball rheometer and indicates the nonconvective densities from core samples, updated with most current available data. Figures 4.2.4 through 4.2.8 provide the apparent viscosity and yield stress in the nonconvective layer-derived ball rheometer data from the first pass through the waste in each riser.[a] The apparent viscosities were normalized to a uniform ball speed of 0.1 cm/s.

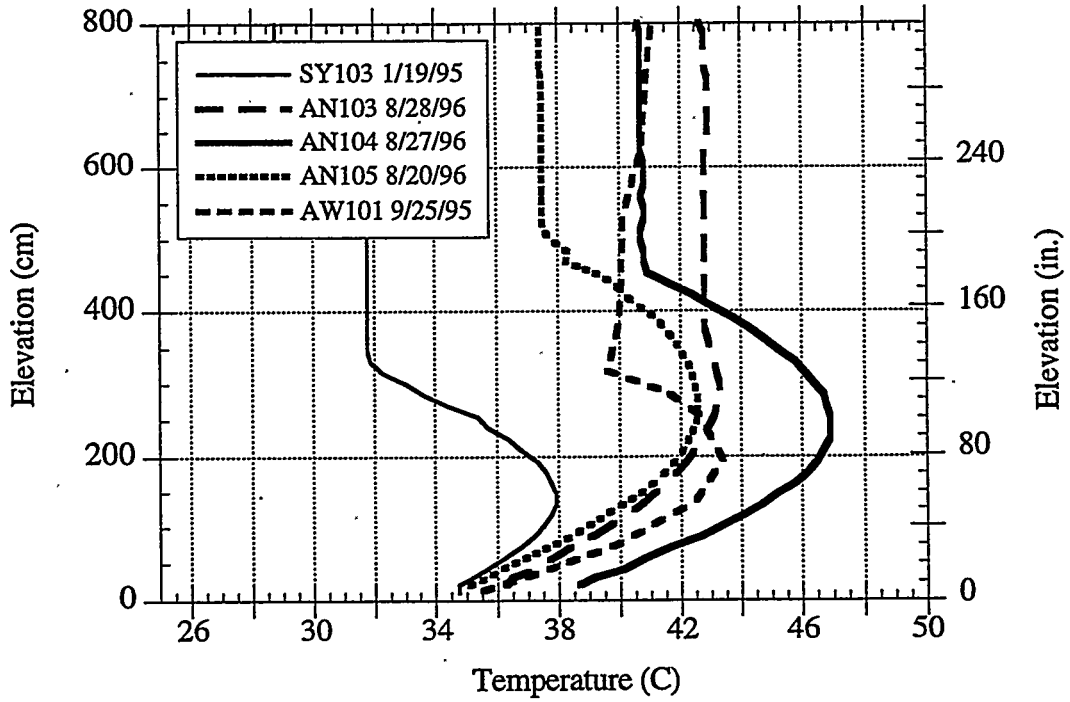

Figure 4.2.2. Temperature Profiles

(a) The apparent viscosity is defined as the ratio of the shear stress divided by the strain rate. It includes the effect of yield stress in a viscoplastic material.

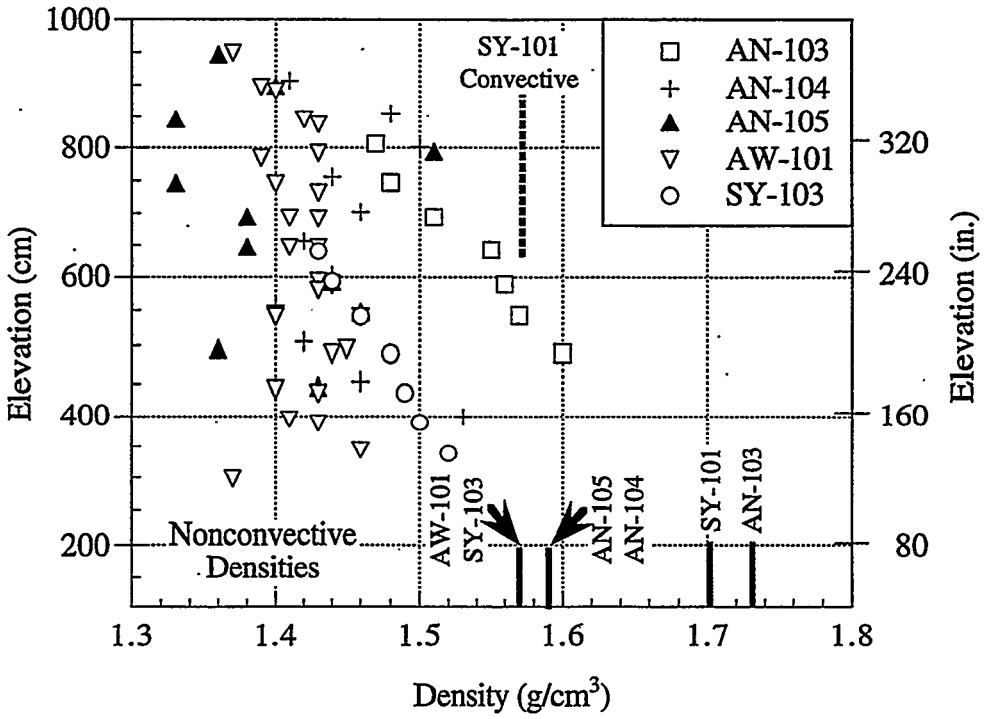

Figure 4.2.3. Density Profiles

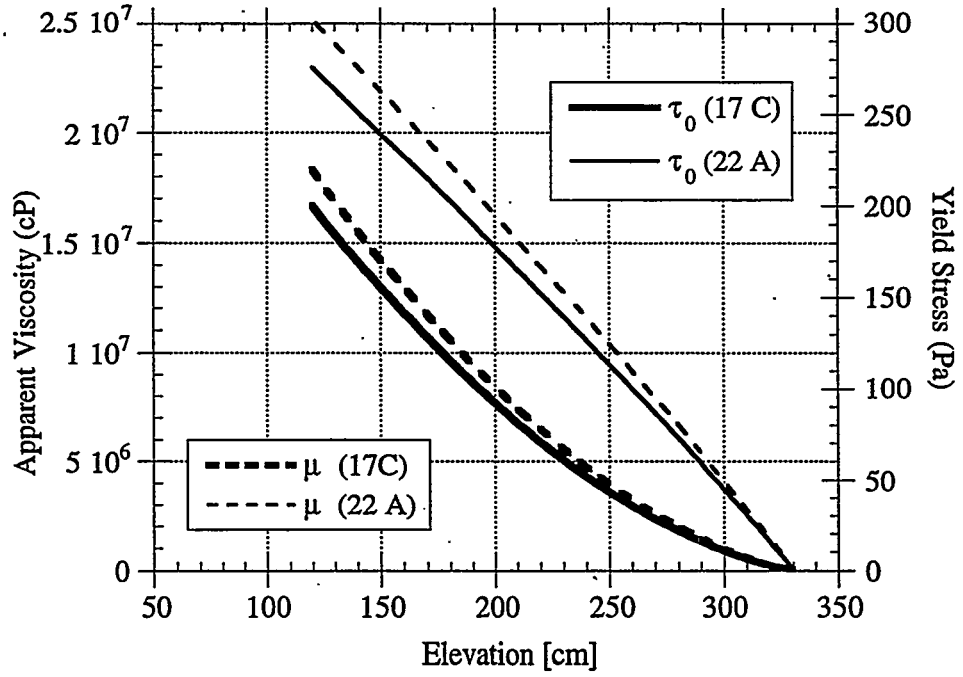

Figure 4.2.4. Apparent Viscosity and Yield Stress: SY-103

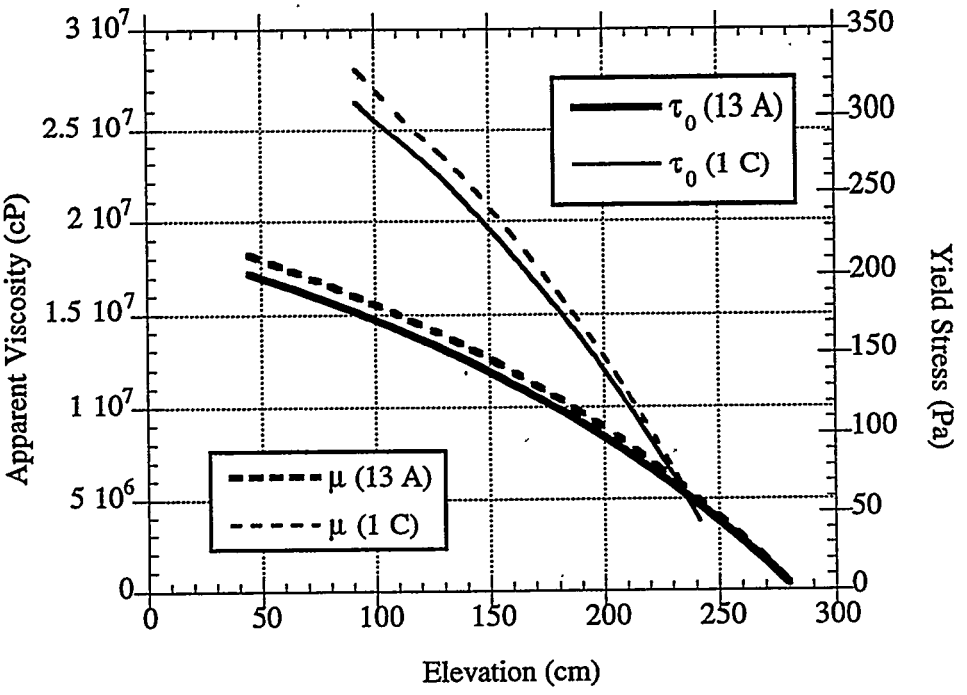

Figure 4.2.5. Apparent Viscosity and Yield Stress: AW-101

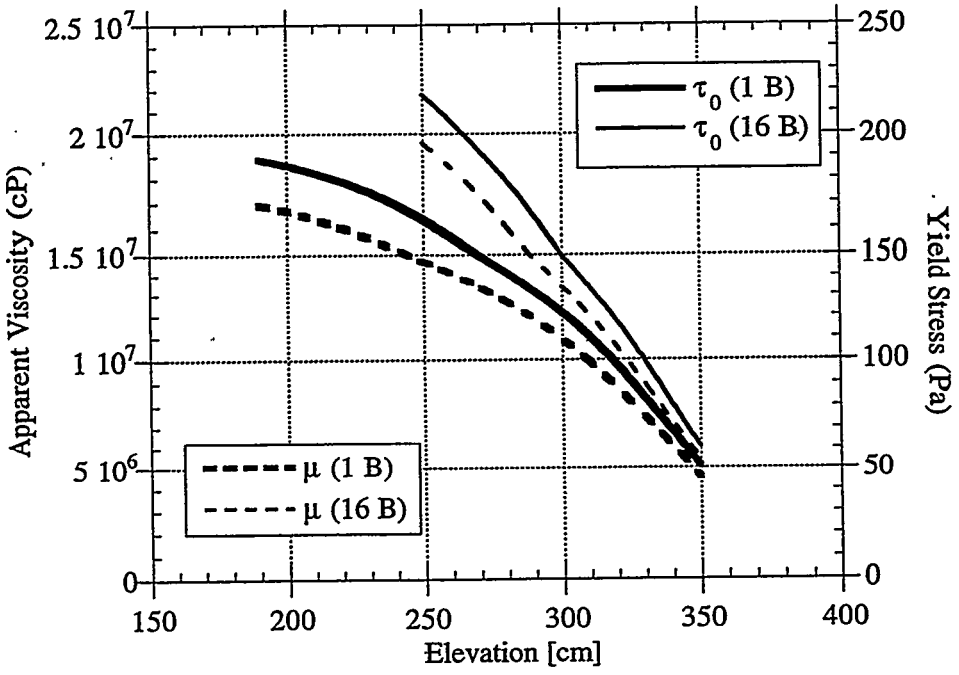

Figure 4.2.6. Apparent Viscosity and Yield Stress: AN-103

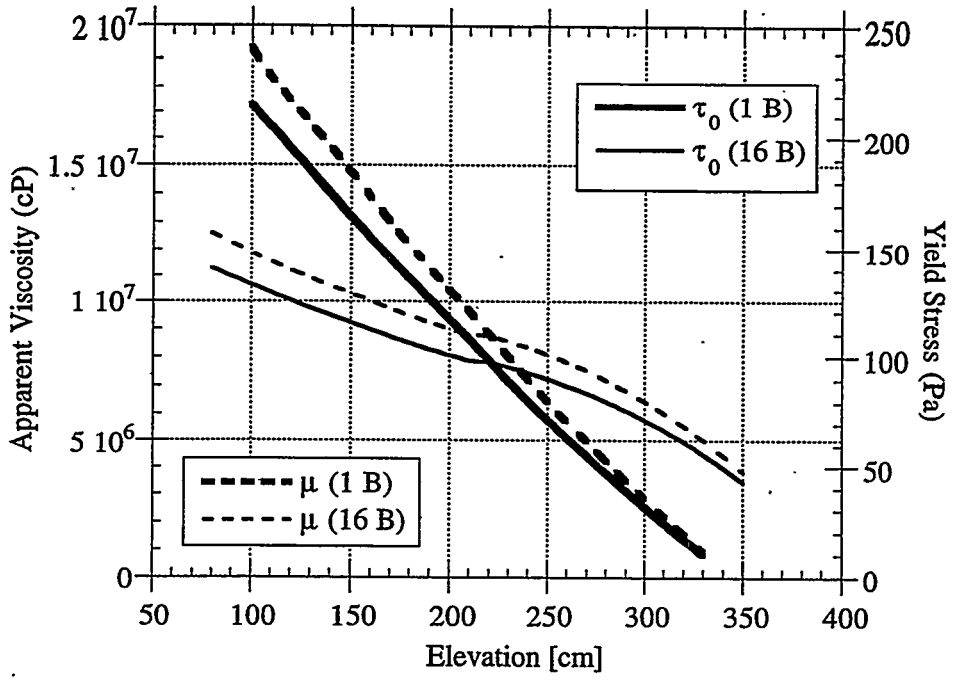

Figure 4.2.7. Apparent Viscosity and Yield Stress: AN-104

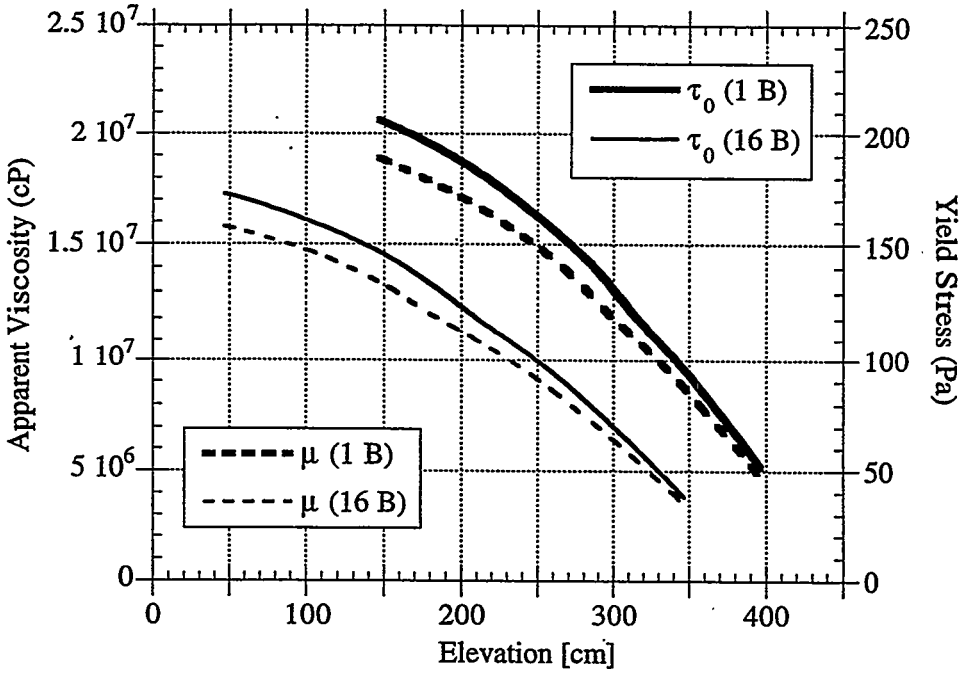

Figure 4.2.8. Apparent Viscosity and Yield Stress: AN-105

Additional information on waste strength is provided by the elevation at which the ball rheometer became supported by the waste. At this point the waste yield stress is at least 900 Pa. The minimum ball elevations in each riser are listed in Table 4.2.1. The yield stress curves in Figures 4.2.4 to 4.2.8 do not extend all the way to the minimum ball elevation because the yield stress cannot be derived from the tension-versus-speed data within several ball diameters of a barrier. The waste properties are apparently discontinuous near where the ball stops, possibly evidence of a hard heel layer.

Table 4.2.2 summarizes the properties and pertinent data used in the models derived in the balance of this section. The following describes the sources of each row of data in the table. In all cases, values given for SY-101 are intended to represent conditions before the mixer pump was installed. Sources for SY-101 data are given at the end of each paragraph.

Densities (Rows 1 and 2): Values are taken directly from Rows 3 and 4 of Table 3.1.2. Densities for SY-101 are taken from Reynolds (1993).

Layer Thickness (Rows 3 - 7): Data for the main layer thicknesses, Rows 3 - 5, are taken directly from Table 3.1.2, Rows 1, 10, and 5, respectively. The "stationary layer" (Row 6) is the average elevation at which the ball rheometer stopped from Table 4.2.1 above. The uncertainty is assigned as half the difference between the two values. Material that would stop the ball has a yield stress greater 900 Pa and, we assume, does not participate in buoyant displacements. Therefore, the effective nonconvective layer depth (Row 7) is the difference between Rows 5 and 6. This configuration is shown schematically in Figure 4.2.9. The SY-101 waste level (Row 3) and nonconvective layer thickness (Row 5) are derived from temperature profiles in Antoniak (1993). Since the temperature data show the larger GREs affecting the lowest thermocouples, the "stationary layer" is assumed to be absent in SY-101, even though neither the ball nor the VFI reached the tank bottom in riser 11B.

Void Fractions (Rows 8 and 9): The neutral buoyancy void fraction (Row 8) is computed from the densities (Rows 1 and 2) by

$$\alpha_{NB} = 1 - \frac{\rho_{CL}}{\rho_{NCL}}$$

Table 4.2.1 Minimum Ball Elevation

Tank	Riser #1	Min. Elevation (cm)	Riser #2	Min. Elevation (cm)
SY-101	11B	80	4A	0
SY-103	17C	102	22A	105
AW-101	13A	0	1C	94
AN-103	16B	227	1B	158
AN-104	16B	74	1B	65
AN-105	16B	0	1B	115

Table 4.2.2. Properties and Parameters Used in Models

Property/Parameter	AN-103	AN-104	AN-105	AW-101	SY-101	SY-103
Densities (kg/m^3)						
1. Convective Layer	1530 ± 50	1440 ± 30	1430 ± 30	1430 ± 30	1500 ± 70	1470 ± 30
2. Nonconvective Layer	1730 ± 110	1590 ± 60	1590 ± 40	1570 ± 30	1700 ± 50	1570 ± 50
Layer Thickness (cm)						
3. Waste Level	884 ± 5	979 ± 4	1041 ± 7	1040 ± 7	1054 ± 10	691 ± 3
4. Convective Layer	413 ± 16	524 ± 10	559 ± 11	693 ± 19	470 ± 8	337 ± 19
5. Nonconvective Layer	379 ± 9	415 ± 9	452 ± 11	283 ± 22	584 ± 40	334 ± 25
6. Stationary Layer	192 ± 35	69 ± 45	57 ± 55	57 ± 47	0	103 ± 20
7. Eff. Nonconvective Layer	187 ± 36	345 ± 10	395 ± 56	225 ± 52	584 ± 40	231 ± 25
Void Fractions (%)						
8. Neutral Buoyancy	12 ± 6	9 ± 4	10 ± 3	9 ± 3	12 ± 5	6 ± 4
9. Nonconvective Layer Avg.	10.7±1.0	6.2±0.9	4.2±0.8	3.8±0.6	~8	6±2
Pressure Ratio						
10. Nonconvective Layer	1.87±0.03	1.97±0.03	2.09±0.04	2.11±0.04	2.30±0.10	1.69±0.05
Nonconvective Layer Rheology						
11. Yield Stress (Pa)	142 ± 15	81 ± 11	129 ± 31	159 ± 37	225 ± 100	112 ± 40
12. Viscosity (Pa-s)	12,600 ± 1400	7,600 ± 650	11,600 ± 2,800	14,000 ± 3500	20,500 ± 10,000	10,400 ± 3900
Historical GRE Data						
13. Std. Rel. Volume (m^3)	14 ± 4	23 ± 16	26 ± 11	14 ± 10	131 ± 47	13 ± 6
14. Period (days)	160 ± 120	120 ± 90	160 ± 130	190 ± 190	100 ± 24	90 ± 70
15. Level Rise (cm/day)	0.04±0.02	0.03±0.01	0.03±0.02	0.03±0.004	0.24±0.06	0.05±0.03

The nonconvective layer void fraction (Row 9) is taken from Table 3.1.2, Row 6. The void fraction in SY-101 is estimated from the nonconvective layer depth and the degassed level from the last row of Table 3.1.2 as follows:

$$\alpha_{SY101} = \frac{\text{Avg. Pre-GRE Gas Vol.}}{\text{Total NCL Volume}} = \frac{L_{Pre-GRE} - L_{NOGAS}}{L_{NCL}}$$

where $L_{Pre\text{-}GRE}$ and L_{NCL} are taken from Rows 3 and 5 of Table 4.2.2, respectively.

Pressure Ratio (Row 10): The nonconvective layer pressure ratio (Row 10) is taken from Table 3.1.2, Row 8. The nonconvective layer pressure ratio for SY-101 is calculated from the densities at the midpoint of the nonconvective layer, ignoring the temperature correction.

Nonconvective Layer Rheology (Row 11 and 12): The nonconvective layer yield stress (Row 11) and apparent viscosity (Row 12) for each tank are calculated as the averages of the values for the two risers plotted in Figures 4.2.4 through 4.2.8, at the elevation of the midpoint of the effective nonconvective layer (thickness given in Row 7). The elevation is calculated by

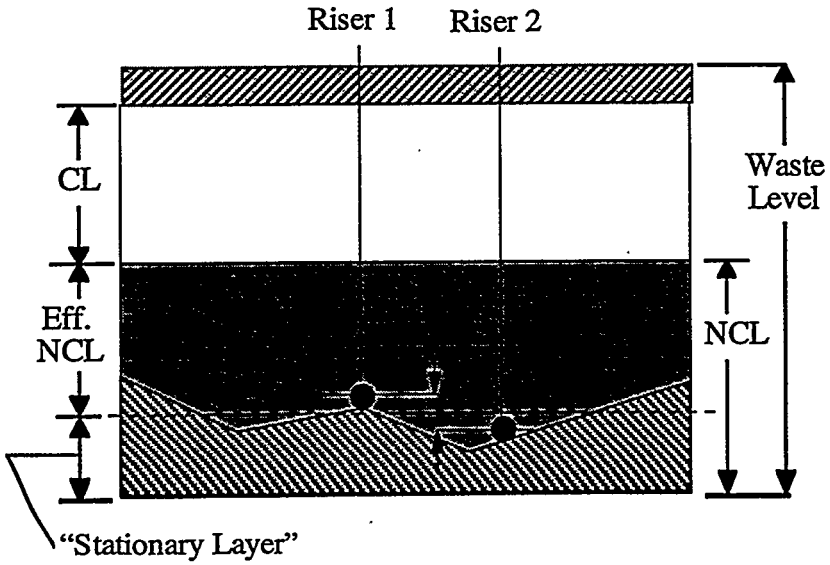

Figure 4.2.9. Layer Thickness Measurements

Eff. NCL Elev. = 0.5*{Eff. NCL Layer (Row 7)} + {"Stationary Layer" (Row 6)}

The apparent viscosity given for any tank should be viewed as more of an indicator of tank-to-tank differences than a physical property. It is highly dependent on the strain rate, and it is unclear what strain rate would be most important in the initiation of a buoyant displacement. Yield stress and viscosity for the nonconvective layer in pre-mixer pump SY-101 are not known but are assumed to have the same general dependence on height as in SY-103. Since the nonconvective layer in SY-101 was much thicker than that in SY-103, the midpoint of the effective nonconvective layer also would have been significantly higher. Since data for all the DSTs show viscosity and yield stress increasing with depth, we used the lowest depth data from SY-103 to represent the midpoint value for SY-101.

Historic GRE Data (Rows 13–14): The GRE standard volume (Row 13) and GRE period (Row 14) are taken from Table 4.2.1. The level rise rate (Row 15) is a direct measure of the gas retention rate, which, in part, determines the GRE period. It is determined from the linear slope of the waste level history prior to GREs shown in Section 4.1 (e.g., Figures 4.1.1 and 4.1.3).

4.3 Material Strength Effects on Initial Buoyancy

A buoyant displacement can occur when a portion of the nonconvective layer becomes less dense than the liquid layer above. However, the strength of the material, which enables it to accumulate gas, restrains the system and requires somewhat more buoyancy to initiate the event. This section examines the effects of material strength on initial buoyancy. In Section 4.3.1, the buoyancy of a planar layer of nonconvective material extending to the tank walls is analyzed. Section 4.3.2 analyzes three-dimensional gobs. The stabilizing effect of material strength is demonstrated and quantified in each section.

4.3.1 Buoyancy of Plane Layers

Consider a plane layer of nonconvective material that behaves like a viscoplastic material and has a uniform bulk density, ρ_B. Neglecting the density of stored gas with respect to that of the solid-liquid mixture, ρ_S, the layer bulk density can be expressed as

$$\rho_B = (1-\alpha)\rho_S \tag{4.3.1}$$

where α is the gas volume fraction. The supernatant liquid or convective layer can be regarded as a Newtonian fluid of uniform density, ρ_L. A portion of the nonconvective layer will experience a buoyant force proportional to the difference in densities between the fluid surrounding that region (of density ρ_L) and the region that retains gas (of density ρ_B). When there is a net positive (upward) buoyant force, the strength of the nonconvective material will restrain the layer until the normal stress difference exceeds the yield stress. Up to the point of yielding, the local normal stress, σ (due to buoyancy), will satisfy the equilibrium equation for normal stresses (Fung 1994):

$$\frac{d\sigma}{dz} + (\rho_L - \rho_B)\, g = 0 \tag{4.3.2}$$

At the convective/nonconvective layer interface ($z = h_S$, where h_S is the height of the nonconvective layer), the normal stress is zero. The normal stress difference between any two elevations within the nonconvective layer is obtained by integrating Eq. (4.3.2) between z_1 and z_2:

$$\sigma_1 - \sigma_2 = g\left[\rho_L(z_2 - z_1) - \int_{z_1}^{z_2} \rho_B \, dz\right] \tag{4.3.3}$$

At the onset of a buoyant instability, the portion of the nonconvective layer that is about to yield is experiencing a normal stress that tends to pull the layer apart. The yield stress obtained from ball rheometer data is an estimate of how the sludge will fail in shear. The relationship between the yield stress in shear, τ_y, and that in tension, σ_y, is $\sigma_y = \sqrt{3}\,\tau_y$. This result can be derived from the state of stress in a viscoplastic material undergoing an elongational flow (Macosko 1994) or, alternatively, from the von Mises yield criterion for isotropic plastic solids. The material could yield from a combination of tension and shear, in which case the stress at yielding is $\beta\tau_y$ $(1 \le \beta \le \sqrt{3})$.

The average yield stress in shear between two points, z_1 and z_2, is determined from

$$\bar{\tau}_y = \frac{\beta}{(z_2 - z_1)} \int_{z_1}^{z_2} \tau_y(z)\, dz \tag{4.3.4}$$

where the local yield stress is obtained from ball rheometer data, for example. Define the average bulk density as a function of the average void fraction in accordance with Eq. (4.3.1) as

$$\overline{\rho}_B = (1-\overline{\alpha})\rho_S = \frac{\rho_S}{(z_2 - z_1)} \int_{z_1}^{z_2} [1-\alpha(z)]dz \qquad (4.3.5)$$

Immediately prior to a buoyant displacement, the upward force due to buoyancy and restraining force due to stress in the material are exactly in balance. The average void fraction required to attain this condition can be termed the critical void fraction. Combining Eq. (4.3.3), (4.3.4), and (4.3.5), and integrating over the entire depth of the nonconvective layer ($z_1 = 0$) and the top ($z_2 = H$), we can express this force balance as

$$\rho_S g H \left[\overline{\alpha}_C - \alpha_{NB}\right] = \beta \overline{\tau}_y \qquad (4.3.6)$$

where α_{NB} is the neutral buoyancy void fraction given by

$$\alpha_{NB} = 1 - \frac{\rho_L}{\rho_S} \qquad (4.3.7)$$

Solving Eq. (4.3.6) for the critical void fraction, we have

$$\overline{\alpha}_C = \alpha_{NB} + \frac{\beta \overline{\tau}_y}{\rho_S g H} \qquad (4.3.8)$$

In the case of zero yield stress, the neutral buoyancy void fraction is the stability threshold. A non-zero yield stress stabilizes the layer by requiring a higher void fraction to initiate a buoyant displacement. For simplicity, we will drop overbars on α_c and τ_y, and it will be understood that they represent averaged values.

Table 4.3.1 compares the measured void fraction at which buoyant displacement began in Gauglitz's small-scale experiments (Stewart et al. 1996b) with the critical void fraction calculated from Eq. (4.3.8). These tests used bentonite clay (less than 5 cm thick) under a supernatant water layer (10 cm thick). Gas was generated by decomposition of hydrogen peroxide (see Section 5). Here, the value of H is the entire depth of the clay layer. The calculated critical void fractions are in good agreement with the measured ones. The large critical void fraction compared with neutral buoyancy illustrates the stabilizing influence of material strength. The effect is relatively large due to the shallowness of the sludge layer in the experiments. Some of the increased buoyancy can be attributed to wall effects, which can be important in small vessels.

The results obtained by applying Eq. (4.3.8) with $\beta = 1$ to DSTs are shown in Table 4.3.2. The tank parameters are taken from Table 4.2.2. The value of H is taken to be the effective

Table 4.3.1. Comparison of Experimental and Calculated Critical Void Fractions

H [cm]	ρ_S [Kg/m^3]	τ_y [Pa]	α_{NB} Eq. (4.3.7)	α_c Measured	α_c ($\beta = 1$) Eq. (4.3.8)	α_c ($\beta = 3^{1/2}$) Eq. (4.3.8)
4.7	1087	67	0.08	0.25	0.21	0.31
4.8	1070	14	0.07	0.15	0.10	0.12
1.5	1070	14	0.07	0.19	0.15	0.22

Table 4.3.2. Critical Void Fraction for Buoyant Displacement in DSTs

Tank	H [cm]	ρ_s [kg/m^3]	τ_y [Pa]	α_{NB} Eq. (4.3.7)	α_c ($\beta = 1$) Eq. (4.3.8)	α_{NB} Measured
AN-103	204	1730	170	0.116	0.121	0.122
AN-104	383	1590	100	0.094	0.096	0.062
AN-105	397	1590	110	0.101	0.103	0.042
AW-101	228	1570	140	0.089	0.094	0.038
SY-101	544	1700	140	0.118	0.119	0.08
SY-103	207	1570	140	0.064	0.068	0.06

nonconvective layer depth. In full-tank dimensions, the stabilizing influence of material strength on a plane layer is much less than in a small vessel, as shown by the close correspondence of the neutral buoyancy void fraction to the critical value.

4.3.2 Effect of Geometry on Buoyant Gobs

In the discussion above, the volume of nonconvective material participating in a buoyant displacement was treated as a planar layer extending to the tank walls. While this analysis shows that material yield strength has an important stabilizing effect on plane layers, it is almost certain that actual buoyant displacements occur in regions much smaller than the tank diameter. Therefore, stresses on the sides of the participating gob, in addition to those on the bottom, need to be considered.

To examine the effect of gob shape, consider a force balance on a gob of volume, V_0, with wetted surface area, S_0. The wetted surface area does not include the top of the gob, which is assumed to be in contact with the liquid layer and therefore to be under zero stress. Assuming constant properties, the buoyant force on the gob is $[\rho_L - \rho_S(1-\alpha_C)]gV_0$, and the net restraining force on the surface of the gob is $\beta\tau_y S_0$. The parameter β now accounts for all averaging of shear and tensile stresses over the surface of the gob. Equating these two forces and using Eq. (4.3.1) and (4.3.7) results in

$$\frac{\rho_B}{\rho_L} = \frac{1-\alpha_C}{1-\alpha_{NB}} = 1 - \frac{\beta\tau_y k_g}{\rho_L g} \tag{4.3.9}$$

where k_g is the ratio of the wetted surface area (or more precisely, that part of the surface area of the gob that was in contact with the rest of the gas-retaining layer immediately prior to initiation of the buoyant displacement) to the volume of the gob. That is,

$$k_g = \frac{S_0}{V_0} = k_g(D_0) \tag{4.3.10}$$

The surface-to-volume ratio is a function of the gob diameter, D_0, that depends on the shape. A family of shapes for which k_g is proportional to the inverse of D_0 can be obtained by scaling a single shape uniformly in all directions:

$$k_g = \frac{b}{D_0} \tag{4.3.11}$$

In particular,

- for a hemisphere of diameter D_0: $b = 6$
- for a cube with edge D_0: $b = 5$
- for a box with edges D_0, a D_0, c D_0: $b = (2 + 2/a + 1/c)$.

A family of shapes with a slightly more complicated formula for k_g is the family of right cylinders of uniform depth and similar base. Let the area of the base be $A = qD_0^2$ and the perimeter be $P = pD_0$. Then the surface area is given by

$$S_0 = PH + A = pHD_0 + qD_0^2 \tag{4.3.12}$$

$$V_0 = qHD_0^2 \tag{4.3.13}$$

hence

$$k_g = b/D_0 + 1/H \tag{4.3.14}$$

where $b = p/q$. For a cylinder, $b = 4$. In the limit of a thin vertical slab in Case 3 above, where a and c tend to infinity, b tends to a minimum value of 2. We propose that the value of b be no smaller than 2 and—for the most probable shapes—between 4 and 6.

To examine the effect of gob diameter on the critical void fraction, consider a cylindrical gob geometry. Calculated critical void fraction is shown in Table 4.3.3 for AN-105. The diameter is specified, and the gob height, H, is taken to be the effective nonconvective layer height. We see from the results that, for larger gobs, yield stress has a negligible effect on the critical void fraction. However, as the gob becomes smaller, the void fraction increases significantly. Results for hemispherical gobs indicate similar behavior.

In summary, nonconvective material yield strength can stabilize otherwise buoyant material. The magnitude of the effect depends on the shape of the gob as well as the size. The shape effect depends on the ratio of the surface area to the volume. For large gobs, the criterion for a buoyant displacement to occur is approximately $\alpha_c = \alpha_{NB}$ or, equivalently, $\rho_B = \rho_L$. For smaller gobs, the critical void fraction is greater than the neutral buoyancy void fraction and must be calculated based on the gob shape.

Table 4.3.3. Calculated Critical Void Fractions for Tank AN-105

Gob Diameter (m)	1	2	4	8	12
Critical void fraction (%)	13.1	11.7	10.9	10.6	10.5
$\alpha_{NB} = 10.1\%$					

4.4 Stability of Buoyant Nonconvective Layers

The purpose of this section is to examine the stability of the buoyant nonconvective layer to develop a relationship between gob size and initial buoyancy. In the previous section, gob size

was related to initial buoyancy based on static force balance arguments. With two such relations, both gob size and critical void fraction can be solved to predict the gas release volumes and their period for given conditions.

At the onset of a buoyant displacement, the yield strength of the nonconvective material is exceeded, and a region within the layer begins to flow. Assuming that at this point the entire nonconvective layer behaves as a viscous fluid, the length scale of the initial buoyant displacement can be estimated from the Rayleigh-Taylor theory for superposed fluid layers of different densities and viscosities. The length scale is taken to be the characteristic length of a region of fluid that at one instant moves either upward or downward. Thus the length scale is half the wave length of the disturbance that has the largest growth rate. If the length scale remains approximately constant as the disturbance grows, then it becomes the effective diameter of a buoyant gob participating in buoyant displacement.

The analysis presented here is a highly idealized treatment of the complex conditions existing in the DSTs. It assumes uniform fluid properties and Newtonian rheology. Additionally, the effects of boundaries such as tank walls and floor and the free surface of the supernatant layer are ignored. In spite of these limitations, the analysis introduces some dependencies between gob size and waste properties that are physically based. Models based on the results of this analysis will be shown to produce good agreement with the historical data in spite of the limitations of the approach. The assumptions, limitations, and general applicability of the analysis are discussed in more detail at the end of Section 4.4.1.

4.4.1 Rayleigh-Taylor Stability Analysis

Consider a viscous Newtonian fluid of density, ρ_L, and kinematic viscosity, ν_L, overlying a lighter fluid (the buoyant nonconvective layer) of density, ρ_B, and kinematic viscosity, ν_B. The relationship between wave number ($k = 2\pi/\lambda$, where λ is the wavelength) and growth rate of the disturbance n is referred to as the dispersion relation and is obtained by performing a stability analysis on the governing differential equations of hydrodynamics. If the two layers of fluid have infinite extent (i.e., no wall boundary effects), the dispersion relation can be obtained in analytic form. As long as the disturbances are relatively small compared with the tank diameter and nonconvective layer depth, this solution will be valid. For larger disturbances, however, the solution will be only approximately correct since the boundary conditions are violated. The general applicability of this analysis for large disturbances will be addressed in more detail at the end of this section. The dispersion relation is given by Chandrasekhar (1981):

$$
\begin{aligned}
&-\left[\frac{gk}{n^2}(\alpha_B-\alpha_L)+1\right](\alpha_L q_B+\alpha_B q_L-k)-4k\alpha_B\alpha_L+\\
&+\frac{4k^2}{n}(\alpha_B\nu_B-\alpha_L\nu_L)\left[(\alpha_L q_B-\alpha_B q_L)+k(\alpha_B-\alpha_L)\right]+\\
&+\frac{4k^3}{n^2}(\alpha_B\nu_B-\alpha_L\nu_L)^2(q_B-k)(q_L-k)=0
\end{aligned}
\qquad (4.4.1)
$$

where

$$
\alpha_B=\frac{\rho_B}{\rho_B+\rho_L} \qquad q_B=\sqrt{k^2+\frac{n}{\nu_B}}
$$

$$
\alpha_L=\frac{\rho_L}{\rho_B+\rho_L} \qquad q_L=\sqrt{k^2+\frac{n}{\nu_L}}
$$

The subscript B refers to the gas-retaining nonconvective layer, and index L is the supernatant liquid or convective layer. Note that the parameter α does not refer to a physical void fraction here. There is, however a functional relationship between the parameters α_B and α_L and the void fractions α_C and α_{NB}. Specifically,

$$\alpha_L = \frac{1-\alpha_{NB}}{(1-\alpha_C)+(1-\alpha_{NB})}$$
$$\alpha_B = \frac{1-\alpha_C}{(1-\alpha_C)+(1-\alpha_{NB})} \qquad (4.4.2)$$

We nondimensionalize the dispersion relation as follows. The characteristic length and time scales are

$$d^3 = \frac{8\nu_B^2\alpha_B^2}{g}$$
$$\tau = \frac{d^2}{\nu_B} \qquad (4.4.3)$$

We introduce the following dimensionless groups:

$$\tilde{k} = dk$$
$$\tilde{n} = \tau n \qquad (4.4.4)$$
$$\varepsilon^2 = \frac{\nu_L}{\nu_B}$$

With this nondimensionalization, the dispersion relation Eq. (4.4.1) becomes

$$-\left[\frac{8\tilde{k}\alpha_B^2}{\tilde{n}^2}(\alpha_B-\alpha_L)+1\right]\left(\varepsilon\alpha_L\tilde{q}_B+\alpha_B\tilde{q}_L-\varepsilon\tilde{k}\right)-4\varepsilon\tilde{k}\alpha_B\alpha_L+$$
$$+\frac{4\tilde{k}^2}{\tilde{n}}(\alpha_B-\varepsilon^2\alpha_L)\left[(\varepsilon\alpha_L\tilde{q}_B-\alpha_B\tilde{q}_L)+\varepsilon\tilde{k}(\alpha_B-\alpha_L)\right]+ \qquad (4.4.5)$$
$$+\frac{4\tilde{k}^3}{\tilde{n}^2}(\alpha_B-\varepsilon^2\alpha_L)^2\left(\tilde{q}_B-\tilde{k}\right)\left(\tilde{q}_L-\varepsilon\tilde{k}\right)=0$$

where

$$\tilde{q}_B = \sqrt{\tilde{k}^2+\tilde{n}}$$
$$\tilde{q}_L = \sqrt{\varepsilon^2\tilde{k}^2+\tilde{n}}$$

The actual value of ε is about 0.01. In the inviscid limit $\varepsilon = 0$, the dispersion relation Eq. (4.4.5) becomes

$$-8\tilde{k}\alpha_B^2(\alpha_B - \alpha_L) - \tilde{n}^2 - 4\tilde{k}^2\tilde{n}\alpha_B + 4\tilde{k}^3\alpha_B(\tilde{q}_B - \tilde{k}) = 0 \tag{4.4.6}$$

Now consider the limit of $\alpha_L - \alpha_B << 1$. Define $\delta = \alpha_L - \alpha_B$ so that Eq. (4.4.6) becomes

$$2\delta(1-\delta)^2\tilde{k} - \tilde{n}^2 - 2(1-\delta)\tilde{k}^2\tilde{n} + 2(1-\delta)\tilde{k}^3(\tilde{q}_B - \tilde{k}) = 0 \tag{4.4.7}$$

A dominant balance occurs for $\delta << 1$ when

$$\tilde{k} = O(\delta^{1/3})$$
$$\tilde{n} = O(\delta^{2/3})$$

Thus let

$$\tilde{k} = \delta^{1/3}K$$
$$\tilde{n} = \delta^{2/3}N \tag{4.4.8}$$

Then the dispersion relation becomes (to leading order)

$$K - N^2 - 2K^2N + 2K^3(Q_B - K) = 0 \tag{4.4.9}$$

where

$$Q_B = \sqrt{K^2 + N}$$

This equation is not solvable analytically but is easily solved numerically. There is a unique value of N for each positive value of K. The value of K giving the maximum value of N is K~1. This corresponds to the most unstable disturbance. The values observed in the numerical solution of the exact dispersion relation, Eq. (4.4.6), are in the range of $1.0 \le K \le 1.02$ for $0 \le \delta \le 0.06$. This is consistent with the approximation being correct to $O(\delta)$ and $O(\varepsilon)$.

Now, if we take the approximate solution to Eq. (4.4.9) to be $K = c_1 \approx 1$, we can solve for the most unstable disturbance wavenumber, k_{max}. Using the definitions given by Eq. (4.4.8), (4.4.4), and (4.4.3), we have

$$k_{max} = \frac{2\pi}{\lambda_{max}} = \frac{c_1}{2}\left[\frac{g(\rho_L^2 - \rho_B^2)}{\mu_B^2}\right]^{1/3} \tag{4.4.10}$$

Eq. (4.4.10) gives the most unstable disturbance wavenumber for the stratified layer. The wavenumber, or wavelength, depends on the viscosity of the bulk layer, the difference in the squares of the densities of the two layers, and the gravitational constant.

Now if we take the diameter of the gob as one half the wavelength of the most unstable disturbance, we have

$$D_0 = \frac{2\pi}{c_1}\left[\frac{\mu_B^2}{g\left(\rho_L^2 - \rho_B^2\right)}\right]^{1/3} \qquad (4.4.11)$$

Several points need to be made regarding the general applicability of Eq. (4.4.11). First of all, Eq. (4.4.11) predicts the diameter of the most unstable gob; however, larger and smaller gobs are also unstable and may occur with lower probability.

The second point relates to the shape of disturbances. The stability analysis assumed longitudinal disturbances at the interface between the convective and nonconvective layers. In reality, disturbances are likely to be more cylindrical. Based on similarity arguments, one can show that the solution for wavenumber for cylindrical disturbances has the same functional form as Eq. (4.4.10). The only difference would be the constant multiplier, c_1. Therefore, D_0 can be assumed to be the effective diameter of a gob with cylindrical symmetry if the constant c_1 is adjusted appropriately.

The third point relates to boundary conditions. The stability analysis is for a doubly infinite stratified layer. The presence of tank walls, tank floor, and supernatant liquid free surface all violate the boundary conditions of the analysis. If disturbances are found to be small compared with tank length scales (i.e., diameter, nonconvective or convective layer height), the effects of the violation should be negligible. If disturbances are predicted to be very large compared with the tank length scales, the assumptions are severely violated and the analysis does not hold. If the disturbances are comparable to tank length scales, however, the analysis may still hold approximately. The primary functional dependence of wavelength on viscosity and density difference might still be the dominant controlling factor. If the stability analysis were performed for the bounded case (a difficult analysis) one would most likely find that the wavelength has additional functional dependencies on tank diameter and waste levels. The predicted disturbance wavelengths have similar magnitudes for all cases considered. Given that all tank diameters are the same, and nonconvective layer depths do not vary by large factors, we suspect that the dependencies on the additional length scales are approximately the same for each tank considered. This point, of course, cannot be proven without completing the analysis with the correct boundary conditions.

The final point relates to waste properties. While convective layer densities are nearly uniform, nonconvective layer densities vary with depth. Nonconvective layer viscosities and yield stresses also vary strongly with depth (Figures 4.2.4–4.2.8). However, if predicted gob diameters are large compared with regions of vertical property variation, the effects of the variation should be minimal. Waste properties are also seen to vary depending on the riser used for the sample or test. Additionally, nonconvective layer viscosities are strongly shear-rate dependent and are clearly non-Newtonian. Hence, the nonuniform, non-Newtonian waste properties clearly violate the assumptions of the stability analysis. Consistent with our overall modeling approach, however, we simplify by using mean or average properties in the models.

In spite of its limitations and idealizations, the stability analysis does provide a simple, physically based relationship between gob size and average waste properties. To quantify the limitations of the approach, a rigorous analysis that accounts for three-dimensional disturbances, tank boundaries, and nonuniform/non-Newtonian properties would be required. Such an analysis would be an enormous undertaking and is likely intractable. Our hope is that the simplistic stability analysis has captured the most dominant functional dependence of gob size on waste properties. The degree to which the model predicts the historical tank behavior is one test of its merits (and is the only one currently available). Additional testing is desirable to refine the model and verify its predictive capability.

4.4.2 Gob Size and Critical Void Fraction

The diameter of the most unstable gob is given by Eq. (4.4.11) as a function of the viscosity and bulk density of the nonconvective layer and the supernatant liquid. Eq. (4.3.9) provides an additional relation between gob diameter and waste properties. These two relations can be combined to solve for the gob diameter and the critical void fraction independently. Returning to Eq. (4.3.9) and rearranging it gives

$$1-\frac{\rho_B}{\rho_L}=\frac{\beta\bar{\tau}}{\rho_L g}k_g(D_0) \tag{4.4.12}$$

Also, using the assumption that the density difference is small, we have

$$\rho_L^2-\rho_B^2=\rho_L^2\left(1-\frac{\rho_B^2}{\rho_L^2}\right)\approx\frac{2\rho_L\beta\bar{\tau}}{g}k_g(D_0) \tag{4.4.13}$$

Substituting Eq. (4.4.13) into Eq. (4.4.11) we obtain

$$D_0=\frac{2\pi}{c_1}\left[\frac{\mu_B^2}{2\rho_L\beta\bar{\tau}k_g(D)}\right]^{1/3} \tag{4.4.14}$$

To solve for D_0 we rewrite (4.4.14) as

$$D_0{}^3k_g(D_0)=\frac{4\pi^3\mu_B^2}{c_1^3\rho_L\beta\bar{\tau}}\equiv L_1{}^2 \tag{4.4.15}$$

Note that the grouping L_1 has dimensions of length. This is one natural-length scale of the system under consideration. Once D_0 is solved from Eq. (4.4.14), the critical void fraction can be determined from Eq. (4.3.9) according to

$$\alpha_C=\alpha_{NB}+(1-\alpha_{NB})L_2L_1{}^2/D_0{}^3 \tag{4.4.16}$$

where L_2 is another natural-length scale given by

$$L_2=\beta\bar{\tau}/\rho_L g \tag{4.4.17}$$

In the particular cases discussed in Section 4.3 we have, for the case of similar shapes, where $k_g = b/D_0$

$$D_0{}^3k_g(D_0)=bD_0{}^2=L_1{}^2 \tag{4.4.18}$$

hence

$$D_0=b^{-1/2}L_1 \tag{4.4.19}$$

The maximum value of D_0 occurs when b is its minimum value; b = 2, therefore,

$$D_0\le 2^{-1/2}L_1 \tag{4.4.20}$$

The volume of the gob must be determined according to the applicable formula for each particular shape. For example, in the case of a hemisphere, b = 6, so

$$D_0 = 6^{-1/2} L_1 \tag{4.4.21}$$

and

$$V_0 = \frac{\pi}{12} D_0{}^3 = \frac{\pi}{72\sqrt{6}} L_1{}^3 \tag{4.4.22}$$

The critical void fraction for similar gobs with any value of b is given by

$$\alpha_C = \alpha_{NB} + b(1-\alpha_{NB}) L_2 / D_0 \tag{4.4.23}$$

For the case of right cylinders, $k_g = b/D_0 + 1/H$, so

$$D_0{}^3 k_g(D_0) = \frac{D_0{}^3}{H} + bD_0{}^2 = L_1{}^2 \tag{4.4.24}$$

Letting $x = D_0/H$, we have the cubic equation

$$x^3 + bx^2 - a = 0 \tag{4.4.25}$$

where $a = L_1{}^2/H^2$. The analytic solution to this cubic equation is

$$x = \frac{D_0}{H} = y^{1/3} + \frac{b^2}{9y^{1/3}} - \frac{1}{3}b \tag{4.4.26}$$

where

$$y = \tfrac{1}{2}a - \tfrac{1}{27}b^3 + \tfrac{1}{18}\sqrt{81a^2 - 12ab^3} \tag{4.4.27}$$

There are two significant limiting cases for this formula, corresponding to the dominance of either the third- or second-order term in Eq. (4.4.25). In the first case, x is large compared with b, and $x \sim a^{1/3} >> b$. This parameter regime is identified by the relation $a >> b^3$. The intermediate value y is real-valued in this case. Geometrically, we have a gob of shallow depth. In the second case, where x is small compared with b, $x \sim (a/b)^{1/2} << b$. This parameter regime is identified by the relation $a << b^3$. The intermediate value y is complex in this case, although the solution x is still real and positive. Geometrically we have a gob of narrow width and large depth. In the intermediate parameter regime, when $a = O(b^3)$, all three terms of the polynomial equation are equally important, and the full solution given by Eq. (4.4.26) and (4.4.27) is necessary. The intermediate value y is either real or complex, with a transition when $a = (4/27)b^3$. Geometrically, the gob is of similar width and depth.

Finally, once D_0 is determined from Eq. (4.4.26), the cylindrical gob volume is

$$V_0 = \pi D_0{}^2 H/4 \tag{4.4.28}$$

and the critical void fraction is calculated according to Eq. (4.4.16).

4.5 Predictive Models

The gob volume and critical void fraction have been solved by the analysis of the previous sections. We can now use these key results to develop models that predict the frequency of buoyant displacements and the size of resulting gas release volumes. The models are applied to the six DSTs, and the results are compared with historical data. Finally, an approximate model is presented that gives good results and has a relatively simple analytic form.

4.5.1 Size and Frequency of Gas Release Events

Since we have solved for the gob volume and critical void fraction, the in-situ volume of gas within the gob is known. If the fraction of this gas released during a buoyant displacement can be calculated, the volume of gas actually released can be determined.

The fraction of gas within a gob that is released during a buoyant displacement can be estimated by a simple model. We assume that gas is released until the nonconvective material, which is now near the surface of the waste, returns to neutral buoyancy. After the release, the gob settles back through the supernatant liquid to the nonconvective layer.

Recall the definition of void fraction, $\alpha = V_G/(V_G+V_S)$, where V_S is the gas volume and V_0 is the volume of solids and liquids. By rearranging, the initial gas volume in the gob just prior to buoyant displacement is $V_{G0} = \alpha_C/(1-\alpha_C)V_S$. As the gob rises to the waste surface, the retained gases expand so that the volume of gas within the gob is $V_{G1} = p_S V_{G0}$, where p_S is the average pressure of the gas in the nonconvective layer in atmospheres. After the gas is released, neutral buoyancy at the surface dictates that $V_{G2} = \alpha_{NB}/(1-\alpha_{NB})V_S$. The fraction of the gas in the gob released is $f_{REL} = (V_{G1} - V_{G2})/V_{G1}$. Substituting for V_{G1} and V_{G2}, we find that

$$f_{REL} = 1 - \frac{\alpha_{NB}(1-\alpha_C)}{\alpha_C(1-\alpha_{NB})}\frac{1}{p_S} \tag{4.5.1}$$

The amount of gas released during a GRE (at standard conditions) is therefore

$$V_{REL} = f_{REL}\,\alpha_C V_0 p_S \tag{4.5.2}$$

For right circular cylindrical gobs (b = 4) we have

$$V_{REL} = f_{REL}\alpha_C \frac{\pi}{4} H D_0^2 p_S \tag{4.5.3}$$

where α_C is given by Eq. (4.4.16), and D_0 is given by solution of Eq. (4.4.26).

For hemispherical gobs we have

$$V_{REL} = f_{REL}\alpha_C \frac{\pi}{12} D_0^3 p_S \tag{4.5.4}$$

where α_{crit} is given by Eq. (4.4.23), and D_0 is given by Eq. (4.4.21).

We now propose a simple model for GRE frequency that is a straightforward extension of the concepts developed so far in this study. The model assumes that gas is generated within the nonconvective layer at a constant rate. While some gas is released due to nonepisodic transport, there is a net accumulation until the nonconvective material becomes unstable, at which time a buoyant displacement occurs. Since the average volume of a buoyant displacement is generally significantly less than the total volume of the nonconvective layer, we assume that there are many such gas generation/buoyant displacement processes occurring independently. Gas accumulation rates can be obtained from long-term level rise data. The number of independent buoyant displacement processes occurring in a tank can be estimated from the results discussed in this section.

According to our model, a buoyant displacement will occur when the void fraction in the nonconvective material is equal to the critical void fraction. After a previous buoyant displacement, the volume of gas within the gob increases with time according to

$$V_G(t) = V_G(0) + A_0(1-f_0)\frac{dh}{dt}t \tag{4.5.5}$$

where $V_G(0)$ is the initial volume of gas at time $t = 0$; A_0 is the cross-sectional area of the gob ($A_0 = \pi D_0^2/4$ for a cylindrical or semispherical gob); and dh/dt is the long-term waste level rise rate. The fraction of gas that is released by small, undetected GREs or other mechanisms between major, recorded GREs is f_0.[(a)] Since the initial gas volume is equal to the amount of gas left in the gob after the previous buoyant displacement, we have

$$V_G(0) = (1\text{-}f_{REL})\,\alpha_C V_0 \tag{4.5.6}$$

If we define the time to initiation of a buoyant displacement as t_C, then $V_G(t_C) = \alpha_C V_0$, and Eq. (4.5.5) can be evaluated at t_C to yield

$$\alpha_C V_0 = (1-f_{REL})\alpha_C V_0 + A_0(1-f_0)\frac{dh}{dt}t_C \tag{4.5.7}$$

Solving Eq. (4.5.7) for t_C yields

$$t_C = \frac{V_0}{A_0(1-f_0)}\left(\frac{dh}{dt}\right)^{-1} f_{REL}\alpha_C \tag{4.5.8}$$

Eq. (4.5.8) gives the average time between buoyant displacements for a given gob. For cylindrical gobs, $V_0/A_0 = H$, where H is the height of the gob. For semispherical gobs, $V_0/A_0 = D_0/3$.

The total number of gobs, N_g, that can act independently is equal to V_S/V_0, where $V_S = h_S A_T$ is the total volume of nonconvective material that retains gas. Therefore, we have

$$N_g = HA_T / V_0 \tag{4.5.9}$$

(a) This factor is important since a particular methodology was applied when counting historical GREs. GREs below about 7 m^3 and occurring over periods longer than 24 hours were not counted. Therefore, to accurately compare with historical data, this factor is needed.

Since the gobs are acting independently of one another, the average time between any two GREs will be $T_{REL} = t_C / N_g$ so that

$$T_{REL} = \frac{V_0^2}{A_0 A_T H} \frac{1}{(1-f_0)} \left(\frac{dh}{dt}\right)^{-1} f_{REL} \alpha_C \tag{4.5.10}$$

For cylindrical gobs we have

$$T_{REL} = \frac{\pi D_0^2 H}{4A_T} \frac{1}{(1-f_0)} \left(\frac{dh}{dt}\right)^{-1} f_{REL} \alpha_C \tag{4.5.11}$$

For hemispherical gobs we have

$$T_{REL} = \frac{\pi D_0^4}{36 A_T H} \frac{1}{(1-f_0)} \left(\frac{dh}{dt}\right)^{-1} f_{REL} \alpha_C \tag{4.5.12}$$

The modeling approach presented in this section also allows us to estimate the average amount of gas retained in the nonconvective layer. For a given gob, the void fraction just prior to a buoyant displacement is α_C. The void fraction after buoyant displacement is $(1\text{-}f_{REL})\ \alpha_C$. Since the void fraction increases nearly linearly in time, the average gob void fraction is approximately $(\alpha_C + (1\text{-}f_{REL})\ \alpha_C)/2$, so that we can write

$$\bar{\alpha}_{NC} \approx (2 - f_{REL}) \alpha_C \tag{4.5.13}$$

Eq. (4.5.13) represents the long-term spatial and temporal average for nonconvective layer void fraction. It is the mass balance of gas being generated versus gas released by multiple gobs acting independently.

4.5.2 Evaluation of GRE Model for DSTs

In this section, we evaluate the models' predictions of GRE size and frequency under the conditions corresponding to the FGWL DSTs, and we identify the gob geometry that produces the best predictive agreement with the data. The hemisphere showed poor agreement with the data, and gob diameters were predicted to be larger than the depth of the nonconvective layers—a clear violation of the assumed geometry. However, the form of the hemisphere model is used to develop a simplified model in the next section.

For right circular cylinder gobs (b =4), the gas release volume is given by Eq. (4.5.3). The formulas were evaluated for the parameter values shown in Table 4.2.2. Additionally, the constants c_1 and β were both set equal to their default value of 1. The value for the viscosity used in the formulas was $\mu_B = c_2 \mu$, where μ is the value derived from the ball rheometer data. The ball rheometer instrument produces indicator (as opposed to absolute) values for dynamic viscosity that are known to be strongly shear-rate dependent. The important information for the models presented is not the absolute value of the viscosity but rather how the viscosity varies from tank to tank. The constant c_2 is the sole adjustable parameter in the model and has the same value for each tank. The value $c_2 = 0.077$ gave the best results.

Results are shown in Table 4.5.1. The first four rows in the table show results for intermediate calculations, and the last three rows show comparisons with historical data. Uncertainties in each computed result, F, are calculated by linear combination according to

$$\Delta F = \sqrt{\sum_i \left(\frac{\partial F}{\partial x_i} \Delta x_i \right)^2} \qquad (4.5.14)$$

where Δx_i is the uncertainty in the input values x_i. These uncertainties are shown in Table 4.2.2 along with the mean input values. Uncertainties were evaluated for all inputs except viscosity.

The model predicts gob diameters ranging from 8 to 13 m. The number of gobs is inversely proportional to the gob size. Critical void fractions vary somewhat from tank to tank, with little or no correlation within a tank group. AN-103 and SY-101 have the largest predicted critical void fractions (13%), and SY-103 has the smallest (~7%). The predicted release fraction for each gob varies from 49% for SY-103 to 60% for SY-101.

Row 5 of Table 4.5.1 shows calculated standard gas release volumes. Historical averages are shown in parentheses along with their associated variations. There is remarkable agreement between the calculated and historical values, and the calculated uncertainties are similar to the variability in historical data. To the extent that uncertainties in waste properties are related to temporal or spatial variations, there may be a connection between model uncertainty and historical variability. However, there is no clear evidence of such a relationship. The predicted values for GRE volume are all within about ± 25% of the historical means except for SY-103, where the volume is underpredicted by about 50%.

Wider variation is seen for predicting the GRE period. Uncertainty in the retention rates produce large uncertainties in the predicted period. The large variability in the historical data make comparisons imprecise. All of the historical mean GRE periods fall within the uncertainty range of the predicted periods but, again, the implication of this is not clear.

Table 4.5.1. Buoyant Displacement Model Results

Calculated Value	AN-103	AN-104	AN-105	AW-101	SY-101	SY-103
Gob Diameter (m) Eq. (4.4.26)	8 ± 2	8 ± 1	9 ± 2	9 ± 2	12 ± 6	8 ± 3
Number of gobs Eq. (4.5.9)	8 ± 3	9 ± 3	6 ± 3	7 ± 3	3 ± 3	8 ± 6
Critical Void (%) Eq. (4.4.16)	12 ± 6	10 ± 4	11 ± 3	10 ± 3	12 ± 5	7 ± 4
Release Fraction (%) Eq. (4.5.1)	52 ± 6	52 ± 3	55 ± 5	58 ± 7	59 ± 12	47 ± 10
GRE Std Vol. (m^3) Eq. (4.5.4)	12±7	17 ± 7	32 ± 13	17 ± 8	117 ± 76	7 ± 5
(Historical - Table 4.1.1)	(14 ± 4)	(23 ± 16)	(26 ± 11)	(14 ± 10)	(131 ± 47)	13 ± 6)
GRE Period (days) Eq. (4.5.11)	79 ± 68	139 ± 90	241 ± 198	140 ± 92	103 ± 109	38 ± 42
(Historical - Table 4.1.1)	(160 ± 120)	(120 ± 90)	(160 ± 130)	(220 ± 230)	(100 ± 24)	(90 ± 70)
NCL Avg. Void (%) Eq. (4.5.13)	9 ± 5	7 ± 3	8 ± 2	7 ± 2	9 ± 4	5 ± 3
(VFI/RGS - Table 3.1.2)	(11 ± 1.0)	(6 ± 0.9)	(4 ± 0.8)	(4 ± 0.6)	(~8)	(6 ± 2)

4.5.3 A Simplified Model

The above model for cylindrical gobs produces very good agreement with the historical data for the six DSTs. However, it is cumbersome to apply because Eq. (4.4.26) does not have a simple closed-form solution. We want to find an approximate model that retains the essential features of the exact solution while simplifying the algebra.

The model for hemispherical gobs has a simple analytical form but does not produce acceptable results, since the predicted diameter exceeds the depth of the nonconvective layer. The diameter of the hemispherical gob has a simple analytical form. We attempt to find an approximate model by assuming that predicted diameter is that of a cylindrical gob even though it was not derived under that assumption. Then the volume of a GRE would be given by Eq. (4.5.3), where D_0 is given by Eq. (4.4.21) so that

$$V_{REL} = f_{REL}\alpha_C \frac{\pi}{4\sqrt{6}} H L_1^2 p_S \tag{4.5.15}$$

Eq. (4.5.15) can be simplified further by noting that the critical void fraction is very nearly equal to the neutral buoyant void fraction for the six tanks considered. Therefore, if we let $\alpha_C = \alpha_{NB}$ then $f_{REL} = p_S - 1$ and Eq. (4.5.15) can be written with the aid of Eq. (4.4.15) as

$$V_{REL} \sim (p_S - 1)\alpha_{NB} H\mu^2 / \rho_L \tau_y \tag{4.5.16}$$

To simplify further, we take advantage of the fact that the kinematic viscosity can be related to the yield strength. The methodology for deriving viscosity and yield strength from ball rheometer data is discussed in Stewart et al. (1996a). For very low shear rates, the viscosity is proportional to the yield stress to first order. The constant of proportionality is the ball shear rate. We take advantage of this fact and write $\mu \sim \tau_y$ in Eq. (4.5.16) to obtain

$$V_{REL} \approx 750(p_S - 1)\alpha_{NB} H(\tau_y / \rho_L) \tag{4.5.17}$$

The leading constant in Eq. (4.5.17) was chosen to give the best fit with the data.

Table 4.5.2 compares the GRE volumes predicted by the approximate formula given by Eq. (4.5.17) with those of the full solution and the historical data. The approximate solution does a reasonable job of matching the data; however, it is not as accurate as the full solution, and its uncertainty is higher.

Eq. (4.5.17) can serve as a predictive model for evaluating the propensity for GREs in other tanks. However, caution is strongly advised for three reasons. First, as well-characterized as the six FGWL DSTs are, uncertainties in their waste properties produce significant uncertainties in predicted volume. Uncertainties would be even higher in cases where properties were less well-defined. Second, while the general scaling of Eq. (4.5.17) is probably correct over some range of conditions, the model has not been evaluated for small GREs, which would be of most interest in its application. Third, additional verification against new data is needed to build confidence in the general applicability of the model.

Finally, it is important to emphasize that the model predicts the most probable gob size, not the largest or smallest. The largest possible gob, in principle, is one with diameter equal to the tank diameter since all scales are potentially unstable.

Table 4.5.2. Comparison of GRE Volume Predictions

Standard Volume (m^3)	AN-103	AN-104	AN-105	AW-101	SY-101	SY-103
Approximate Solution Eq. (4.5.17)	14 ± 8	14 ± 6	29 ± 12	19 ± 8	100 ± 62	6 ± 4
Full Solution Eq. (4.5.4)	12 ± 7	17 ± 7	32 ± 13	17 ± 8	117 ± 76	7 ± 5
Historical Average	14 ± 4	23 ± 16	26 ± 11	14 ± 10	131 ± 47	13 ± 6

4.6 A Criterion for Gas Release During Buoyant Displacement

Up to this point in our modeling, we have assumed that all buoyant displacements produce GREs. The mechanisms or conditions whereby the gas retaining solid-liquid matrix is disrupted and gas is released have not been addressed. The actual gas release process is complex and not easily modeled. However, basic energy conservation principles can be applied to the process of gas release during buoyant displacement to determine the conditions required for it to occur. The advantage of this approach is that only the initial and final states of the gas retaining material are required, not a detailed knowledge of the actual complex processes.

A simple predictive model is presented in this section that describes the energy requirements of buoyant displacement in terms of estimated or measurable parameters. The model establishes a criterion for gas release by buoyant displacement. The total amount of energy stored in a gob of gas-bearing solids must exceed the energy required to yield the gas-retaining matrix. The model is compared with data from scaled experiments and applied to the six DSTs on the FGWL.

4.6.1 Buoyant Energy of Nonconvective Layer

To calculate the available energy that can be released by a buoyant displacement, consider an initial volume or "gob" of buoyant, gas-retaining nonconvective material, V_0, as shown in Figure 4.6.1. This volume is composed of both degassed material, V_s, and gas, V_{g0}. The gob is sufficiently buoyant to break free from the surrounding material and begin to rise. To achieve this, its initial void fraction, α_0, must be at least that required for neutral buoyancy. According to the results in Section 4.4, the initial void fraction is slightly larger than neutral buoyancy due to the effects of nonconvective material strength.

The initial volume possesses potential energy due to its buoyant state and the distance it can rise before reaching the waste surface. This energy is the maximum that can be released during a displacement event. Not all of this energy will go into yielding the buoyant gob, since some will be dissipated in viscous motion; however, it does represent the maximum energy available. The stored buoyant energy can be calculated from the work done in raising the gob a distance h, given by

$$E_b = \int_0^h F(z)dz \qquad (4.6.1)$$

where F(z) is the net buoyant force on the volume given by

$$F(z) = [\rho_L V(z) - \rho_s V_s]g \tag{4.6.2}$$

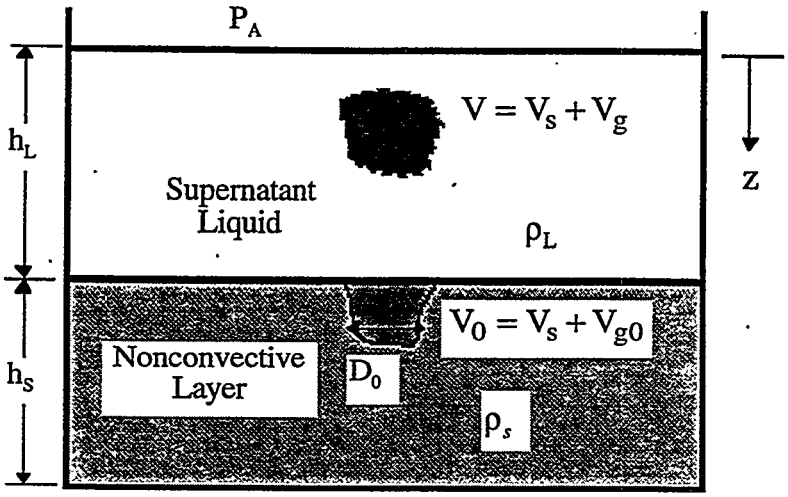

Figure 4.6.1. Geometry and Nomenclature for Gas Release Model

The limit of integration, h, is the distance from the center of the participating gob to the top of the liquid layer, which is given approximately by

$$h \approx h_L + h_g/2 \tag{4.6.3}$$

where h_g is the height of the gob. For cylindrical gobs that extend to the bottom of the nonconvective layer, $h_g = h_S$.

Eq. (4.6.2) can be expressed in terms of known quantities with the following relations:

$$V_0 = V_S + V_{g0} \tag{4.6.4}$$

$$V(z) = V_s + V_g(z) \tag{4.6.5}$$

$$V_s = (1-\alpha_0)V(z) \tag{4.6.6}$$

$$V_g(z) = V_{g0}P_0/P(z) \tag{4.6.7}$$

$$P(z) = P_A + \rho_L gz \tag{4.6.8}$$

Eq. (4.6.7) assumes the gas expands isothermally as the gob rises. Eq. (4.6.8) gives the pressure distribution in the liquid layer; however, it is applied to the nonconvective layer as well since the bulk density in the nonconvective layer is very close to the supernatant density prior to a buoyant displacement. By combining Eq. (4.6.4) through (4.6.8), Eq. (4.6.2) can be written as

$$F(z) = \alpha_0 \rho_L V_0 g\left(\frac{\gamma+1}{1+\gamma z/h} - k\right) \tag{4.6.9}$$

where the parameters γ and k are given by

$$\gamma = \rho_L g h / P_A \tag{4.6.10}$$

$$k = \frac{\alpha_{NB}(1-\alpha_0)}{\alpha_0(1-\alpha_{NB})} \tag{4.6.11}$$

If the initial void fraction is equal to the neutral buoyancy void fraction, then $k = 1$. When the initial void fraction is greater than the neutral buoyant void fraction, $k < 1$.

The integral in Eq. (4.6.1) can now be evaluated with the aid of Eq. (4.6.9) to give the buoyant potential energy available during a buoyant displacement as

$$E_b = \alpha_0 V_0 \rho_L g h[(1+1/\gamma)\ln(1+\gamma) - k] \tag{4.6.12}$$

4.6.2 Energy Required to Release Gas

In this section, we estimate the energy required to yield a volume of material participating in a buoyant displacement. We assume that the material has a finite yield strength that must be overcome to release gas bubbles. The structural properties of actual waste is unknown and is expected to be complex; however, most materials have some basic features that allow us to estimate yield energy. Regardless of the material characteristics, the energy required to produce a specified strain in a volume of material is equal to the work done on the volume by an externally applied stress to create that strain in the entire volume. We postulate that at a sufficiently high strain the material fails or begins to act as a fluid such that it can no longer restrain gas bubbles from escaping. This is expressed mathematically as

$$E_y = V_s \int_0^{\varepsilon_y} \tau d\varepsilon \tag{4.6.13}$$

Here, τ is the stress applied to the volume and ε is the strain (relative elongation). The limit of integration, ε_y, is the strain at failure. This integration can be performed if the stress-strain relation is known. Note however, that a knowledge of the rheological behavior of the fluidized material after failure is not required.

Based on the few rheological measurements available and the behavior of the material during core sample extrusion, the colloidal materials typical of a DST nonconvective layer are expected to be quite ductile. Failure probably occurs only after significant plastic deformation. Figure 4.6.2 shows stress-strain data for a bentonite clay simulant that exhibits this behavior.[(a)] Data were taken at two different strain rates; the lower strain-rate data are shown on the left in the figure. The linear-elastic, plastic, and thixotropic regions are clearly visible; the linear region extends to strains up to about 10% (0.1). As the stress increases above a certain critical value (about 190 Pa for the low strain-rate case and 230 Pa for the high strain-rate case), there is a sudden failure or relaxation. Beyond this point the material behaves plastically, where the stress is approximately constant with strain. Finally, at a strain of about 1.6 for the low strain-rate case and 1.2 for the high strain-rate case, a thixotropic fluid region is encountered where the material is essentially flowing and no longer possesses solid-like properties.

(a) Data from internal letter report by JR Phillips (PNNL) entitled, *A Basic Survey of Simulant Materials for the Ball Rheometry Project.*

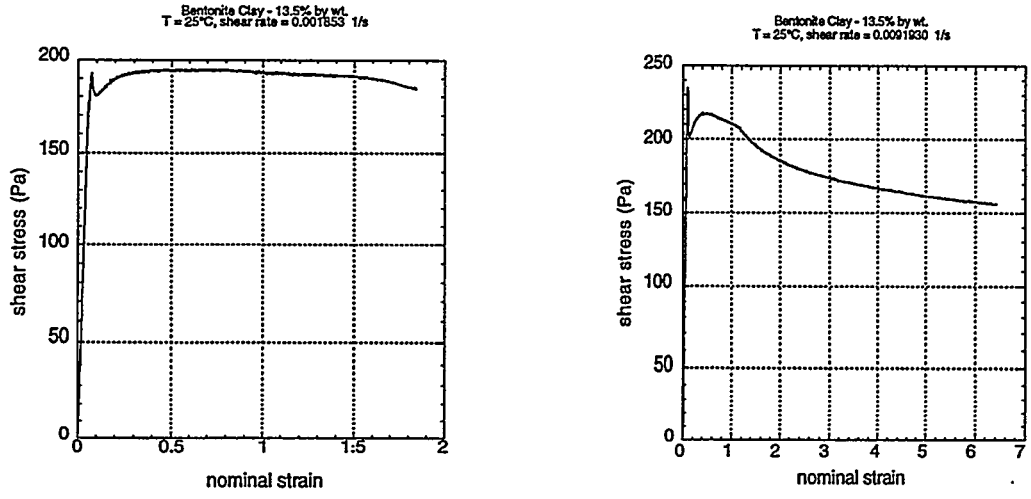

Figure 4.6.2. Stress-Strain Data for Bentonite Sludge Simulant for Two Strain Rates

Assuming the waste behaves similarly, the stress-strain model is simplified to consist of linear-elastic behavior up to 10% strain followed by a plastic region where the stress is equal to the yield stress up to a strain of 1.0, where failure is assumed to occur and the material becomes fluid. With this model, the energy required to yield the material is approximately $E_y = \varepsilon_y V_s \tau_y$, where $\varepsilon_y \approx 1$ is the strain at thixotropic transition. With $V_s = (1-\alpha_0)V_0$ and using Eq. (4.6.12), the energy required to yield the sludge is approximately

$$E_y = V_0 \varepsilon_y \tau_y (1-\alpha_0) \tag{4.6.14}$$

4.6.3 The Gas Release Criterion

The criterion states that gas release will not occur if the buoyant energy available is less than that required to yield the gas-bearing gob participating in the buoyant displacement. The ratio of the two energies given by Eq. (4.6.11) and (4.6.13) is

$$\frac{E_b}{E_y} = \frac{\alpha_0 \rho_L g h}{(1-\alpha_0)\varepsilon_y \tau_y}\left((1+1/\gamma)\ln(1+\gamma) - k\right) \tag{4.6.15}$$

If $E_b/E_y > 1$, we expect a buoyant displacement to release at least some of the retained gas. Otherwise, we expect little or no gas to be released. But a large fraction of the buoyant energy is dissipated in processes other than yielding the rising gob, so more energy is required than just enough to bring the ratio to 1.0.

To find out how much greater than 1.0 the ratio needs to be, we can evaluate the criterion of Eq. (4.6.15) with the results of scaled buoyant displacement experiments (Stewart et al. 1996b). These experiments used a bentonite clay simulant with gas produced in situ by decomposition of hydrogen peroxide. The model inputs and results are shown in Table 4.6.1. In the first test, a

Table 4.6.1. The Energy Model Applied to Scaled Buoyant Displacement Experiments

Case	ρ_s (kg/m^3)	α_0, α_{NB}	k	h_L (m)	γ	τ_y (Pa)	E_b/E_y	Energetic	Gas Release
1	1087	0.25, 0.087	0.286	0.105	0.010	67	2.6	Y	N
2	1087	0.25, 0.087	0.286	0.012	0.0012	67	0.30	N	N
3	1070	0.15, 0.07	0.426	0.101	0.0099	14	5.2	Y	Y
4	1070	0.20, 0.07	0.426	0.011	0.0011	14	0.81	N	N

displacement occurred, but very little gas was released because the individual gobs, while rising to the surface, did not break apart and release their gas. Eq. (4.6.15) gives an energy ratio of 2.6 for this case.

The conditions of the second case are the same as those of the first, but the depth of the liquid layer is reduced. For this case, no active displacement or gas release was observed. The model predicts an energy ratio of 0.3. In the third and fourth cases, a weaker simulant was used. In case 3, with a predicted energy ratio of 5.2, both an energetic displacement and a gas release were observed. In the final case, the liquid layer was reduced, and again no active displacement was observed. A small amount of gas was released, but the mechanism appeared to be percolation rather than buoyant displacement. The energy ratio for this case is 0.81, consistent with the observed behavior.

Table 4.6.2 shows model results for the DSTs on the FGWL. The first row shows energy ratios for gobs with diameter equal to nonconvective layer depth. All of the energy ratios are greater than 5.0, implying that there is sufficient energy in a buoyant displacement to release a large fraction of its trapped gas. This result is expected since all the tanks under consideration exhibit periodic GREs. We see that AN-105 has the highest energy ratio, while SY-103 has the smallest. The second row shows results for the small gob limit. Here, the diameter of the gob is negligible compared with the convective layer depth. This case represents very small gobs that break away from the top of the nonconvective layer. Again, all of the energy ratios are greater than 5.0, implying that small buoyant displacements will also release gas.

While these observations and the scaled experiment results are not sufficient to precisely quantify the relation between gas release and energy ratio, they are consistent with the following criteria: no disruptive buoyant displacement is predicted for $E_b/E_y<1$, buoyant displacements with limited gas release might occur for $E_b/E_y>\sim2$, and major gas releases can be expected if $E_b/E_y>\sim5$. For typical tank conditions, Eq. (4.6.15) requires the supernatant liquid depth to exceed about 1 m for buoyant displacements with limited gas release and over 3 m for significant gas release. These conditions currently exist only in the DSTs.

Table 4.6.2. Energy Ratio Calculated for Six DSTs

	AN-103	AN-104	AN-105	AW-101	SY-101	SY-103
Largest: $h_g = h_s/2$	26	49	52	44	24	13
Smallest: $h_g = 0$	18	29	31	35	11	8

4.7 Recommendations for Improving Gas Release Models

Given measurements or estimates of the waste properties, configuration, and gas volume, the models discussed in the preceding sections can predict the size and frequency of gas releases from tanks with a waste configuration representing current DSTs. These calculations assume that gas can accumulate in the waste up to the point of neutral buoyancy. However, there is clear evidence that the maximum void fraction is limited, and many tanks simply do not retain a significant volume of gas. Therefore, the predicted gas releases may not occur at all.

Unfortunately, we cannot yet predict the gas retention ability based on waste properties and dimensions. This capability is most urgently needed to assess the potential flammable gas hazard resulting from waste transfers. Theoretical studies at Los Alamos National Laboratory aimed at predicting the steady-state background gas release rate are beginning to make progress.[a] If the background release rate is known as a function of void fraction, the maximum void fraction will occur when the background release is equal to the total generation rate. These studies need to be pursued.

Laboratory experiments have been performed on simulants and real waste samples that show a maximum void fraction of 0.25 to 0.35 (Gauglitz et al. 1996). However, these tests were done in very small vessels with extremely fast gas generation rates relative to tank conditions. Wall effects and the absence of correct hydrostatic pressure difference undoubtedly affect the results. A long-term, large-scale experiment on real waste material to resolve these difficulties should be given high priority.

Even given the capability to predict the maximum void fraction and gas release volume, the tank data set available to validate such models is very limited. We only have data on tanks that are known to release significant volumes of gas regularly. We have essentially no data on DSTs that do not show episodic releases. The VFI is scheduled to be run in one riser of AN-107 in FY 1997. We also recommend that the VFI and ball rheometer be operated in AW-104 at the earliest convenient time. This will provide vital information on the conditions required to *prevent* gas retention and release.

(a) Presentation by K Pasamehmetoglu, LANL, to the Flammable Gas Project, March 4, 1997.

5.0 Potential Consequences of Gas Releases

The peak head-space pressure resulting from a postulated deflagration has been calculated for each of the six tanks using a probabilistic model that assumes a release of an arbitrary fraction of the gas retained in the nonconvective layer at random times. The procedure for estimating the burn pressure uses the best estimates available for the required input and the associated uncertainty, including the uncertainty in the gas volume itself, in its composition, and in the variation in the gas volume with time according to the tanks' level history. Section 5.1 discusses the gas composition, Section 5.2 describes the combustion model and calculational procedure, and Section 5.3 presents the results. Recommendations for improving the peak pressure model are given in Section 5.4.

5.1 Gas Composition

The composition of the gas released from the waste must be known to determine the volume of flammable gas as a function of time following a release. The released gas composition has been estimated from the head-space gas concentrations after large GREs in SY-101 (Sullivan 1997) and also inferred from the ratios of steady-state head-space concentrations (Van Vleet 1996). Only SY-101 has released sufficiently large gas volumes that the head-space concentration accurately represents the concentration of the gas released from the waste. Inferring release gas concentrations from the steady-state head space requires assumptions about the concentrations of nitrogen and any important species not measured by the installed monitoring system. The steady-state head-space concentration ratios are also quite variable and do not match the actual waste gas concentrations obtained with the RGS.

We believe that the composition of gas found in the waste is the best representation of the composition of the released gas. The RGS is the only instrument in use that provides in-situ waste gas composition directly. These measurements are used for AN-103, AN-104, AN-105, and AW-101.

The waste gas compositions in SY-101 prior to mixing are derived from the values given in the mixer pump safety assessment (Sullivan 1997). The composition given in the safety assessment represents the released gas, including the ammonia co-release, not the waste gas. The waste gas concentrations are derived by reducing the ammonia concentration from the reported 11% to 6%, which is the estimated ammonia concentration in the bubbles, and normalizing the other species accordingly. The uncertainties are computed as the difference between the "conservative estimate" and "best estimate" values given in the safety assessment.

The waste gas composition for SY-103 is derived from gas generation tests on actual waste samples that were described in Section 2. No other tank has as yet been tested in this way. The results allow estimates to be made of the generation rates of hydrogen, nitrous oxide, and nitrogen at tank conditions. The estimated gas generation rates for SY-103 at 33°C and 441 R/hour are[a]

Hydrogen	$2.1(10^{-6}) \pm 10\%$ mol/kg/day
Nitrous Oxide	$4.3(10^{-7}) \pm 30\%$ mol/kg/day
Nitrogen	$7.8(10^{-7})$ mol/kg/day

(a) Electronic message, CM King (PNNL) to CW Stewart (PNNL), May 5, 1997, "SY-103 gas generation rates under tank conditions."

The uncertainty for nitrogen is not specified but is stated to be high. The fraction of each of these gases in the waste is assumed to be proportional to the above generation rates. This gives relative concentrations of 63 ± 6% for hydrogen, 13 ± 4% for nitrous oxide, and 24 ± 7% for nitrogen. The uncertainty for nitrogen is assumed to be the square root of the sum of the squares of the hydrogen and nitrous oxide uncertainties. Concentrations of ammonia, methane, and other gases are assumed to be the same as SY-101. The hydrogen, nitrous oxide, and nitrogen concentrations are reduced accordingly to make the total 100%.

Given the composition, the mixture concentration in the head space at the lower LFL is determined from LeChatelier's rule:

$$\frac{1}{LFL_{MIX}} = \frac{[H_2]}{LFL_{H_2}} + \frac{[CH_4]}{LFL_{CH_4}} + \frac{[NH_3]}{LFL_{NH_3}} + \frac{[CO]}{LFL_{CO}} \qquad (5.1.1)$$

where the LFL concentrations of hydrogen, methane, ammonia, and carbon monoxide are 4, 5.5, 15, and 12.5%, respectively. The ammonia concentration in Eq. (5.1.1) includes both that in the escaping gas bubbles plus an additional amount assumed to evaporate from the waste surface as it is disturbed by the gas release. Assuming the volume of ammonia that evaporates from the surface can be expressed as a co-release fraction, F_{EVAP}, of the total gas release volume, the mixture LFL can be related to the waste gas composition by

$$\frac{1}{LFL_{MIX}} = \frac{1}{1+F_{EVAP}}\left[\frac{[H_2]}{LFL_{H_2}} + \frac{[CH_4]}{LFL_{CH_4}} + \frac{[NH_3]+F_{EVAP}}{LFL_{NH_3}} + \frac{[CO]}{LFL_{CO}}\right] \qquad (5.1.2)$$

The ammonia co-release fraction in SY-101 and SY-103 was established as 0.06 (Stewart et al. 1996a). The evaporation rate, and therefore the co-release fraction, should be approximately proportional to the dissolved ammonia concentration in the liquid. Since the other tanks have at least an order of magnitude lower dissolved ammonia concentration in the liquid, their co-release fraction is deemed insignificant and is set to zero.

The volume of waste gas that would need to be released to bring the head space just to the LFL is the product of the tank head space and the mixture LFL concentration. Dividing this volume by the stored gas volume in the nonconvective layer (see Tables 3.1.2 and 4.1.1 for SY-101) gives the gas release fraction necessary to bring the head space to LFL.

Table 5.1.1 summarizes the gas compositions and flammability information derived above. Note that there is insufficient stored gas in AW-101 and SY-103 to make the entire dome flammable even if all of the gas were released. Also, the required release fractions for the other tanks (except for SY-101) are much higher than those of observed GREs to date (see Table 4.1.1).

5.2 Peak Pressure Model

The peak head-space pressure resulting from a postulated deflagration is determined in order to assess the potential safety consequences of releasing part or all of a tank's stored gas volume. The hazard is evaluated by comparing the predicted peak pressure with the maximum allowable pressure, which is assumed to be 3.08-atm gauge (3.0 bar). We do not consider specific

Table 5.1.1. Waste Gas Composition and Flammability Summary

	AN-103	AN-104	AN-105	AW-101	SY-101[a]	SY-103[b]
Waste Gas Composition						
Ammonia (%)	0.06 ± 0.06	0.02 ± 0.02	0.03 ± 0.03	0.02 ± 0.02	6 ± 4	6 ± 4
Nitrogen (%)	34 ± 5	32 ± 3	25 ± 2	60 ± 5	35 ± 9	22 ± 7
Hydrogen (%)	61 ± 8	47 ± 4	63 ± 4	31 ± 3	30 ± 3	57 ± 6
Nitrous Oxide (%)	3.8 ± 0.5	19 ± 2	11 ± 1	4.3 ± 0.4	26 ± 2	12 ± 4
Methane (%)	0.7 ± 0.1	1.8 ± 0.3	0.7 ± 0.1	1.9 ± 0.3	0.37 ± 0.2	0.37 ± 0.2
Other gases (%)	0.4 ± 5	0.2 ± 2	0.3 ± 2	2.8 ± 3	2.6 ± 0.4	2.6 ± 0.4
Diss. Ammonia (μm/L)	2200 ± 1200	2100 ± 900	1400 ± 500	2200 ± 700	200,000	200,000
Head Space Flammability						
Mix. Conc. @ LFL (%)	6.4 ± 0.8	8.3 ± 0.7	6.4 ± 0.4	12 ± 1	12 ± 1	7 ± 0.7
Tank head space (m^3)	1712 ± 20	1323 ± 20	1066 ± 21	1070 ± 30	1023 ± 22	2503 ± 13
Mix. vol. for LFL (m^3)	109 ± 13	110 ± 10	67 ± 4	125 ± 11	125 ± 12	170 ± 17
Stored gas vol. (Std. m^3)	314 ± 31	207 ± 28	161 ± 30	93 ± 13	394 ± 84	148 ± 45
Rel. fraction for LFL	0.35 ± 0.05	0.50 ± 0.09	0.40 ± 0.08	1.3 ± 0.2	0.30 ± 0.07	1.2 ± 0.4

(a) SY-101 compositions were taken from Sullivan et al. (1997).
(b) SY-103 N_2, H_2, and N_2O compositions were derived from gas generation tests (Bryan et al. 1996).

gas release mechanisms but vary the release fraction from 0 to 1.0 as a parameter to cover all possible releases. The combustion model is based on LANL's maximum allowable release analysis for SY-103.[a]

Uncertainties in the gas volumes and compositions and other data are specifically included by a probabilistic implementation of the gas release and combustion model. Inputs are described as probability distributions. The distribution of the burn pressure over the full range of the input is computed by the simulations described below. The probability distributions so derived are conditional and very conservatively assume ignition of the entire gas release volume. Dilution or other plume effects that reduce the volume of gas that is actually flammable, and the effects of less than perfect combustion efficiency are left to a more detailed calculation. The inputs modeled as probability distributions are as follows:

- species concentration in the waste gas
  - hydrogen
  - nitrous oxide
  - methane
  - carbon monoxide ("other" gases in Table 5.1.1 assumed to be CO)
  - ammonia
- ratio of volume of dissolved ammonia evaporated to total volume of free gas released
- void fraction in each subregion of the nonconvective layer
- pressure in each subregion of the nonconvective layer
- waste level at time of release

The void fraction and pressure distributions in each sublevel are assumed normal with statistics based on the actual VFI observations as described in Section 3. Distributions for the major gas components for the equivalent fuel calculation were obtained from the following sources with nominal values given in Table 5.1.1:

(a) Pasamehmetoglu KO. 1996. *Maximum Allowable Gas Release Volume Predictions.* Letter report TSA-10-96-329, Los Alamos National Laboratory, Los Alamos, New Mexico.

- RGS: AW-101, AN-103, AN-104, AN-105 (Shekarriz et al. 1997).
- Head space analysis of a large GRE: SY-101 (Sullivan [1997], modified to convert release gas concentration to waste gas concentration).
- Gas generation tests: SY-103 (hydrogen, nitrous oxide and nitrogen from Bryan et al [1996] with the rest assumed equal to SY-101).

Some volume of dissolved ammonia evaporates from the waste surface during a GRE in addition to the free gas volume released. If the ratio of dissolved to free gas release volume is denoted as F_{EVAP}, the free gas volume released is multiplied by a factor $[1 + F_{EVAP}]$ to get the total release volume. At the same time, the waste gas concentrations are reduced by the same factor in computing equivalent fuel values and flammability in the head space.

$$\chi_i' = \frac{\chi_i}{1+F_{EVAP}} \tag{5.2.1}$$

where χ_i' is the concentration of component i in the release gas. The ammonia concentration in the head space after the release is given by

$$\chi_A' = \frac{\chi_A + F_{EVAP}}{1+F_{EVAP}} \tag{5.2.2}$$

Waste level appears in two ways in the calculation. There was a point-level observation at the time of the VFI measurement—from which the degassed level is calculated—that was not modeled as a distribution. Given the degassed level, the waste level at the time of a gas release must be input to define the stored gas volume available. The distribution for the pre-GRE waste level was obtained from actual level data over a long time period; these were processed to produce a piece-wise constant distribution. An 'add-on' uncertainty modeled as a uniform distribution in [-0.025, 0.025] meters was applied to the base distribution account for FIC flushes and offsets due to changes of level instruments. The SY-101 level was input as a normal distribution with mean and standard deviation derived from the 'before GRE' column of Table 4.1.2.

The peak pressure model begins by calculating the volume-averaged pressure ($\ddot{p}$), in atmospheres, of the undissolved gas in the nonconvective layer:

$$\ddot{p}_{NC} = \frac{1}{V_{NC}\hat{p}} \sum_{i=1}^{NC} \alpha_i H_i p_i \tag{5.2.3}$$

where p_i is the layer pressure defined by Eq. (3.1.5). This differs from the average pressure ratio defined by Eq. (3.1.11) in neglecting the temperature correction.

Next, the fraction of the fuel that is oxidized by nitrous oxide (rather than oxygen) is estimated, and the total equivalent fuel value (for all fuels present) is determined. It should be noted that recent flammability tests at California Institute of Technology[a] suggest that nitrous oxide is essentially inert in lean conditions close to the LFL. However, it does apparently participate actively when the flame temperature exceeds 1300K. Since this is likely to occur in burns of larger

(a) Personal communication, ME Brewster (PNNL) with J Shepard (CIT), August 1996.

volumes that might exceed the maximum pressure, we consider nitrous oxide to be as effective as oxygen, recognizing that this may be over-conservative for small releases. Combustion energies with oxygen and nitrous oxide are compared in Table 5.2.1.

$$\eta_U = \frac{\chi_N}{S_H\chi_H + S_A\chi_A + S_M\chi_M + S_C\chi_C} \tag{5.2.4}$$

$$\eta_D = \frac{\chi_N}{S_A} \tag{5.2.5}$$

$$\eta_{TOT} = \frac{1}{(1/\eta_U + F_{EVAP}/\eta_D)} \tag{5.2.6}$$

$$e_{TOT} = \left(\frac{1}{1+F_{EVAP}}\right)\left\{\begin{array}{l}\chi_H(E_{HN}\eta_{TOT} + (1-\eta_{TOT}) + (\chi_A + F_{EVAP})(E_{AN}\eta_{TOT} + E_A(1-\eta_{TOT}) + \\ \chi_M(E_{MN}\eta_{TOT} + E_M(1-\eta_{TOT}) + \chi_C(E_{CNN}\eta_{TOT} + E_C(1-\eta_{TOT})\end{array}\right\} \tag{5.2.7}$$

where

η_U = the fraction of fuel from undissolved gas that is oxidized by N_2O

η_D = the fraction of fuel from dissolved gas that is oxidized by N_2O

η_{TOT} = the total fraction of fuel oxidized by N_2O

χ = the concentration (mole fraction) of a component in the undissolved gas; the subscript H is hydrogen, A is ammonia, M is methane, C is carbon monoxide, and N is nitrous oxide

S = the stoichiometric ratio for a gas component when burned with N_2O; subscripts are as noted above

F_{EVAP} = the ratio of ammonia released from solution to that released from undissolved gas.

e_{TOT} = the total equivalent fuel value (in terms of hydrogen)

E = the equivalent fuel value of gases other than hydrogen when burned in oxygen; subscripts are as noted above.

$E_{...N}$ = the equivalent fuel value of gases when burned in nitrous oxide; subscripts are as noted above.

Table 5.2.1. Combustion Energies of Different Fuel-Oxidizer Pairs (Sullivan 1995)

Fuel	Combustion Energy (kJ/mole of fuel)	
	Oxygen	Nitrous oxide
Hydrogen	-241	-324
Ammonia	-317	-442
Methane	-789	-1132
Carbon monoxide	-281	-365

The total head-space volume available to absorb the burn energy depends on the depth of the waste immediately after a GRE (and immediately preceding the hypothetical burn). The depth, L_{post}, is given by

$$L_{post} = L_{NO-GAS} + (1 - F_{REL})(L - L_{NO-GAS}) \quad (5.2.8)$$

where

L = the waste level (m) at some randomly selected observation time
F_{REL} = the ratio of the volume of undissolved gas released to the total undissolved gas present in the nonconvective layer
L_{post} = the waste level (m) after a GRE.

The standard volume of gas released is proportional to the total gas volume before the GRE, the release fraction, the fraction of dissolved gas released with the insoluble gas, and the pressure at which the gas is stored. This is expressed as

$$\hat{V}_{REL} = F_{REL}(1 + F_{EVAP})(L - L_{NO-GAS})A(\bar{p}_{NC}\hat{T}/T_{NC}) \quad (5.2.9)$$

where

A = the cross-sectional area of the tank (m^2)
T_{NC} = the estimated nonconvective layer temperature (K)
$\hat{T}$ = the standard temperature (K)
$\hat{V}_{REL}$ = the standard volume of gas released (m^3).

Finally, the peak pressure (in atm gauge) that can be achieved by burning the entire release is computed by scaling a very detailed coupled combustion and structural calculation of burn pressure performed for SY-101 (Sullivan 1995). The SY-101 calculation predicted a 2.91 atm (2.95 bar) gauge pressure as a result of burning 245 m^3 (8,650 SCF) of gas, equivalent to 62.7% hydrogen combusted in air, in a head-space volume of 1,218 m^3 (43,000 ft^3). Assuming a linear dependence, this result is simply scaled by the release volume, head-space volume, and equivalent fuel value of the release gas to estimate the peak pressure in the tank of interest. The scaling is expressed as

$$P_{PEAK} = \frac{\Theta e_{TOT}\hat{V}_{REL}}{(V_{dome} + A(L_{MAX} - L_{post})} \quad (5.2.10)$$

where

Θ = 23.09 atm = 2.91 atm • 1,218 m^3/(245 m^3 • 0.627 H_2); the pressure per concentration of hydrogen-equivalent fuel burned
V_{dome} = the volume (m^3) of the dome space above L_{MAX}.
L_{MAX} = the waste level at maximum capacity (m).

The software Crystal Ball® was used to perform the simulations. Five-thousand samples were used to ensure that the simulation had converged in the tail of the distribution. The results of the simulation were output as percentile (cumulative distribution) in increments of 5%. Results are presented for each tank in terms of the peak burn pressure at the 50th, 95th and 99th percentile as a function of the release fraction. The results of the Monte Carlo simulation were verified for convergence up to the 99th percentile values, which were the largest values used in the graphs in this section. The results are deemed accurate to one significant figure at the 99th percentile value. These results are presented in context in Section 5.3.

5.3 Peak Pressure Predictions

Plots of the estimated peak burn pressure versus fraction of retained gas released are shown for each tank in Figures 5.3.1 through 5.3.6. These plots are intended to portray a tank's 'hazard signature.' Three curves are shown: the median (50th percentile), or best estimate burn pressure; the 95th percentile; and the 99th percentile.

A sensitivity analysis was performed to validate the use of point estimates for certain parameters. The dominant sources of uncertainty in the peak pressure calculation vary from tank to tank. In SY-101 the waste level, which defines the stored gas volume available for release, dominates. It was input as a normal distribution with average and standard deviations derived from the historical level readings just before each GRE, which vary considerably. In the other tanks, the level is input as an empirical distribution created simply by binning all the waste level readings, ignoring how the readings relate to GREs. The dominant uncertainty for AN-103, AN-104, AN-105, and AW-101 calculations was in the hydrogen concentrations. In the case of AN-103 this is due to the small number of measurements available. In the other cases the uncertainty is due to the scatter in the measurements. The uncertainty in the nonconvective layer void fraction dominated in Tank SY-103 due to spatial nonuniformity in the measurements.

The hazard signatures compare the predicted peak pressures with the limiting dome pressure difference of 3.08 atm (312 kPa, 45.3 psig). This pressure was determined in the SY-101 mixer pump safety assessment (Sullivan 1995) to maintain confinement of radioactive waste within the primary liner. Though the analysis predicts extensive concrete cracking and rebar yielding throughout the dome structure at this pressure, gross structural deformations are prevented. The peak dome apex velocity is also predicted to be under the limiting value at which the overlying soil would separate and re-impact the dome, potentially causing it to collapse. To put this in perspective, the estimated peak pressure required to rupture the HEPA filters is 0.168 atm (17 kPa), and that to blow the seals is 0.025 atm (2.5 kPa).[a]

The solid and dashed vertical lines on each "hazard signature" represent the mean and maximum release fraction observed in the tank's GRE history. This shows the range of potential consequences resulting from what the tank has been known to do. Higher release fractions might result from a severe seismic event, for example.

The release fraction required to bring the entire mixed head space to the LFL is also shown by a vertical line on each hazard signature. The mixture LFL is computed via LeChatelier's linear combination rule based on the 50th percentile values for the concentrations given in Table 5.1.1.

The hazard signature estimated for SY-101 prior to mixer pump installation is given in Figure 5.3.1. This figure is essentially unchanged from that shown in Stewart et al. (1996a). The best estimate peak burn pressure is predicted to exceed the 3.08 atm maximum at the maximum historical release. Releases cannot be much larger than the median to remain below the maximum pressure at a 99% confidence limit. Even the expected release exceeds the LFL. It is clear that this tank presented a significant hazard.

The signatures of SY-103 and AW-101 are shown in Figures 5.3.2 and 5.3.3. SY-103 has such a large head space and AW-101 such a low hydrogen concentration and gas volume that, even for a 100% release, the peak burn pressure would remain below the 3.08 atm limit at 99% confidence, and the fully mixed head space would remain well below the LFL.

(a) Personal communication, RJ Van Vleet (FDNW) to CW Stewart (PNNL), January 6, 1997.

The hazard signatures for AN-103, AN-104, and AN-105 are shown in Figures 5.3.4, 5.3.5, and 5.3.6, respectively. None of them has ever released enough gas in historical GREs to even approach the maximum allowable pressure or the LFL in the mixed head space. According to the best estimate prediction, none of them would exceed the 3.08 atm pressure limit even if all their stored gas were released.

These calculations estimate the pressure resulting from a deflagration using the best information available for comparing the relative hazard between the six DSTs on the FGWL. The model and its input are not purposefully conservative or bounding, and the results are not intended as a safety analysis, though conservative consequences can be obtained from the output distribution if desired.

The conclusion is that only SY-101 demonstrated a clear potential for a flammable gas burn that could fail the dome structure. None of the other tanks appear capable of producing peak pressures exceeding the 3.08 atm limit at 99% confidence for even a very large release of 50% of their stored gas, which is far larger than any observed to date. Two of the tanks are incapable of exceeding the pressure limit releasing 100% of their stored gas.

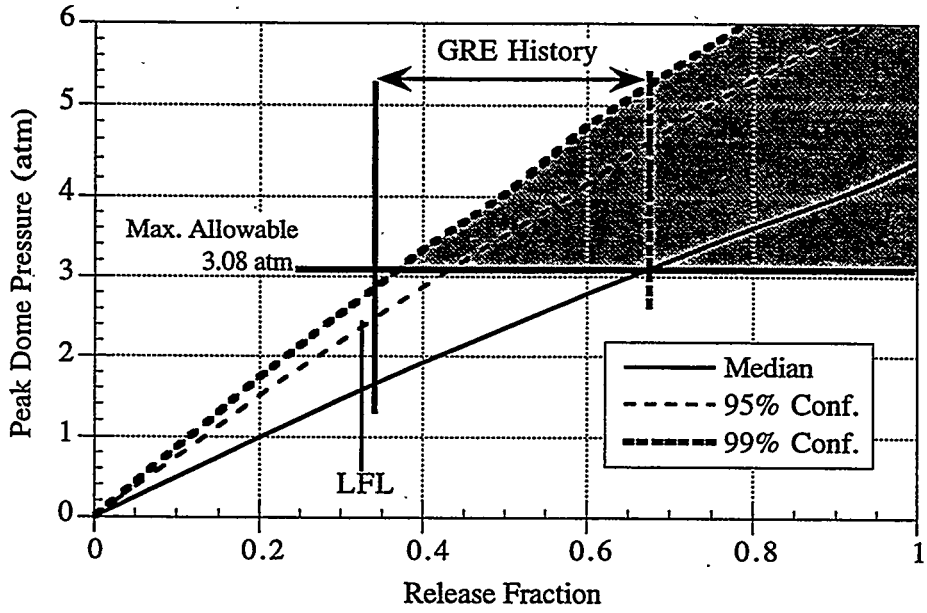

Figure 5.3.1. Peak Burn Pressure in SY-101

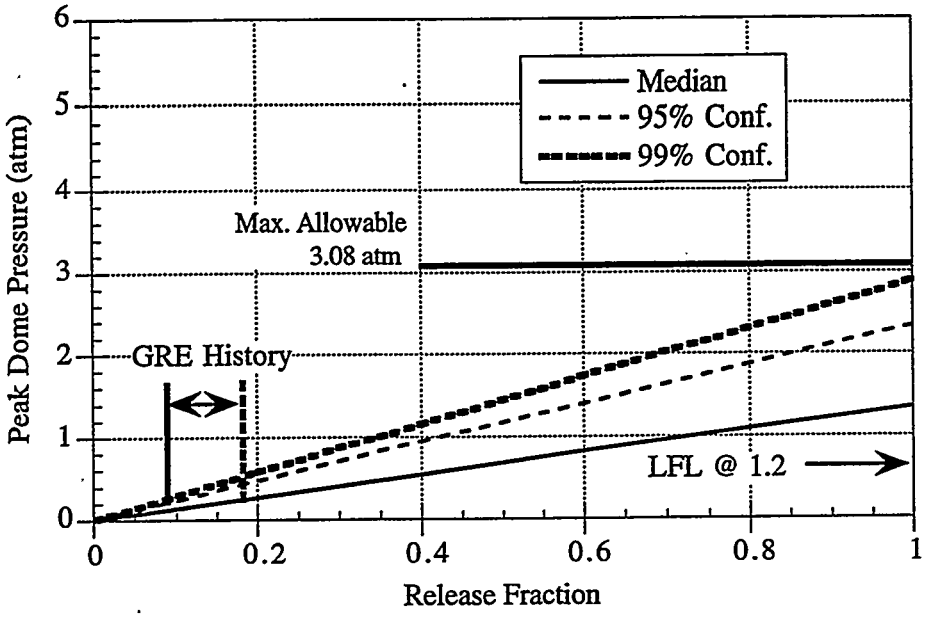

Figure 5.3.2. Peak Burn Pressure in SY-103

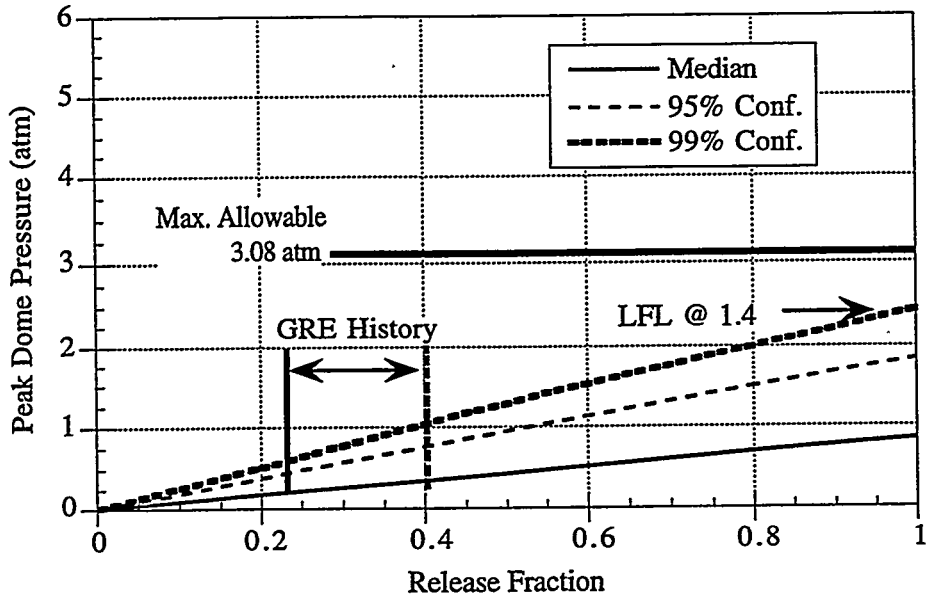

Figure 5.3.3. Peak Burn Pressure in AW-101

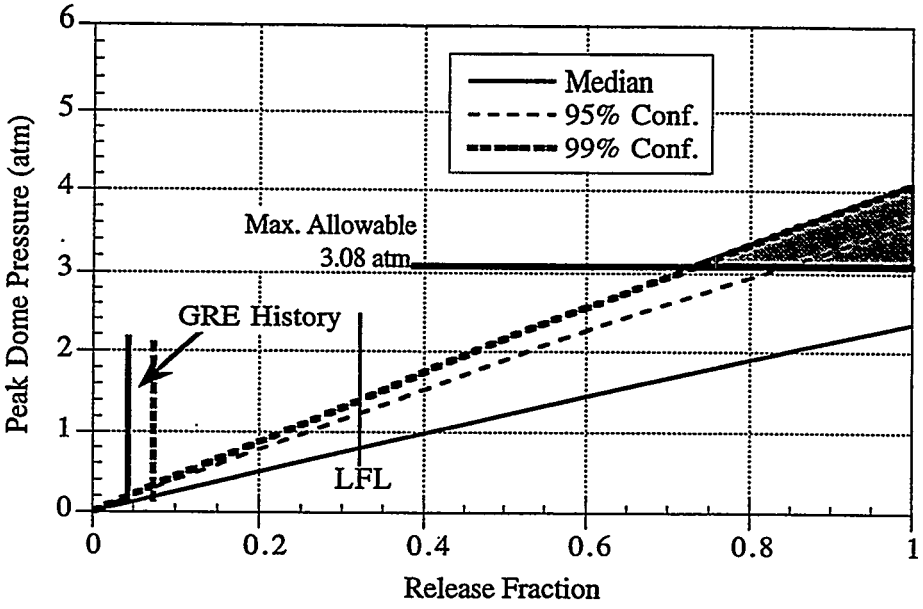

Figure 5.3.4. Peak Burn Pressure in AN-103

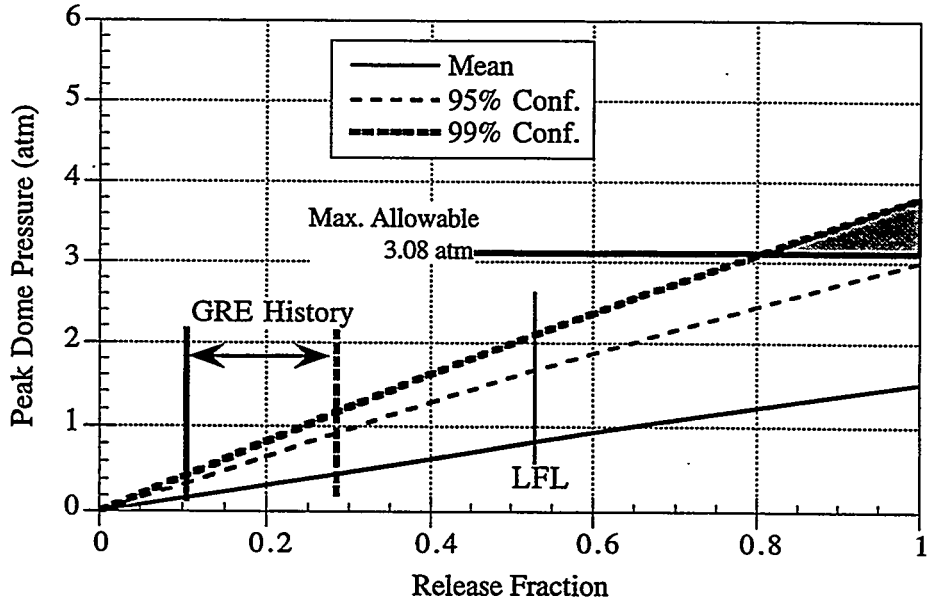

Figure 5.3.5. Peak Burn Pressure in AN-104

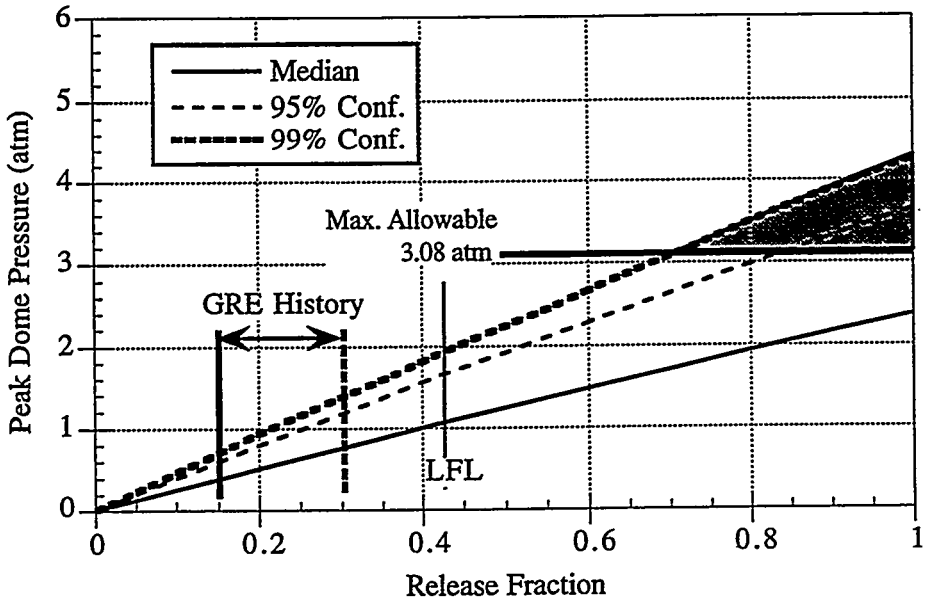

Figure 5.3.6. Peak Burn Pressure in AN-105

5.4 Recommendations for Improving Peak Pressure Models

The peak pressure calculated to result from a postulated gas release and ignition has assumed that all the released gas burns. Two important effects reduce the actual volume that can burn significantly, especially for small releases. First, the released gas begins mixing with the dome atmosphere as soon as it leaves the waste so that only a portion of the release volume exists in flammable concentrations at any instant. For small, slow releases it is probable that flammability is never achieved. It may be possible to show that only those releases that bring the entire head space to a significant fraction of the LFL are capable of burning as a plume. Second, combustion is believed to be very inefficient in very lean mixtures just above the LFL. Therefore, only a fraction of the gas that is flammable actually burns.

If it can be shown that only a small fraction of the gas that is released is flammable and that only a small fraction of the flammable volume actually burns, the safety concern due to small plume combustion can probably be eliminated. We recommend that plume mixing calculations, and possibly a confirming experiment, be continued and that ongoing combustion experiments with lean mixtures be continued.

6.0 References

Allemann RT, TM Burke, DA Reynolds, and DE Simpson. 1993. *Assessment of Gas Accumulation and Retention - Tank 241-SY-101.* WHC-EP-0576, Westinghouse Hanford Company, Richland, Washington.

Allemann RT, ZI Antoniak, WD Chvala, LE Efferding, JG Fadeff, JR Friley, WB Gregory, JD Hudson, JJ Irwin, NW Kirch, TE Michener, FE Panisko, CW Stewart, and BM Wise. 1994. *Mitigation of Tank 241-SY-101 by Pump Mixing: Results of Testing Phases A and B.* PNL-9423, Pacific Northwest Laboratory, Richland, Washington.

Antoniak ZI. 1993. *Historical Trends in Tank 241-SY-101 Waste Temperatures and Levels.* PNL-8880, Pacific Northwest Laboratory, Richland, Washington.

Barefield EK, D Boatwright, A Deshpande, F Doctorovich, CL Liotta, HM Neumann, and S Seymore. 1995, *Mechanisms of Gas Generation from Simulated SY Tank Farm Wastes: FY 1994 Progress Report.* PNL-10822, Pacific Northwest Laboratory, Richland, Washington.

Barefield EK, D Boatwright, A Deshpande, F Doctorovich, CL Liotta, HM Neumann, and S Seymore. 1996. *Mechanisms of Gas Generation from Simulated SY Tank Farm Wastes: FY 1996 Progress Report,* PNNL-11247, Pacific Northwest National Laboratory, Richland, Washington.

Brewster ME, NB Gallagher, JD Hudson, and CW Stewart. 1995. *The Behavior, Quantity, and Location of Undissolved Gas in Tank 241-SY-101.* PNL-10681, Pacific Northwest Laboratory, Richland, Washington.

Bryan S, CM King, LR Pederson, SV Forbes, and RL Sell. 1996. *Gas Generation from Tank 241-SY-103 Waste.* PNNL-10978, Pacific Northwest National Laboratory, Richland, Washington.

Caley SM, LA Mahoney, and PA Gauglitz. 1996. *Summary of Tank Information Relating Salt Well Pumping to Flammable Gas Safety Issues.* PNNL-11335, Pacific Northwest National Laboratory, Richland, Washington.

Chandrasekhar S. 1981. *Hydrodynamic and Hydromagnetic Stability.* Dover Publications, Inc., New York.

Fung YC. 1994. *A First Course in Continuum Mechanics.* Prentice-Hall, New Jersey.

Gauglitz PA, SD Rassat, MR Powell, RR Shah, and LA Mahoney. 1995. *Gas Bubble Retention and Its Effects on Waste Properties: Retention Mechanisms, Viscosity, and Tensile and Shear Strengths.* PNL-10740, Pacific Northwest Laboratory, Richland, Washington.

Gauglitz PA, SD Rassat, PR Bredt, JH Konynenbelt, JM Tingey, and DP Mendoza. 1996. *Mechanisms of Gas Bubble Retention and Release: Results for Hanford Waste Tanks 241-S-102 and 241-SY-103 and Single-Shell Tank Simulants.* PNNL-11298, Pacific Northwest National Laboratory, Richland, Washington.

Graves RD. 1994. *Topical Report on Flammable Gases in Non-Burping Waste Tanks. WHC-SD-WM-SARR-015,* Westinghouse Hanford Company, Richland, Washington.

Hartley SA, KM Remund, BC Simpson, RD Cromar, and CM Anderson. 1995. *Statistical Supplement to the Tank Characterization Reference Guide.* WHC-SD-WM-TI-648 Rev. 0, Westinghouse Hanford Company, Richland, Washington.

Hopkins JD. 1994. *Criteria for Flammable Gas Watch List Tanks.* WHC-EP-0702 Rev. 0, Westinghouse Hanford Company, Richland, Washington.

Johnson GD. 1997. *Flammable Gas Project Topical Report.* HNF-SP-1193 Rev. 2, Lockheed Martin Services Incorporated, Richland, Washington.

Kataoka I. 1986. "Local Instant Formulation of Two-Phase Flow." *Int. J. Multiphase Flow,* Vol. 12, pp. 745-757.

Macosko CW. 1994. *Rheology Principles, Measurements, and Applications.* VCH Publishers, Inc., New York.

Meisel D, CD Jonah, S Kapoor, MS Matheson, and MC Sauer. 1993. *Radiolytic and Radiolytically Induced Generation of Gases from Synthetic Wastes.* ANL-93/43, Argonne National Laboratory, Argonne, Illinois.

Pederson LR, and SA Bryan. 1996. *Status and Integration of Studies of Gas Generation in Hanford Wastes.* PNNL-11297, Pacific Northwest National Laboratory, Richland, Washington.

Person JC. 1996. *Effects of Oxygen Cover Gas and NaOH Dilution on Gas Generation in Tank 241-SY-101 Waste.* WHC-SD-WM-DTR-043, Westinghouse Hanford Company, Richland, Washington.

Reynolds DA. 1993. *Tank 101-SY Window E Core Sample: Interpretation of Results.* WHC-EP-0628, Westinghouse Hanford Company, Richland, Washington.

Shekarriz A, DR Rector, LA Mahoney, MA Chieda, JM Bates, RE Bauer, NS Cannon, BE Hey, CG Linschooten, FJ Reitz, and ER Siciliano. 1997. *Composition and Quantities of Retained Gas Measured in Hanford Waste Tanks 241-AW-101, 241-A-101, 241-AN-105, 241-AN-104, and 241-AN-103.* PNNL-11450, Rev. 1, Pacific Northwest National Laboratory, Richland, Washington.

Stewart CW, JD Hudson, JR Friley, FE Panisko, ZI Antoniak, JJ Irwin, JG Fadeff, LE Efferding, TE Michener, NW Kirch, and DA Reynolds. 1994. *Mitigation of Tank 241-SY-101 by Pump Mixing: Results of Full-Scale Testing.* PNL-9959, Pacific Northwest Laboratory, Richland, Washington.

Stewart CW, JM Alzheimer, ME Brewster, G Chen, RE Mendoza, HC Reid, CL Shepard, and G Terrones. 1996a. *In Situ Rheology and Gas Volume in Hanford Double-Shell Waste Tanks.* PNNL-11296, Pacific Northwest National Laboratory, Richland, Washington.

Stewart CW, ME Brewster, PA Gauglitz, LA Mahoney, PA Meyer, KP Recknagle, and HC Reid. 1996b. *Gas Retention and Release Behavior in Hanford Single-Shell Waste Tanks .* PNNL-11391, Pacific Northwest National Laboratory, Richland, Washington.

Sullivan HL. 1995. *A Safety Assessment for Proposed Pump Mixing Operations to Mitigate Episodic Gas Releases in Tank 241-SY-101: Hanford Site, Richland, Washington.* LA-UR-92-3196 Rev. 14, Los Alamos National Laboratory, Los Alamos, New Mexico.

Sullivan HL. 1997. *A Safety Assessment for Proposed Pump Mixing Operations to Mitigate Episodic Gas Releases in Tank 241-SY-101: Hanford Site, Richland, Washington.* HNF-SD-WM-SAD-033 Rev. 3, US Department of Energy, Richland, Washington.

Van Vleet RJ. 1996. *Summary of Flammable Gas Hazards and Potential Consequences in Tank Waste Remediation Facilities at the Hanford Site.* WHC-SD-WM-TI-753 Rev. 0, Westinghouse Hanford Company, Richland, Washington.

Whitney PD. 1995. *Screening the Hanford Tanks for Trapped Gas.* PNL-10821, Pacific Northwest Laboratory, Richland, Washington.

Whitney PD, PA Meyer, NE Wilkins, F Gao, and AG Wood. 1996. *Flammable Gas Data Evaluation Progress Report.* PNNL-11373, Pacific Northwest National Laboratory, Richland, Washington.

Wilkins NE. 1995. *Tank 241-SY-103 Core Sample: Interpretation of Results.* WHC-SD-WMM-TI-712, Westinghouse Hanford Company, Richland, Washington.

Wilkins NE, RE Bauer, and DM Ogden. 1996. *Results of Vapor Space Monitoring of Flammable Gas Watch List Tanks.* HNF-SD-WM-TI-797, Westinghouse Hanford Company, Richland, Washington.

Zhang DZ and A Prosperetti. 1993. "Ensemble Averaged Euler Equations and Added Mass for Linearized Flows." *Gas-Liquid Flows 1993.* FED-Vol. 165, American Society of Mechanical Engineers, New York.